



FRIEDRICH-SCHILLER-
UNIVERSITÄT
JENA

ABOVE-THRESHOLD IONIZATION DRIVEN
BY SPATIALLY STRUCTURED LASER FIELDS

DISSERTATION

zur Erlangung des akademischen Grades
doctor rerum naturalium (Dr. rer. nat.)

vorgelegt dem Rat der
PHYSIKALISCH-ASTRONOMISCHEN FAKULTÄT
der
FRIEDRICH-SCHILLER-UNIVERSITÄT JENA

von

M. Sc. Birger Nils Böning
geboren am 17.04.1990 in Bremen

GUTACHTER:

1. Prof. Dr. Stephan Fritzsche (Friedrich-Schiller-Universität Jena)
2. Prof. Dr. Manfred Lein (Leibniz Universität Hannover)
3. Prof. Dr. Stefanie Gräfe (Friedrich-Schiller-Universität Jena)

TAG DER DISPUTATION: 25. Juni 2020

Dedicated to the memory of my father.

ABSTRACT

Strong laser fields are a valuable tool to study the electron dynamics in atoms and molecules. A prominent strong-field process is the above-threshold ionization (ATI), where the momentum distributions of emitted photoelectrons encode not only details about the laser-atom interaction, but also properties of the driving laser field. Recent advances in the generation of intense laser beams at mid-infrared wavelengths enable the investigation of ATI in a new parameter range. Moreover, laser beams with a sophisticated spatial structure as a result of an orbital angular momentum (twisted light) have found applications in the strong-field regime.

In this dissertation, we theoretically investigate ATI driven by mid-infrared and twisted light beams. We show that not only the temporal but also the *spatial* dependence of such beams has a pronounced impact on the ionization dynamics due to *nondipole* interactions. Therefore, we develop a quite general theoretical approach to ATI that incorporates this spatial structure: in order to extend the widely used strong-field approximation (SFA), we construct nondipole Volkov states which describe the photoelectron continuum dressed by the laser field. The resulting *nondipole SFA* allows the treatment of ATI and other strong-field processes driven by spatially structured laser fields and is not restricted to plane-wave beams.

We apply this nondipole SFA to the ATI driven by mid-infrared plane-wave laser beams and show that *peak shifts* in the photoelectron momentum distributions can be computed in good agreement with experiments. As a second application, we consider the ATI driven by standing light waves, known as *high-intensity Kapitza-Dirac effect*. Here, we calculate the momentum transfer to photoelectrons for elliptically polarized standing waves and demonstrate that low- and high-energy photoelectrons exhibit markedly different angular distributions, which were not observed previously.

Finally, we investigate the ATI of localized atomic targets driven by intense *few-cycle Bessel pulses*. Based on a local dipole approximation, we demonstrate that the photoelectrons can also be emitted along the propagation direction of the pulse owing to longitudinal electric field components. Moreover, when measured in propagation direction, the ATI spectra depend on both the opening angle and the orbital angular momentum of the Bessel pulse. To conclude, we also discuss the extension of this work towards long pulses, which can be treated within the above nondipole SFA.

ZUSAMMENFASSUNG

Starke Laserfelder sind ein wertvolles Hilfsmittel zur Untersuchung der Elektronendynamik in Atomen und Molekülen. Ein wichtiger Starkfeldprozess ist die Above-Threshold-Ionisation (ATI), bei der die Impulsverteilungen der emittierten Photoelektronen auf Details der Laser-Atom-Wechselwirkung und auf Eigenschaften des treibenden Laserfeldes schließen lassen. Jüngste Fortschritte in der Erzeugung intensiver Laserstrahlen mit Wellenlängen im mittleren Infrarot erlauben ATI-Experimente in einem neuen Parameterbereich. Zusätzlich haben Laserstrahlen mit einer komplexen räumlichen Struktur als Resultat eines Bahndrehimpulses (getwistetes Licht) Anwendungen im Starkfeldregime gefunden.

In dieser Dissertation wird die ATI mit Laserstrahlen im mittleren Infrarot und mit getwisteten Laserstrahlen theoretisch untersucht. Es wird gezeigt, dass neben der zeitlichen auch die *räumliche* Abhängigkeit der Strahlen einen deutlichen Einfluss auf die Ionisationsdynamik hat, der aus *Nichtdipol-Wechselwirkungen* resultiert. Deshalb wird ein allgemeiner theoretischer Zugang zur ATI entwickelt, der diese räumliche Struktur berücksichtigt: Um die häufig angewandte Starkfeldnäherung (SFA) zu erweitern, werden Nichtdipol-Volkovzustände konstruiert, die das Elektronenkontinuum im Laserfeld beschreiben. Diese *Nichtdipol-SFA* erlaubt die Behandlung der ATI und anderer Starkfeldprozesse getrieben durch räumlich strukturierte Laserfelder. Die Nichtdipol-SFA wird auf die ATI mit ebenen Laserstrahlen im mittleren Infrarot angewandt und es wird gezeigt, dass Verschiebungen der Maxima in den Impulsverteilungen der Photoelektronen in guter Übereinstimmung mit Experimenten berechnet werden können. Als weitere Anwendung wird die ATI mit stehenden Lichtwellen betrachtet, auch bekannt als *Hochintensitäts-Kapitza-Dirac-Effekt*. Dabei wird der Impulstransfer auf die Photoelektronen für elliptisch polarisierte stehende Wellen berechnet und gezeigt, dass nieder- und hochenergetische Photoelektronen unterschiedliche Winkelverteilungen aufweisen, die bisher nicht beobachtet wurden. Schließlich wird die ATI lokalisierter atomarer Targets mit intensiven kurzen Besselpulsen untersucht. Mit einer lokalen Dipolnäherung wird gezeigt, dass die Photoelektronen aufgrund longitudinaler Komponenten des elektrischen Feldes auch in Ausbreitungsrichtung des Pulses emittiert werden. Des Weiteren hängen die entsprechenden ATI-Spektren sowohl vom Öffnungswinkel als auch vom Bahndrehimpuls des Besselpulses ab. Schlussendlich wird die Erweiterung hin zu langen Pulsen diskutiert, die innerhalb der Nichtdipol-SFA behandelt werden kann.

PUBLICATIONS

The material presented in this thesis was contributed to the following publications:

- *Polarization-dependent high-intensity Kapitza-Dirac effect in strong laser fields*
B. Böning, W. Paufler, and S. Fritzsche
PHYSICAL REVIEW A (Rapid Communications)
Accepted for publication (2020)
- *Nondipole strong-field approximation for spatially structured laser fields*
B. Böning, W. Paufler, and S. Fritzsche
PHYSICAL REVIEW A **99**, 053404 (2019)
- *Above-threshold ionization by few-cycle Bessel pulses carrying orbital angular momentum*
B. Böning, W. Paufler, and S. Fritzsche
PHYSICAL REVIEW A **98**, 023407 (2018)

The following publications do not contain thesis work:

- *Strong-Field Ionization with Few-Cycle Bessel Pulses: Interplay Between Orbital Angular Momentum and Carrier Envelope Phase*
W. Paufler, B. Böning, and S. Fritzsche
In: *Quantum Collisions and Confinement of Atomic and Molecular Species, and Photons*
Ed. by P.C. Deshmukh, E.Krishnamurthy, and Sonjoy Majumder (2019). Springer Proceedings in Physics, vol 230. Springer, Singapore
- *Coherence control in high-order harmonic generation with Laguerre-Gaussian beams*
W. Paufler, B. Böning, and S. Fritzsche
PHYSICAL REVIEW A **100**, 013422 (2019)
- *High harmonic generation with Laguerre-Gaussian beams*
W. Paufler, B. Böning, and S. Fritzsche
Journal of Optics **21**(9), 094001 (2019)
- *Dichroism in two-color above-threshold ionization with twisted XUV beams and intense infrared laser fields*
B. Baghdasaryan, B. Böning, W. Paufler, and S. Fritzsche
PHYSICAL REVIEW A **99**, 023403 (2019)

- *Tailored orbital angular momentum in high-order harmonic generation with bicircular Laguerre-Gaussian beams*
W. Paufler, B. Böning, and S. Fritzsche
PHYSICAL REVIEW A **98**, 011401(R) (2018)
- *Strong-field ionization with twisted laser pulses*
W. Paufler, B. Böning, and S. Fritzsche
PHYSICAL REVIEW A **97**, 043418 (2018)
- *Attosecond streaking with twisted X waves and intense infrared pulses*
B. Böning, W. Paufler, and S. Fritzsche
PHYSICAL REVIEW A **96**, 043423 (2017)

ACKNOWLEDGMENTS

This dissertation would not have been possible without the people who have supported me in different ways over the past years and during the time of writing.

First and foremost, I want to thank *Prof. Stephan Fritzsche* for giving me the opportunity to work on this research topic and for our discussions in which he always brought up the right questions. In addition, I am grateful for his understanding and the freedom he gave me during difficult periods.

Likewise, I want to thank all those who have been part of the Atomic Theory Group in Jena during my PhD time. Many helpful discussions and remarks during our seminars and group meetings have advanced my work further than it would have been possible by a single person.

A special thanks goes to *Willi Paufler* for our many trips to conferences and for finding our way into the topic of strong-field atomic physics together.

Last but not least, I thank *Carolin Hundt, Milena Leutnant, Malte Böning* and *Willi Paufler*, who made major contributions to the readability of the dissertation by proofreading large parts of the manuscript.

CONTENTS

1	INTRODUCTION	1
2	DESCRIPTION OF LASER BEAMS AND PULSES	7
2.1	Maxwell's equations	7
2.2	Relevance of the spatial structure	8
2.3	Plane waves	9
2.3.1	Plane-wave beams	9
2.3.2	Plane-wave pulses	12
2.4	Twisted light	12
3	THEORY OF ABOVE-THRESHOLD IONIZATION	17
3.1	Overview of methods	18
3.2	Dipole approximation	20
3.3	Strong-field approximation	22
3.3.1	Volkov states in dipole approximation	27
3.3.2	Choice of gauge	28
3.4	ATI with plane-wave beams and pulses	29
4	NONDIPOLE SFA FOR SPATIALLY STRUCTURED LASER FIELDS	33
4.1	Nondipole SFA theories	33
4.1.1	Formulation of the problem	34
4.1.2	Previous approaches	36
4.2	Nondipole Volkov states for integral superpositions of plane waves	37
4.2.1	Solution of the Schrödinger equation	37
4.2.2	Modified Volkov phase	41
4.2.3	Relation to other nondipole SFA theories	43
5	PEAK SHIFTS IN THE ATI WITH PLANE-WAVE BEAMS	45
5.1	Nondipole effects in plane-wave laser fields	45
5.2	Setup and parameters	48
5.3	Photoionization probability	49
5.3.1	Nondipole Volkov states	49
5.3.2	SFA transition amplitude	52
5.3.3	Computation of ATI spectra and peak shifts	54
5.4	Results	55
5.4.1	Circular polarization	55
5.4.2	Linear polarization	59

5.5	Conclusions	61
6	HIGH-INTENSITY KAPITZA-DIRAC EFFECT	63
6.1	Electron deflection by a standing light wave	63
6.2	Setup and parameters	67
6.3	Photoionization probability	69
6.3.1	Nondipole Volkov states	69
6.3.2	SFA transition amplitude	72
6.3.3	Computation of polar-angle distributions	72
6.3.4	Target position	73
6.4	Results	74
6.5	Conclusions	78
7	ATI WITH FEW-CYCLE BESSEL PULSES	79
7.1	Twisted light in atomic physics	79
7.2	Setup and parameters	80
7.3	Photoionization probability	82
7.3.1	Local dipole approximation	82
7.3.2	SFA transition amplitude	83
7.4	Results	84
7.5	Towards nondipole effects	89
8	CONCLUSIONS AND OUTLOOK	93
A	BESSEL FUNCTIONS OF THE FIRST KIND	99
B	DIPOLE VOLKOV STATES: DERIVATIONS	101
B.1	Plane-wave laser pulse	101
B.2	Bessel pulse	104
C	ZEROth-ORDER APPROXIMATION IN THE NONDIPOLE SFA	107
D	NONDIPOLE VOLKOV STATES: DERIVATIONS	109
D.1	Plane-wave laser beam	109
D.2	Standing light wave	111
	BIBLIOGRAPHY	117
	DECLARATION	127

LIST OF FIGURES

Figure 1.1	Strong-field processes	2
Figure 2.1	Visualization of plane-wave beams	10
Figure 2.2	Visualization of Bessel beams	13
Figure 3.1	Three-step model	19
Figure 3.2	Validity of the dipole approximation	21
Figure 3.3	ATI spectra for plane-wave pulses	32
Figure 5.1	Setup of ATI with plane-wave beams and illustration of peak shifts	48
Figure 5.2	Peak shifts for circular polarization	56
Figure 5.3	Peak shifts for linear polarization	59
Figure 6.1	Overview of the free-electron KDE	64
Figure 6.2	Overview of the high-intensity KDE	66
Figure 6.3	Visualization of standing light waves	68
Figure 6.4	Momentum transfer in the high-intensity KDE for linear polarization	75
Figure 6.5	Momentum transfer in the high-intensity KDE for elliptical polarization	77
Figure 7.1	Setup of ATI with Bessel pulses	81
Figure 7.2	ATI spectra in the plane-wave limit of Bessel pulses	85
Figure 7.3	Dependence of ATI spectra on the polar angle	86
Figure 7.4	Dependence of ATI spectra on the opening angle	87
Figure 7.5	Ponderomotive energy of electrons in Bessel pulses as function of the opening angle	89
Figure 7.6	Modified Volkov phase in a Bessel beam	90

ACRONYMS

ATI	above-threshold ionization
HHG	high-harmonic generation
IR	infrared
KDE	Kapitza-Dirac effect
PAD	polar-angle distribution
PEMD	photoelectron momentum distribution
SFA	strong-field approximation
TAM	total angular momentum

TOOLS AND METHODS

The content presented in this thesis consists to a large part of analytical work. Wherever results are shown for specific physical parameters, computational tools have been employed to evaluate the respective analytical expressions for numerical values. In particular, Wolfram Mathematica v. 11 (Wolfram Research, Inc., 2016) was used for the results shown in Sec. 3.4, in Sec. 5.4 according to the procedure outlined in Sec. 5.3.3, in Sec. 6.4 according to the procedure outlined in Sec. 6.3.3, and in Sec. 7.5. The results presented in Sec. 7.4 were computed using a simple self-written C++ code that evaluates the equations in Sec. 7.3.2 for specific laser parameters. Moreover, all figures shown in this thesis have been created with Wolfram Mathematica v. 11 and Inkscape v. 0.92 (Harrington, 2018).

INTRODUCTION

The interaction of light and matter lies at the heart of our experience and understanding of the world. Everything we see around us is a direct consequence of this interaction. Since ancient times, the nature of light and of the building blocks of matter has therefore captured people's imagination. Starting in the 19th century and continuing to this day, science has unveiled more and more details of this nature.

That light is, in fact, an electromagnetic wave was discovered through the work of Faraday and many others on how electric and magnetic fields influence each other and charges in their vicinity (Whittaker, 1910, chapter 6). These discoveries converged into a theoretical description of the dynamics of these fields and including electromagnetic waves, known as Maxwell's equations (Maxwell, 1865). Supplemented with equations that describe the state of matter, they explain many macroscopic phenomena related to light-matter interactions. Discrepancies prevail, however, on the microscopic scale.

To provide an example, the photoelectric effect, where electrons are emitted when light shines on a metal plate, remained elusive in the wave picture of light. Its successful explanation by Einstein (1905) advanced our understanding of microscopic processes, based on the assumption that light consists of individual particles (photons), which carry well-defined quanta of energy, $E = \hbar\omega$ with the light's frequency ω (Planck, 1901). Beginning with this *quantum theory* of light, new laws were discovered that govern the building blocks of matter. These laws of quantum mechanics, culminating in the equations of Schrödinger (1926) and Dirac (1928), brought a new understanding of electrons, atoms and molecules. Most notably, they predict that within an atom electrons are bound by the electrostatic force of the nucleus and can only exist in quantized energy levels.

What determines the precise structure of these energy levels? And is it possible to influence or even control the electron in the atom? Such questions have excited physicists since the discovery of quantum mechanics. Their answers have become accessible through one of the great inventions of the 20th century: the laser allows the generation of bright, coherent light with a fixed and stable wavelength $\lambda = \omega/2\pi c$ and, therefore, photon energy (Maiman, 1960). This new tool made precise experiments

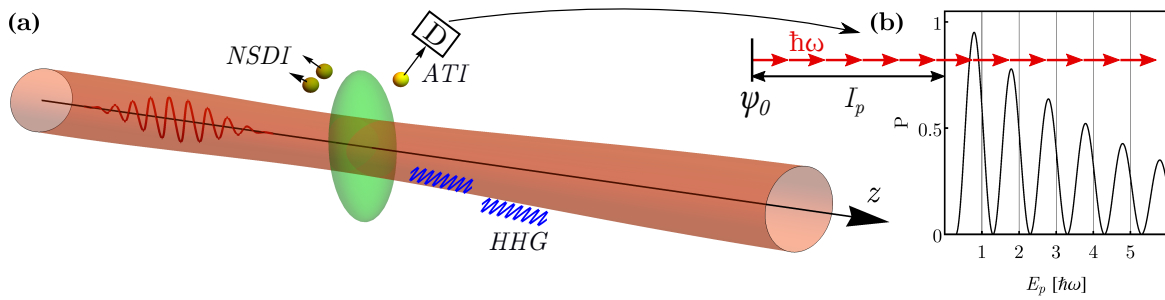


Figure 1.1: Strong-field processes. (a) In a typical strong-field experiment, a gas cloud of atoms (green) is illuminated by a strong laser beam (red with the oscillating electric field shown inside). Upon interaction with the gas atoms, several processes can be observed: high-harmonic generation (HHG), where high-energetic photons (blue) are emitted; above-threshold ionization (ATI), where a single electron is emitted per atom; non-sequential double ionization (NSDI), where two electrons are emitted simultaneously. (b) If a detector (D) measures the energy spectrum $P(E_p)$ of the ATI electrons, several peaks are visible, spaced by the photon energy $\hbar\omega$: the bound electron in the ground state ψ_0 absorbs several photons (red arrows) to overcome the ionization threshold I_p . Subsequently, it may absorb more photons from the laser beam in the continuum before reaching the detector.

possible that can probe the quantized structure of atoms and revealed a variety of processes on the atomic scale.

One particular example is the *photoionization* of atoms, which is closely related to the photoelectric effect: an atom is irradiated by a continuous beam of laser light and absorbs enough energy to raise an electron from a bound state to the continuum, where it can subsequently be detected. If the photon energy is high enough, one photon is already sufficient to release an electron. However, if one increases the wavelength of the laser beam, more and more photons need to be absorbed and the quantum-mechanical *photoionization probability* decreases. One can counteract this decrease, however, by increasing the intensity of the laser beam, i.e. the amplitude of its electric and magnetic fields, which implies a higher density of photons. In this way, one enters the realm of strong-field atomic physics.

If such a *strong* laser beam interacts with a gas cloud of atoms, a variety of strong-field processes can be observed, which are illustrated in Fig. 1.1 (a). First, a single electron may be emitted from an atom, which is called strong-field ionization. Second, two electrons may be emitted simultaneously [*non-sequential double ionization*; Walker et al. (1994)]. Third, photons may be emitted carrying multiples of the incoming photon energy, if the electron released in the first place recombines with its parent ion [*high-harmonic generation (HHG)*; McPherson et al. (1987)]. These strong-field processes have been studied extensively over the past decades and have not only given insight into the underlying mechanisms of laser-atom interactions (Schultze et al., 2010) but have also enabled the advancement of new laser sources and the exploration of

the internal dynamics of atoms and molecules on its natural time scale [attosecond science; Calegari et al. (2016)].

Let us take a closer look at strong-field ionization. As stated above, the electron may absorb several photons to overcome the ionization potential and enter the continuum. However, Agostini et al. (1979) made the surprising discovery that the electron may absorb even more photons than this minimum number necessary to overcome the threshold [see Fig. 1.1 (b)]. Today, this process is known as *above-threshold ionization* (ATI). If the energy spectrum of the emitted photoelectron is measured, several maxima are visible, spaced by the photon energy $\hbar\omega$. Depending on the laser parameters, these so-called *ATI peaks* may extend to quite high photoelectron energies (Schafer et al., 1993; Paulus et al., 1994).

Today, a typical ATI experiment measures either the photoelectron momentum distribution (PEMD), that is, the photoionization probability as a function of the emission angle of the photoelectron, or the energy spectra of photoelectrons emitted in a particular direction. Instead of continuous laser beams, *laser pulses* of a short duration are often used. Nowadays, femtosecond pulses can routinely be generated and their temporal shape can be precisely controlled (Wollenhaupt et al., 2016). From ATI experiments with such laser pulses, one can deduce properties of the atom as well as of the driving laser pulse itself (Becker et al., 2018).

For many years, strong-field experiments have been performed at $\lambda = 800$ nm in the near-infrared (IR) ($\lambda \approx 780 - 3000$ nm), a typical wavelength emitted by the widely used Ti:sapphire-laser (Moulton, 1986). Very recently, however, advances in the generation of laser sources in the mid-IR ($\lambda \approx 3000 - 50000$ nm) have enabled the experimental investigation of both ATI and HHG at longer wavelengths (Colosimo et al., 2008; Popmintchev et al., 2012; Dura et al., 2013). This promises fascinating technical advances for ultrashort laser pulses (Hernández-García et al., 2013). However, the understanding and utilization of strong-field processes driven by long-wavelength laser beams presents significant challenges for both experiment and theory: while in the near-IR, the dynamics of these processes is driven solely by the electric field of the laser beam, for mid-IR beams the magnetic field also has a significant influence on the behavior of the electron. This does not only alter the PEMD measured in ATI experiments (Smeenk et al., 2011) but also suppresses the recombination with the parent ion that is necessary to induce HHG (Pisanty et al., 2018). For these reasons, an improvement of our theoretical description of strong-field processes in the mid-IR in general and ATI in particular is required.

The theoretical understanding of strong-field processes is based on the Schrödinger equation, which describes the non-relativistic dynamics of the electron under the influence of the laser beam or pulse and the field of the atomic nucleus. That is, it

encodes all details of the transition of the electron from a bound state in the atom to a continuum state. Today, several methods exist to calculate the PEMD in ATI for given atomic and laser pulse parameters, which we will describe in more detail in Sec. 3.1. In this dissertation, we will make use of and extend the so-called *strong-field approximation (SFA)*, which allows an analytical solution of the Schrödinger equation as opposed to a purely numerical treatment (Keldysh, 1964; Faisal, 1973; Reiss, 1980). Within the SFA, one assumes that the continuum states accessible to the electron do not see the presence of the electrostatic potential of the remaining ionic core. Instead, they are described by so-called *Volkov states*, which take only the influence of the laser field into account (Volkov, 1935). In this sense, the SFA assumes a *strong* laser field compared to the binding potential. Together with a few other assumptions (cf. Sec. 3.3), the SFA then allows the treatment of many strong-field processes, including ATI, and has been very successful in this regard (Amini et al., 2019).

Nevertheless, most of the theoretical methods developed to describe strong-field processes in the near-IR make explicit use of the assumption that the dynamics is driven by a purely time-dependent electric field of the laser beam (*dipole approximation*). As already mentioned above, this approximation is not appropriate when one deals with mid-IR driving laser fields. At present, extensions exist of numerical (Brennecke and Lein, 2018), semi-classical (Willenberg et al., 2019) as well as SFA-based methods (Titi and Drake, 2012) towards the *nondipole* regime, i.e. beyond the dipole approximation. Within these nondipole methods, many features of ATI driven by mid-IR *plane-wave* laser beams can be explained.

We will explain in Sec. 2.2 that the neglect of the magnetic field of the driving laser beam is equivalent to stating either that the photon's *momentum* is zero or that the laser beam has no *spatial structure*, i.e. is spatially homogeneous. While the mid-IR *plane-wave* laser fields mentioned above are an important case where the magnetic field plays a role in ATI, other laser fields exist that exhibit a more complicated spatial structure and cannot be described as plane waves (Kotlyar and Kovalev, 2008; Andrews and Babiker, 2013; Ornigotti et al., 2016). Among them are so-called *twisted* laser beams, which carry an orbital angular momentum with respect to their beam axis (Allen et al., 1992). This property makes them a versatile tool in laser-atom interactions since it gives access to atomic excitation and ionization pathways that are not accessible with plane-wave laser beams due to angular momentum conservation (Scholz-Marggraf et al., 2014; Schmiegelow et al., 2016). Nowadays, twisted laser beams can routinely be generated using, for example, spiral phase plates (Andrews and Babiker, 2013, chapter 1). Very recently, twisted laser beams have found their way into strong-field physics, especially HHG (Garipey et al., 2014; Dorney et al., 2018; Paufler et al., 2018b), and it has been observed that orbital angular momentum is

transferred from the laser beam to the target. In order to properly describe strong-field processes driven by twisted laser beams, including their angular momentum properties, it is essential to account for the beam's spatial structure in the electron dynamics. Until now, however, no formulations of a nondipole SFA or other theoretical methods exist that achieve this goal.

In this dissertation, we will therefore extend the SFA to laser beams that have a (quite general) spatial structure. With this theoretical approach to *ATI driven by spatially structured laser fields*, we will analyze particular experimental scenarios that involve either (mid-IR) plane-wave beams, superpositions of them, or twisted beams.

The dissertation is structured as follows. In Chap. 2, we will review the theoretical description of light. We start with Maxwell's equations and the electromagnetic potentials in Sec. 2.1, before we discuss the relevance of the spatial structure of laser beams in Sec. 2.2. Finally, we introduce plane-wave laser beams and pulses in Sec. 2.3 and twisted light beams in Sec. 2.4.

In Chap. 3, we will then examine the theory of ATI in the dipole approximation. After giving an overview of the different methods presently in use in Sec. 3.1 and a discussion of the dipole approximation in Sec. 3.2, we go through the derivation of the SFA transition amplitude and the (dipole) Volkov states in Sec. 3.3. We then apply the dipole SFA to ATI and show that it allows the calculation of ATI spectra for near-IR driving laser pulses in Sec. 3.4.

In Chap. 4, we turn to the extension of the SFA towards laser fields of a general spatial structure. We begin with an overview of nondipole SFA theories in Sec. 4.1 and a review of specific work done by other authors in Sec. 4.1.2. In Sec. 4.2, we then show how *nondipole* Volkov states can be derived, which describe the electron continuum dressed by the spatially-dependent laser field. We conclude the chapter with a discussion of the relation of our work to other nondipole SFA theories.

As a first application, we will demonstrate in Chap. 5 that this nondipole SFA can be applied to the ATI driven by mid-IR plane-wave laser beams and yields theoretical results in good agreement with experiments. In particular, we will analyze *peak shifts* of the PEMD along the laser propagation direction. We describe the experimental setup in Sec. 5.2 and derive the nondipole Volkov states and the SFA transition amplitude in Sec. 5.3, before we present our results in Sec. 5.4.

In Chap. 6, we will turn to a second application: the so-called high-intensity Kapitza-Dirac effect (KDE), where an atomic target is ionized in the field of a strong *standing light wave*, which gives rise to a large transfer of longitudinal momentum to the photoelectron. We introduce the KDE in Sec. 6.1 and discuss the specific setup in Sec. 6.2. Subsequently, we show in Sec. 6.3 how the high-intensity KDE can be described within our nondipole SFA. Specific results are discussed in Sec. 6.4 with an

emphasis on the angular distributions of low- and high-energy photoelectrons and how the momentum transfer depends on the ellipticity of the standing light wave.

Chapter 7 deals with ATI of a localized atomic target driven by twisted Bessel pulses. Here, we will argue that for few-cycle Bessel pulses, nondipole effects due to the spatial structure can be neglected and the photoionization probability can be calculated within a *local dipole approximation* (Sec. 7.3). We discuss the ATI spectra computed within this approximation in Sec. 7.4 and show that they differ significantly from those found with plane-wave laser beams due to an additional longitudinal component of the electric field. Eventually, in Sec. 7.5, we discuss the extension towards nondipole effects that become important for longer pulse durations.

Finally, we give our conclusions and an outlook to future work in Chap. 8.

Atomic units are used throughout the dissertation unless stated otherwise:

$$m_e = e = \hbar = 4\pi\epsilon_0 = 1$$

DESCRIPTION OF LASER BEAMS AND PULSES

2.1 MAXWELL'S EQUATIONS

In order to theoretically model laser-atom interactions, a mathematical description is needed of light propagating in vacuum. As an electromagnetic wave, it is described by electric and magnetic fields $\mathbf{E}(\mathbf{r}, t)$ and $\mathbf{B}(\mathbf{r}, t)$ that are solutions to Maxwell's equations in the absence of charges and currents (Jackson, 1999, introduction),

$$\nabla \cdot \mathbf{E}(\mathbf{r}, t) = 0, \quad \nabla \times \mathbf{E}(\mathbf{r}, t) = -\frac{\partial \mathbf{B}(\mathbf{r}, t)}{\partial t}, \quad (2.1a)$$

$$\nabla \cdot \mathbf{B}(\mathbf{r}, t) = 0, \quad \nabla \times \mathbf{B}(\mathbf{r}, t) = \frac{1}{c^2} \frac{\partial \mathbf{E}(\mathbf{r}, t)}{\partial t}, \quad (2.1b)$$

with the speed of light c . The solution of Maxwell's equations is simplified upon the introduction of a scalar potential $\phi(\mathbf{r}, t)$ and a vector potential $\mathbf{A}(\mathbf{r}, t)$ which are related to the fields via

$$\mathbf{E}(\mathbf{r}, t) = -\nabla\phi(\mathbf{r}, t) - \frac{\partial \mathbf{A}(\mathbf{r}, t)}{\partial t}, \quad (2.2a)$$

$$\mathbf{B}(\mathbf{r}, t) = \nabla \times \mathbf{A}(\mathbf{r}, t). \quad (2.2b)$$

For given physical fields $\mathbf{E}(\mathbf{r}, t)$ and $\mathbf{B}(\mathbf{r}, t)$, the potentials are not unambiguously defined through these equations: any *gauge transformation* of the form

$$\phi'(\mathbf{r}, t) = \phi(\mathbf{r}, t) - \frac{\partial f(\mathbf{r}, t)}{\partial t}, \quad (2.3a)$$

$$\mathbf{A}'(\mathbf{r}, t) = \mathbf{A}(\mathbf{r}, t) + \nabla f(\mathbf{r}, t), \quad (2.3b)$$

with an arbitrary (smooth) scalar function $f(\mathbf{r}, t)$ leaves the fields invariant. In order to determine the potentials from Maxwell's equations, it is therefore necessary to fix the gauge by imposing conditions on $\phi(\mathbf{r}, t)$ and $\mathbf{A}(\mathbf{r}, t)$. In this chapter, the Coulomb gauge will be used, which is defined by (Jackson, 1999, chapter 6)

$$\phi(\mathbf{r}, t) = 0, \quad \nabla \cdot \mathbf{A}(\mathbf{r}, t) = 0. \quad (2.4)$$

Upon insertion of the relations (2.2) and using the Coulomb gauge condition (2.4), Maxwell's equations (2.1) reduce to a single wave equation for the vector potential,

$$\nabla^2 \mathbf{A}(\mathbf{r}, t) - \frac{1}{c^2} \frac{\partial^2 \mathbf{A}(\mathbf{r}, t)}{\partial t^2} = 0. \quad (2.5)$$

This system of wave equation (2.5) and Coulomb gauge condition (2.4) is then equivalent to Maxwell's equations.

Since the wave equation (2.5) is linear in $\mathbf{A}(\mathbf{r}, t)$, any solution may be written as a superposition of monochromatic electromagnetic waves of the form

$$\mathbf{A}(\mathbf{r}, t) = \text{Re} \left\{ \mathbf{A}(\mathbf{r}) e^{-i\omega t} \right\}, \quad (2.6)$$

with the frequency $\omega = 2\pi c/\lambda$ and the wavelength λ . The wave equation (2.5) then reduces to the Helmholtz equation,

$$(\nabla^2 + k^2) \mathbf{A}(\mathbf{r}) = 0, \quad (2.7)$$

where $k = \omega/c$ is the wave number. It is instructive to write this equation in terms of the linear momentum operator $\hat{\mathbf{p}} = -i\nabla$,

$$\hat{\mathbf{p}}^2 \mathbf{A}(\mathbf{r}) = k^2 \mathbf{A}(\mathbf{r}). \quad (2.8)$$

Thus, a monochromatic solution to the wave equation is an eigenfunction of the squared linear momentum operator. The corresponding eigenvalue $k = \omega/c$ is interpreted as the photon momentum.

An important property for strong-field laser-atom interactions is the laser beam's *intensity*, defined as the absolute value of the cycle-averaged Poynting vector $\mathbf{S}(\mathbf{r}, t) = \frac{1}{\mu_0} \mathbf{E}(\mathbf{r}, t) \times \mathbf{B}(\mathbf{r}, t)$ (Saleh and Teich, 1991, chapter 2),

$$I(\mathbf{r}, t) = \frac{1}{T} \left| \int_t^{t+T} d\tau \mathbf{S}(\mathbf{r}, \tau) \right|, \quad (2.9)$$

with the cycle length $T = 2\pi/\omega$. It is important to note that, in general, the intensity depends on both time t and space \mathbf{r} .

2.2 RELEVANCE OF THE SPATIAL STRUCTURE

The dependence of the vector potential on the spatial coordinates, $\mathbf{A}(\mathbf{r})$, defines the *spatial structure* of the laser beam. An important conclusion can be drawn from the linear momentum eigenvalue equation (2.8): suppose that the vector potential has

no spatial structure, i.e. $\mathbf{A}(\mathbf{r}) = \text{const.}$ Then it follows from Eq. (2.8) that its linear momentum eigenvalue is zero, $k = 0$. In addition, Eq. (2.2b) implies that the magnetic field vanishes. Hence, the following three statements are equivalent:

- The laser beam has a spatial structure, $\mathbf{A}(\mathbf{r}) \neq \text{const.}$
- The magnetic field of the laser beam is nonzero, $\mathbf{B}(\mathbf{r}, t) \neq 0$.
- The photon's linear momentum is nonzero, $k \neq 0$.

In general, the dispersion relation $k = \omega/c$ forbids the existence of oscillating fields ($\omega \neq 0$) without spatial structure ($k = 0$). Often, however, this spatial structure is neglected in the description of laser-atom interactions. This so-called dipole approximation is discussed in more detail in Sec. 3.2. Under certain conditions, the non-vanishing photon momentum becomes visible in the spectra of photoelectrons in strong-field ionization experiments. Then, a theoretical description of these experiments needs to account for the spatial structure, or, equivalently, the magnetic field of the laser beam. How this can be accomplished will be the focus of Chap. 4.

2.3 PLANE WAVES

2.3.1 Plane-wave beams

A simple set of solutions to the Helmholtz equation (2.7) is given by monochromatic plane-wave light beams of the form

$$\mathbf{A}(\mathbf{r}) = A_0 e^{i\mathbf{k}\cdot\mathbf{r}} \boldsymbol{\varepsilon}, \quad (2.10)$$

with the amplitude A_0 , the wave vector $\mathbf{k} = k\mathbf{e}_k$ with a unit vector \mathbf{e}_k , and the polarization unit vector $\boldsymbol{\varepsilon}$. For elliptically polarized beams propagating in z -direction, $\mathbf{k} = k\mathbf{e}_z$ and the polarization unit vector is

$$\boldsymbol{\varepsilon} = \frac{1}{\sqrt{1 + \varepsilon^2}} (\mathbf{e}_x + i\varepsilon\Lambda\mathbf{e}_y), \quad (2.11)$$

with the ellipticity $0 \leq \varepsilon \leq 1$ and the helicity $\Lambda = \pm 1$. In particular, beams with $\varepsilon = 0$ and $\varepsilon = 1$ are called linearly and circularly polarized, respectively. The full vector potential (2.6) of the plane-wave beam is given by

$$\mathbf{A}(z, t) = \frac{A_0}{\sqrt{1 + \varepsilon^2}} (\cos(kz - \omega t) \mathbf{e}_x - \varepsilon\Lambda \sin(kz - \omega t) \mathbf{e}_y). \quad (2.12)$$

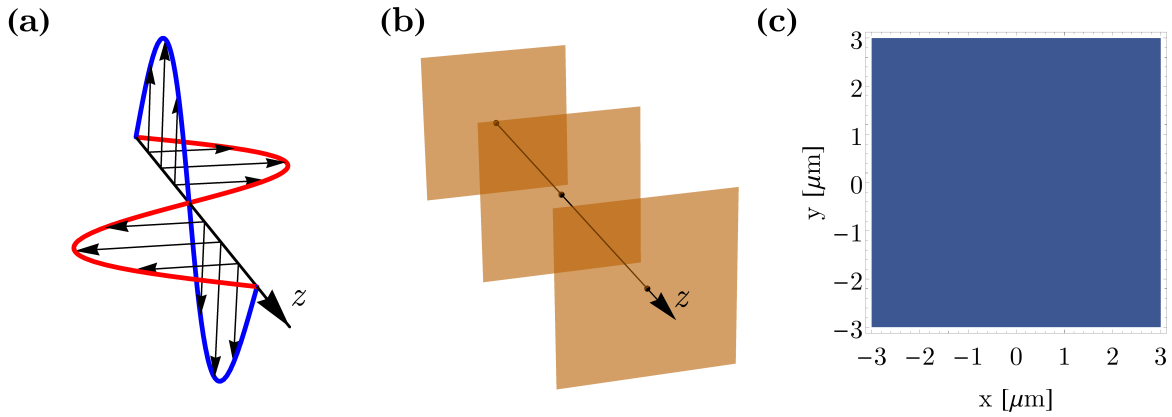


Figure 2.1: Visualization of plane-wave beams. (a) Electric (red) and magnetic (blue) fields of a linearly polarized plane-wave beam as a function of z and for a fixed time $t = t_0$. The amplitude of the magnetic field is exaggerated by a factor c . (b) The phase fronts of the beam are planes perpendicular to the propagation direction. (c) The intensity of a plane wave beam is constant in the plane transverse to the propagation direction, and independent of the ellipticity ε .

These elliptically polarized plane waves are characterized by their wavelength λ , ellipticity ε , helicity Λ as well as their amplitude A_0 . For linear polarization ($\varepsilon = 0$), the electric and magnetic fields corresponding to the vector potential (2.12) are visualized in 2.1 (a). The name *plane wave* stems from the fact that their wave fronts, i.e. the surfaces of constant phase, are planes defined by $kz = \text{const.}$, as shown in Fig. 2.1 (b). Another characteristic property of plane waves is their intensity profile that is given, following Eq. (2.9), by

$$I(\mathbf{r}, t) = \frac{A_0^2 \omega^3 c}{8\pi^2 (1 + \varepsilon^2)} \int_t^{t+\Gamma} d\tau (\sin^2(kz - \omega t) + \varepsilon^2 \cos^2(kz - \omega t)) = \frac{A_0^2 \omega^2 c}{8\pi}. \quad (2.13)$$

Thus, the intensity is uniform in both space and time, and does not depend on the ellipticity of the beam [cf. Fig. 2.1 (c)].

In certain physical scenarios where two or more plane-wave modes are superposed, it is necessary to generalize the vector potential (2.12) for the special case of propagation along the z -axis to arbitrary propagation directions \mathbf{e}_k . If the plane perpendicular to \mathbf{e}_k is spanned by the unit vectors \mathbf{e}_1 and \mathbf{e}_2 such that $\{\mathbf{e}_1, \mathbf{e}_2, \mathbf{e}_k\}$ form a right-handed basis, the polarization unit vector is

$$\boldsymbol{\varepsilon} = \frac{1}{\sqrt{1 + \varepsilon^2}} (\mathbf{e}_1 + i\varepsilon\Lambda\mathbf{e}_2), \quad (2.14)$$

and the vector potential for an elliptically polarized plane wave beam propagating along the \mathbf{e}_k -direction has a form very similar to the above,

$$\mathbf{A}(\mathbf{r}, t) = \frac{A_0}{\sqrt{1 + \varepsilon^2}} (\cos(\mathbf{k} \cdot \mathbf{r} - \omega t) \mathbf{e}_1 - \varepsilon \sin(\mathbf{k} \cdot \mathbf{r} - \omega t) \mathbf{e}_2). \quad (2.15)$$

An important special case is a circularly polarized plane wave beam ($\varepsilon = 1$) that propagates in the direction

$$\mathbf{e}_k = \begin{pmatrix} \cos \vartheta_k \cos \varphi_k \\ \cos \vartheta_k \sin \varphi_k \\ \sin \vartheta_k \end{pmatrix}, \quad (2.16)$$

defined by the polar and azimuthal angles ϑ_k and φ_k of the wave vector, respectively. The polarization unit vector $\boldsymbol{\varepsilon} = \boldsymbol{\varepsilon}_{\mathbf{k}\Lambda}$ then takes the form (Matula et al., 2013)

$$\boldsymbol{\varepsilon}_{\mathbf{k}\Lambda} = -\frac{\Lambda}{\sqrt{2}} \begin{pmatrix} \cos \vartheta_k \cos \varphi_k - i\Lambda \sin \varphi_k \\ \cos \vartheta_k \sin \varphi_k + i\Lambda \cos \varphi_k \\ -\sin \vartheta_k \end{pmatrix}. \quad (2.17)$$

Since, in the interaction with atoms, the z -axis often plays the role of the quantization axis, it is convenient to represent this vector in the (orthonormal) basis of eigenvectors $\boldsymbol{\eta}_{m_s}$ ($m_s = 0, \pm 1$) of the spin projection operator \hat{S}_z with respect to this axis,

$$\hat{S}_z \boldsymbol{\eta}_{m_s} = m_s \boldsymbol{\eta}_{m_s}, \quad \hat{S}_z = -i \begin{pmatrix} 0 & 1 & 0 \\ -1 & 0 & 0 \\ 0 & 0 & 0 \end{pmatrix}. \quad (2.18)$$

The eigenvectors are explicitly given by

$$\boldsymbol{\eta}_0 = \begin{pmatrix} 0 \\ 0 \\ 1 \end{pmatrix}, \quad \boldsymbol{\eta}_{\pm 1} = \frac{\mp 1}{\sqrt{2}} \begin{pmatrix} 1 \\ \pm i \\ 0 \end{pmatrix}, \quad (2.19)$$

and, accordingly, Eq. (2.17) can be written as

$$\boldsymbol{\varepsilon}_{\mathbf{k}\Lambda} = \sum_{m_s=0,\pm 1} c_{m_s} e^{-im_s \varphi_k} \boldsymbol{\eta}_{m_s}, \quad (2.20)$$

with the expansion coefficients $c_0 = \frac{\Lambda}{\sqrt{2}} \sin \vartheta_k$ and $c_{\pm 1} = \frac{1}{2}(1 \pm \Lambda \cos \vartheta_k)$. If we return to a beam propagating along the z -axis, i.e. $\varphi_k = \vartheta_k = 0$ in the above equations, we see that we may interpret the helicity Λ as the projection of the photon's spin onto the beam axis \mathbf{e}_k (Matula et al., 2013).

Finally, let us note that a monochromatic plane-wave laser beam is characterized by its wavelength $\lambda = 2\pi c/\omega$, ellipticity $0 \leq \varepsilon \leq 1$, helicity $\Lambda = \pm 1$ and intensity I .

2.3.2 Plane-wave pulses

In experiments on the interaction of laser light with matter, laser pulses of a finite pulse duration T_p are often employed instead of the continuous beams described by Eq. (2.12). The intensity (2.9) then becomes time-dependent and, therefore, a finite pulse duration may have a profound influence on processes sensitive to the laser intensity. The vector potential $\mathbf{A}^{(P)}(\mathbf{r}, t)$ of a plane-wave laser pulse is modelled by multiplying Eq. (2.12) with an envelope function $f(t)$ (Milošević et al., 2006),

$$\mathbf{A}^{(P)}(z, t) = \frac{A_0}{\sqrt{1 + \varepsilon^2}} f(t) \left(\cos(kz - \omega t + \phi_{\text{CEP}}) \mathbf{e}_x - \varepsilon \Lambda \sin(kz - \omega t + \phi_{\text{CEP}}) \mathbf{e}_y \right), \quad (2.21)$$

where we also added a constant carrier-envelope phase ϕ_{CEP} that determines how the field oscillates relative to the envelope. Whenever we describe finite pulses in this dissertation, we will use a sine-squared-envelope of the form

$$f(t) = \begin{cases} \sin^2\left(\frac{\omega t}{2n_p}\right) & 0 \leq t \leq T_p \\ 0 & \text{otherwise} \end{cases}, \quad (2.22)$$

where the pulse duration $T_p = n_p T$ with the number of optical cycles n_p comprising the pulse. If the laser pulse is sufficiently long ($n_p \rightarrow \infty$), $f(t) \rightarrow 1$ and one may approximate Eq. (2.21) by the vector potential (2.12) of the plane-wave beam.

2.4 TWISTED LIGHT

The plane waves introduced in the previous section represent the simplest forms of electromagnetic waves. We now introduce light beams that carry not only spin but also orbital angular momentum with respect to their beam axis and, as a result, have a more complex spatial structure. Such beams possess helical phase fronts that twist around the propagation axis and are therefore called twisted light beams.

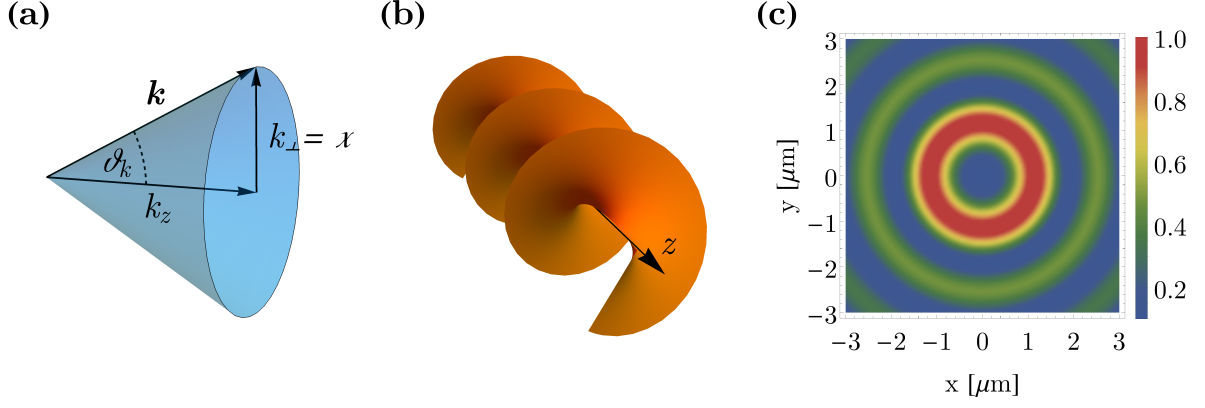


Figure 2.2: Visualization of Bessel beams. (a) A Bessel beam is formed by a superposition of (circularly polarized) plane waves with wave vectors \mathbf{k} lying on a cone with opening angle $\vartheta_k = \arctan(\varkappa/k_z)$. (b) The resulting phase fronts are helices that wind around the beam axis. (c) The transverse intensity profile of a Bessel beam is characterized by a vanishing intensity on the beam axis ($x = y = 0$) and an infinite number of concentric rings. It is shown in units of the maximum intensity for a beam with $\lambda = 800$ nm, $\vartheta_k = 20$ deg., $\Lambda = +1$ and $m_\gamma = 3$.

Our focus here is on Bessel beams, whose vector potential $\mathbf{A}(\mathbf{r}, t)$ is a monochromatic solution (2.6) of the wave equation (2.5) with the additional requirement that it is an eigenstate of the operator of total angular momentum (TAM) projection $\hat{J}_z = \hat{S}_z + \hat{L}_z$ with the orbital angular momentum projection $\hat{L}_z = -i\frac{\partial}{\partial\varphi}$,

$$\hat{J}_z \mathbf{A}(\mathbf{r}) = m_\gamma \mathbf{A}(\mathbf{r}). \quad (2.23)$$

The eigenvalue m_γ is often simply called the TAM of the Bessel beam. Furthermore, we assume that the beam possesses a well-defined longitudinal momentum k_z ,

$$\hat{p}_z^2 \mathbf{A}(\mathbf{r}) = k_z^2 \mathbf{A}(\mathbf{r}). \quad (2.24)$$

Together with the Helmholtz equation (2.7), this implies that a Bessel beam also has a definite modulus of the transverse linear momentum $k_\perp = |\mathbf{k}_\perp| = \varkappa = \sqrt{k^2 - k_z^2}$, where $k = \omega/c$.

In order to find an explicit expression for the Bessel vector potential $\mathbf{A}(\mathbf{r})$, common solutions to the Helmholtz equation (2.7) and the eigenequations (2.23) and (2.24) have to be constructed, which also satisfy the Coulomb gauge condition (2.4). These solutions can be expressed as superpositions of circularly polarized plane waves in the form (Matula et al., 2013)

$$\mathbf{A}(\mathbf{r}) = \frac{A_0}{(2\pi)^2} \int d^2\mathbf{k}_\perp a_{\varkappa m_\gamma}(\mathbf{k}_\perp) \boldsymbol{\varepsilon}_{\mathbf{k}\Lambda} e^{i\mathbf{k}\mathbf{r}}, \quad (2.25)$$

with the helicity $\Lambda = \pm 1$ and the polarization vectors $\boldsymbol{\varepsilon}_{\mathbf{k}\Lambda}$ given by Eq. (2.17). Each plane-wave component in (2.25) is weighted with the amplitude

$$a_{\varkappa m_\gamma}(\mathbf{k}_\perp) = \sqrt{\frac{2\pi}{\varkappa}} (-i)^{m_\gamma} e^{im_\gamma \varphi_k} \delta(\mathbf{k}_\perp - \varkappa). \quad (2.26)$$

Due to the Dirac delta function $\delta(\mathbf{k}_\perp - \varkappa)$, all wave vectors \mathbf{k} of the plane-wave components contributing to the Bessel vector potential lie on a cone with opening angle $\vartheta_k = \arctan(\varkappa/k_z)$ in momentum space, as illustrated in Fig. 2.2 (a).

It is instructive to write down the vector potential (2.25) in position space by performing the integrations over \mathbf{k}_\perp and φ_k using the delta function and the identity

$$\frac{1}{2\pi} \int_0^{2\pi} d\varphi_k e^{i(n\varphi_k \pm k_\perp r \cos(\varphi_k - \varphi_r))} = (\pm i)^n e^{in\varphi_r} J_n(k_\perp r), \quad (2.27)$$

where $J_n(x)$ are the Bessel functions of the first kind (see App. A) and where we use cylindrical coordinates (r, φ_r, z) . Making use of the expansion (2.20) of the polarization unit vector into eigenfunctions (2.19) of \hat{S}_z , the vector potential in position space has the form

$$\mathbf{A}(\mathbf{r}) = \sum_{m_s=0,\pm 1} A_{m_s}(\mathbf{r}) \boldsymbol{\eta}_{m_s}, \quad (2.28a)$$

$$A_{m_s}(\mathbf{r}) = \sqrt{\frac{\varkappa}{2\pi}} (-i)^{m_s} c_{m_s} J_{m_\gamma - m_s}(\varkappa r) e^{i(m_\gamma - m_s)\varphi_r} e^{ik_z z}. \quad (2.28b)$$

In Chap. 7, we will analyze the ATI driven by Bessel beams, where the intensity profile of the Bessel beam plays an important role. The Poynting vector $\mathbf{S}(\mathbf{r}, t)$ corresponding to the fields generated by the vector potential (2.25) has a more intricate form than for a plane-wave beam (Surzhykov et al., 2016). Besides its longitudinal component S_z , it possesses an azimuthal component S_φ and depends, in addition, on the radial coordinate r . However, its radial component S_r vanishes and, thus, no energy flow occurs transverse to the propagation axis. The intensity profile I_\perp of a Bessel beam is defined analogous to (2.9), however, only via the longitudinal component S_z of the Poynting vector (Surzhykov et al., 2016). It is explicitly given by

$$I_\perp(r) = \frac{\omega^2 \varkappa}{4\pi} \left| c_{+1}^2 J_{m_\gamma - 1}^2(\varkappa r) - c_{-1}^2 J_{m_\gamma + 1}^2(\varkappa r) \right|. \quad (2.29)$$

From this equation, we can see that Bessel beams are non-diffractive: their intensity profile does not change along the propagation direction. Figure 2.2 (c) displays a characteristic intensity profile that has a ring-like structure due to the Bessel functions in Eq. (2.29).

Based on the representation (2.28) of the vector potential, one may consider the Bessel beam in the paraxial approximation, in which the transverse momentum is much smaller than the longitudinal momentum, $\varkappa \ll k_z$, or, equivalently, $\vartheta_k \ll 1$. The summation in Eq. (2.28) then reduces to the single term $m_s = \Lambda$,

$$\mathbf{A}(\mathbf{r}) \approx \sqrt{\frac{\varkappa}{2\pi}} (-i)^\Lambda c_\Lambda J_{m_\gamma - \Lambda}(\varkappa r) e^{i(m_\gamma - \Lambda)\varphi_r} e^{ik_z z} \boldsymbol{\eta}_\Lambda, \quad (2.30)$$

and this paraxial Bessel vector potential is a simultaneous eigenfunction of both the spin and orbital angular momentum operators,

$$\hat{S}_z \mathbf{A}(\mathbf{r}) = \Lambda \mathbf{A}(\mathbf{r}), \quad \hat{L}_z \mathbf{A}(\mathbf{r}) = (m_\gamma - \Lambda) \mathbf{A}(\mathbf{r}). \quad (2.31)$$

Therefore, for small opening angle ϑ_k , one may refer to the *orbital* angular momentum $m_l = m_\gamma - \Lambda$ of the Bessel beam. According to Eq. (2.30), the phase fronts of the beam are defined by the equation $(m_\gamma - \Lambda)\varphi_k + k_z z = \text{const.}$, yielding the helical structure shown in Fig. 2.2 (b). Moreover, for $\varkappa \rightarrow 0$ ($J_{m_\gamma - \Lambda}(\varkappa r) \rightarrow \delta_{m_\gamma \Lambda}$) the Bessel vector potential (2.30) reduces to the plane-wave vector potential (2.10) with $\varepsilon = 1$.

In our analysis of the *nonlinear* ATI process driven by Bessel pulses in Chap. 7, we will need a real-valued expression of the form (2.6) for the vector potential (2.28). In the literature, the notion has been adopted to take the imaginary instead of the real part of the vector potential for twisted light beams (Quinteiro et al., 2017a; Paufler et al., 2018a). We will conform to this notion here, since it does not alter the physical results. We then obtain the explicit expressions

$$\begin{aligned} A_x(\mathbf{r}, t) = \sqrt{\frac{\varkappa}{4\pi}} & \left[c_{-1} J_{m_\gamma + 1}(\varkappa r) \cos((m_\gamma + 1)\varphi_r + k_z z - \omega t) \right. \\ & \left. + c_{+1} J_{m_\gamma - 1}(\varkappa r) \cos((m_\gamma - 1)\varphi_r + k_z z - \omega t) \right], \end{aligned} \quad (2.32a)$$

$$\begin{aligned} A_y(\mathbf{r}, t) = \sqrt{\frac{\varkappa}{4\pi}} & \left[c_{-1} J_{m_\gamma + 1}(\varkappa r) \sin((m_\gamma + 1)\varphi_r + k_z z - \omega t) \right. \\ & \left. - c_{+1} J_{m_\gamma - 1}(\varkappa r) \sin((m_\gamma - 1)\varphi_r + k_z z - \omega t) \right], \end{aligned} \quad (2.32b)$$

$$A_z(\mathbf{r}, t) = \sqrt{\frac{\varkappa}{2\pi}} c_0 J_{m_\gamma}(\varkappa r) \sin(m_\gamma \varphi_r + k_z z - \omega t), \quad (2.32c)$$

for the Cartesian components of the real-valued vector potential.

To conclude this section, we note that a Bessel beam is characterized by its wavelength λ , opening angle ϑ_k , helicity $\Lambda = \pm 1$, TAM projection m_γ and the amplitude A_0 . The amplitude A_0 defines the maximum intensity of the Bessel beam, while the position of this intensity maximum in the transverse plane also depends on the other four parameters [cf. Eq. (2.29)].

 THEORY OF ABOVE-THRESHOLD IONIZATION

In this chapter, we will introduce the theoretical approach on which the work of subsequent chapters is founded. As explained in the introduction, we consider the strong-field ionization of atomic targets. In particular, we examine ATI processes, where a single electron is emitted from an atom under the influence of a strong laser field and may absorb more photons than needed to overcome the ionization threshold before it is measured at a detector.

The dynamics of strong-field ionization depends on the physical parameters describing the laser field and the atomic target. Their respective roles in the ionization process is best discussed in the picture of the electron tunneling through the barrier formed by the atomic binding potential that is suppressed by the laser (electric) field [see also Fig. 3.1 (a)]. In this static picture, the atom may undergo either *tunnel* or *over-the-barrier* ionization, depending on the degree of suppression. However, the laser field oscillates in time and, therefore, the potential barrier is suppressed only on the time scale of the laser cycle duration. If this time scale is too short compared to the time scale of the induced electron dynamics, the tunneling process does not take place. Then, the atom may undergo *multiphoton* ionization or, for low intensity and high frequency (photon energy), single-photon ionization. These different regimes can be distinguished using the so-called Keldysh parameter (Keldysh, 1964),

$$\gamma = \sqrt{\frac{I_p}{2U_p}} = \omega \frac{\sqrt{2I_p}}{E_0}, \quad (3.1)$$

where I_p is the ionization potential of the atom and ω and $E_0 = A_0\omega$ are the laser frequency and the amplitude of its electric field, respectively. Furthermore, we introduced the ponderomotive energy

$$U_p = \frac{E_0^2}{4\omega^2}, \quad (3.2)$$

which is the cycle-averaged kinetic energy of a free electron in a plane-wave laser field¹. We can use the Keldysh parameter (3.1) to make the characterization of the ionization mechanism more precise (Amini et al., 2019): multiphoton ionization for $\gamma \gg 1$, tunnel ionization for $\gamma < 1$ and over-the-barrier ionization for $\gamma \ll 1$. The ATI process that we consider in the following is usually understood as a multiphoton ionization process, in which the electron absorbs more photons than needed to overcome the threshold. It can, however, also be described within the tunneling picture and it is often useful to resort to this intuitive picture (Amini et al., 2019).

3.1 OVERVIEW OF METHODS

In a typical ATI experiment, a gas of atoms is irradiated by a strong laser field and the angle-resolved PEMD is measured, which is mathematically given by the energy- and angle-differential photoionization probability $\mathbb{P}(\mathbf{p})$ with the momentum \mathbf{p} of the photoelectron at the detector. The goal of a theoretical description of an ATI process is, then, to compute $\mathbb{P}(\mathbf{p})$ for a given target atom and laser field. The starting point is the Schrödinger equation that describes the dynamics of the electron in terms of its wave function $|\Psi(t)\rangle$ and the Hamiltonian \hat{H} ,

$$i \frac{d}{dt} |\Psi(t)\rangle = \hat{H} |\Psi(t)\rangle, \quad \hat{H} = \frac{1}{2} (\hat{\mathbf{p}} - q\mathbf{A}(\mathbf{r}, t))^2 + q\phi(\mathbf{r}, t) + V(\mathbf{r}), \quad (3.3a)$$

where $q = -e = -1$ is the electron's charge, $\phi(\mathbf{r}, t)$ and $\mathbf{A}(\mathbf{r}, t)$ are the scalar and vector potentials associated with the laser field, respectively, and $V(\mathbf{r})$ is the atomic binding potential. In order to solve this first-order differential equation for $|\Psi(t)\rangle$, it needs to be complemented with an initial state $|\Psi(t_0)\rangle$ for some $t = t_0$. The measurement of a fixed momentum \mathbf{p} at the detector then corresponds to a projection of the final wave function ($|\Psi(t)\rangle$ for $t \rightarrow \infty$) onto a continuum state $|\Psi_{\mathbf{p}}(t)\rangle$ with definite momentum \mathbf{p} . Accordingly, the differential photoionization probability for the emission of an electron with energy $E_{\mathbf{p}} = p^2/2$ into the solid angle element $d\Omega_{\mathbf{p}}$ can be written in the form (Milošević et al., 2006)

$$\mathbb{P}(\mathbf{p}) = |\mathbb{T}_{\mathbf{p}}|^2 \frac{d^3\mathbf{p}}{d\Omega_{\mathbf{p}} dE_{\mathbf{p}}} = p |\mathbb{T}(\mathbf{p})|^2, \quad (3.4)$$

with the transition amplitude of the process,

$$\mathbb{T}(\mathbf{p}) = \lim_{t \rightarrow \infty} \langle \Psi_{\mathbf{p}}(t) | \Psi(t) \rangle. \quad (3.5)$$

¹ Note that the ponderomotive energy does not depend on the laser ellipticity.

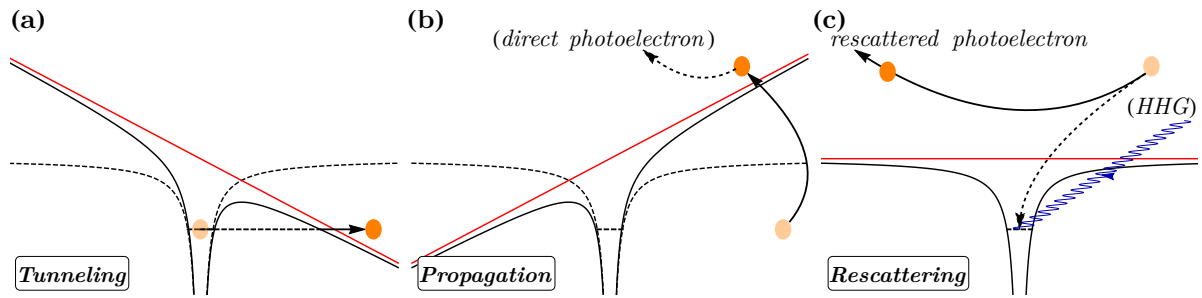


Figure 3.1: Three-step model of ATI. (a) First step: the bound electron (orange) tunnels through the atomic binding potential that is suppressed by the (oscillating) electric field (red) of the laser beam. (b) Second step: the free electron is accelerated in the laser field and may propagate directly to the detector (direct photoelectron). (c) Third step: instead of propagating to the detector, the free electron may rescatter at the parent ion (ATI: rescattered photoelectrons) or recombine with it (HHG: photon emission, blue).

Equations (3.3) already involve approximations. First, a single-electron wave function is used to describe the dynamics of the system (*single-active electron approximation*), which is often sufficient for ATI processes (Milošević et al., 2006). Second, it is assumed that the dynamics of this electron is non-relativistic and can be described by the Schrödinger equation instead of the relativistic Dirac equation. This is true for neutral atomic targets, while relativistic dynamics may be important for highly charged ion targets (Klaiber et al., 2013a). Furthermore, as we will discuss in Chap. 4, first-order relativistic corrections have to be included in order to account for the spatial structure of the laser field. Third, we assume that no ground state depletion occurs in the cloud of target atoms, that is, the concentration of atoms in the ground state does not reduce over the course of the ionization process and we can always assume that our target starts out in the initial state $|\Psi(t_0)\rangle$.

In general, three classes of methods are distinguished to compute the photoionization probability (3.4), representing different levels of approximation. First, the Schrödinger equation (3.3) may be numerically solved without any further approximations [TDSE methods; Kulander, 1987]. Second, analytical solutions can be constructed in which the effect of the laser field on the initial state as well as the influence of the Coulomb potential on the continuum states are (usually) neglected, and continuum-continuum transitions of the photoelectron induced by the laser field are treated in terms of a series expansion. Several such approaches exist, which are combined under the common name SFA and will be the main mathematical tool used in this dissertation² (see Sec. 3.3). Third, the so-called three-step model divides the ionization process into the steps shown in Fig. 3.1 (Krause et al., 1992; Corkum, 1993):

² We will here use the formulation of the SFA that is commonly used in the description of ATI and in the following call it simply *the SFA*.

the electron tunnels through the laser-suppressed atomic potential, propagates in the continuum and, depending on the driving laser field, may rescatter on the ionic core. Several methods make explicit use of the three-step model; in particular, quantum trajectory monte carlo simulations successfully explain many features of PEMDs measured in ATI experiments (Li et al., 2014). Here, the tunneling step is described by Ammosov-Delone-Kraino theory (Ammosov et al., 1986), which yields initial conditions for the free electron in the continuum. Subsequently, the photoelectron is propagated classically for all possible initial conditions. At the detector, these classical paths are finally superposed and weighted by their quantum phase according to Feynman's path integral formulation. Thereby, the quantum features of PEMD can be reproduced based on classical simulations. In fact, the SFA contains the classical trajectories as saddle points of oscillating integrals in the transition amplitude and both methods are closely related (Milošević et al., 2006).

While TDSE methods are most exact, they are limited to simple atomic targets and laser fields due to computational resources. In particular, the spatial dependence of the laser field is usually neglected (*dipole approximation*, see Sec. 3.2) and only plane-wave laser fields are considered. Therefore, to study the influence of the spatial structure of the laser field on the ATI process in a quantum-mechanical model, it is convenient to work within the framework of the SFA. Furthermore, both the SFA and the three-step model provide physical insight into the dynamics of the electron that is hard or impossible to gain from numerical solutions.

3.2 DIPOLE APPROXIMATION

The theoretical analysis of ATI processes, both in numerical and analytical models, is greatly simplified if the driving laser field is considered in the dipole approximation. In this approximation, the spatial dependence of the laser beam's vector potential is neglected, $\mathbf{A}(\mathbf{r}, t) \approx \mathbf{A}(\mathbf{r}_0, t)$ with the position \mathbf{r}_0 of the target atom. According to our discussion in Sec. 2.2, this is equivalent to neglecting the magnetic field of the driving laser, so that the ATI is solely driven by the time-dependent electric field $\mathbf{E}(t)$ of the laser beam.

For twisted laser beams (cf. Sec. 2.4), the vector potential has a considerable spatial dependence and the electric and magnetic fields vary also in the plane transverse to the beam propagation direction. Here, the dipole approximation is in general not justified. In Chap. 7 we will show that it is limited to the description of ATI processes with twisted pulses of very short duration.

In order to determine the conditions under which the dipole approximation is valid for plane-wave laser fields, we have to compare the typical length scale of the

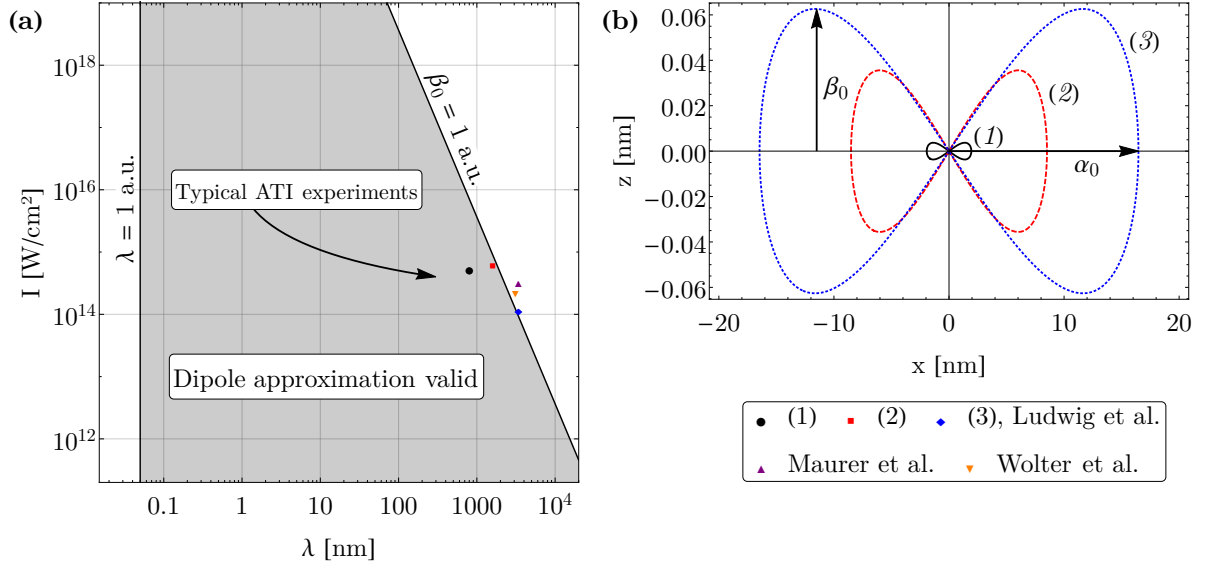


Figure 3.2: Validity of the dipole approximation. (a) Region of validity (gray) depending on laser intensity I and wavelength λ . For $\lambda \leq 1$ a.u., the spatial variation of the laser field over the extension of the initial state wave function is significant, giving a lower bound for λ . If the magnitude β_0 of the photoelectron’s longitudinal motion in the laser field [see (b)] is in the order of 1 a.u., the magnetic field cannot be neglected in the ionization process, giving an upper bound for λ and I . Typical ATI experiments are performed in the vicinity of the $\beta_0 = 1$ a.u. curve. (b) An electron in a linearly polarized laser field performs a figure-eight motion in its average rest frame with amplitudes α_0 and β_0 along the polarization and propagation directions of the field, respectively.

atomic target with the characteristic length scales of the laser field itself, i.e. the wavelength λ , and of the dynamics induced by it. The length scale of the atomic target is given by the extension of the initial state wave function $|\Psi_0(t)\rangle$, which, for the neutral or singly-charged atomic targets considered in this dissertation, is in the order of the Bohr radius $a_0 = 4\pi\epsilon_0\hbar^2/m_e e^2 = 1$ a.u. ≈ 0.05 nm. Therefore, a lower limit on the validity of the dipole approximation is given by the condition that the laser wavelength $\lambda \approx 1$ a.u. Only for $\lambda \gg 1$ a.u. the vector potential can be considered as constant over the extension of the target atom.

In addition, an upper limit exists for the validity of the dipole approximation. This *magnetic displacement limit* is set by the dynamics of the photoelectron in the continuum that plays an essential role in the ionization process [cf. Fig. 3.1 (b) and Sec. 3.3]. Classically, this dynamics is described by the relativistic Lorentz equation for the electron in the combined electric and magnetic fields of the plane-wave laser beam. Solutions to this equation were constructed by Sarachik and Schappert (1970): in its average rest frame, the electron performs a *figure-eight motion* with amplitudes

α_0 and β_0 along the laser polarization and propagation directions, respectively [see Fig. 3.2 (b)]. The amplitude in laser propagation direction is given by (Reiss, 2008)

$$\beta_0 \approx \frac{U_p}{4c\omega} = \frac{E_0^2}{16c\omega^3} \sim I\lambda^3. \quad (3.6)$$

As long as this amplitude is small compared to the Bohr radius, the influence of the magnetic field on the photoelectron dynamics can be neglected (Reiss, 2014). For long wavelengths or high intensities, however, β_0 can be in the order of 1 a.u., where magnetic (or *nondipole*) contributions to the interaction between laser field, photoelectron and the remaining ion can become significant.

The region of validity of the dipole approximation defined by these two limits is illustrated in Fig. 3.2 (a). In typical ATI experiments, indicated in the figure, wavelengths lie in the near- or mid-IR and intensities are in the range $10^{12} - 10^{15}$ W/cm². That is, they always satisfy the condition $\lambda \gg 1$ a.u. but are close to the magnetic displacement limit $\beta_0 = 1$ a.u. Hence, especially for ATI experiments with mid-IR plane-wave laser fields, nondipole contributions to the ionization process can become important. We will discuss them in detail in Chap. 5.

3.3 STRONG-FIELD APPROXIMATION

As briefly mentioned above, the name SFA accommodates several distinct methods. They have developed from different historical beginnings and with the goal to describe the interaction of strong laser fields with different physical systems (Amini et al., 2019). The formulation introduced in this section was explicitly developed to treat ionization problems and has its starting point in the work of Keldysh (1964), which was subsequently extended by Faisal (1973) and by Reiss (1980). Keldysh derived the photoionization probability for atoms in strong laser fields with $\hbar\omega \ll I_p$. He introduced the Keldysh parameter γ to characterize the ionization regime and showed that tunnel and multiphoton ionization can be described within the same formalism when the respective limits of $\gamma < 1$ and $\gamma \gg 1$ are taken. Faisal and Reiss then worked out rigorous derivations of the transition amplitude within an S-matrix formalism that are valid to all orders in the number N of absorbed photons. Therefore, they include also the process of absorbing more photons than needed to overcome the ionization threshold, i.e. ATI.

Since then, the SFA has been extended in several ways, most notably to include Coulomb corrections (Arbó et al., 2008) and nondipole interactions (see Chap. 4). In addition to atomic systems, it has been applied to molecular, two-electron and solid-state systems (Amini et al., 2019).

In this section, we will present a derivation of the transition amplitude $\mathbb{T}(\mathbf{p})$ in the modern formulation of the Keldysh-Faisal-Reiss theory and will closely follow the derivations given by Becker et al. (2002) and Milošević et al. (2006). We begin by writing the Hamiltonian \hat{H} in Eq. (3.3) in the form

$$\hat{H} = \frac{\hat{\mathbf{p}}^2}{2} + V_{\text{le}}(\mathbf{r}, t) + V(\mathbf{r}), \quad (3.7)$$

with the laser-electron interaction potential

$$V_{\text{le}}(\mathbf{r}, t) = \frac{1}{2} \left(\hat{\mathbf{p}} \cdot \mathbf{A}(\mathbf{r}, t) + \mathbf{A}(\mathbf{r}, t) \cdot \hat{\mathbf{p}} + \mathbf{A}^2(\mathbf{r}, t) \right) - \phi(\mathbf{r}, t). \quad (3.8)$$

We will assume that the vector potential $\mathbf{A}(\mathbf{r}, t)$ vanishes asymptotically for $t \rightarrow \pm\infty$. While this is not true for the continuous laser beams often used in theory, a real laser pulse used in experiment has to fulfill this condition since it cannot exert a net force on a charged particle³ (Milošević et al., 2006, appendix A). It follows that both the initial bound state $|\Psi(t_0)\rangle$ and the final continuum state $|\Psi_{\mathbf{p}}(t)\rangle$ are eigenstates of the atomic Hamiltonian $\hat{H}_{\text{A}} = \hat{\mathbf{p}}^2/2 + V(\mathbf{r})$.

In order to take the limit $t \rightarrow \infty$ in the evaluation of the transition amplitude (3.5), the time evolution of the electron's wave function $|\Psi(t)\rangle$ according to the Hamiltonian \hat{H} needs to be known. This time evolution, from an initial time t_0 to a final time t , can be expressed in terms of a unitary time-evolution operator $\hat{U}(t, t_0)$,

$$|\Psi(t)\rangle = \hat{U}(t, t_0) |\Psi(t_0)\rangle, \quad (3.9)$$

which satisfies the Schrödinger equation $i \frac{d}{dt} \hat{U}(t, t_0) = \hat{H} \hat{U}(t, t_0)$, the normalization condition $\hat{U}(t_0, t_0) = 1$ and the property $\hat{U}(t, t_0) = \hat{U}(t, \tau) \hat{U}(\tau, t_0)$ for all τ .

Now, suppose that we decompose the full Hamiltonian (3.7) into two terms, $\hat{H} = \hat{H}_1 + \hat{H}_2$. The so-called Dyson equation then relates the full time evolution operator \hat{U} to the Hamiltonians \hat{H}_1 and \hat{H}_2 ,

$$\hat{U}(t, t_0) = \hat{U}_1(t, t_0) - i \int_{t_0}^t d\tau \hat{U}(t, \tau) \hat{H}_2(\tau) \hat{U}_1(\tau, t_0), \quad (3.10)$$

where \hat{U}_1 is the time evolution operator corresponding to \hat{H}_1 . The same equation is also true if \hat{U}_1 and \hat{U} are interchanged in the integral.

³ Nevertheless, for long pulses, it is convenient and sufficient to model them as continuous laser beam.

If we set $\hat{H}_1 = \hat{H}_A = \hat{p}^2/2 + V(\mathbf{r})$ and $\hat{H}_2 = V_{le}(\mathbf{r}, t)$ and use the Dyson equation, we can rewrite the transition amplitude (3.5) as

$$\begin{aligned}
\mathbb{T}(\mathbf{p}) &= \lim_{t \rightarrow \infty} \langle \Psi_{\mathbf{p}}(t) | \Psi(t) \rangle \\
&= \lim_{t \rightarrow \infty, t_0 \rightarrow -\infty} \langle \Psi_{\mathbf{p}}(t) | \hat{U}(t, t_0) | \Psi_0(t_0) \rangle \\
&= \lim_{t \rightarrow \infty, t_0 \rightarrow -\infty} \left[\langle \Psi_{\mathbf{p}}(t) | \hat{U}_A(t, t_0) | \Psi_0(t_0) \rangle \right. \\
&\quad \left. - i \int_{t_0}^t d\tau \langle \Psi_{\mathbf{p}}(t) | \hat{U}(t, \tau) V_{le}(\mathbf{r}, \tau) \hat{U}_A(\tau, t_0) | \Psi_0(t_0) \rangle \right] \\
&= \lim_{t \rightarrow \infty, t_0 \rightarrow -\infty} \left[\langle \Psi_{\mathbf{p}}(t) | \Psi_0(t) \rangle - i \int_{t_0}^t d\tau \langle \Psi_{\mathbf{p}}(t) | \hat{U}(t, \tau) V_{le}(\mathbf{r}, \tau) | \Psi_0(\tau) \rangle \right].
\end{aligned} \tag{3.11}$$

Since the continuum state $|\Psi_{\mathbf{p}}(t)\rangle$ (for $t \rightarrow \infty$) and the bound state $|\Psi(t_0)\rangle = |\Psi_0(t_0)\rangle$ (for $t_0 \rightarrow -\infty$) are orthogonal eigenstates of the atomic Hamiltonian \hat{H}_A , the first term in the bracket vanishes. In the second term, we make use of the Dyson equation (3.10) again, setting $\hat{H}_1 = \hat{H}_{le} = \hat{p}^2/2 + V_{le}(\mathbf{r}, t)$ and $\hat{H}_2 = V(\mathbf{r})$, and find

$$\begin{aligned}
\mathbb{T}(\mathbf{p}) &= \lim_{t \rightarrow \infty, t_0 \rightarrow -\infty} \left[-i \int_{t_0}^t d\tau \langle \Psi_{\mathbf{p}}(t) | \hat{U}_{le}(t, \tau) V_{le}(\mathbf{r}, \tau) | \Psi_0(\tau) \rangle \right. \\
&\quad \left. + (-i)^2 \int_{t_0}^t d\tau \int_{\tau}^t d\tau' \langle \Psi_{\mathbf{p}}(t) | \hat{U}(t, \tau') V(\mathbf{r}) \hat{U}_{le}(\tau', \tau) V_{le}(\mathbf{r}, \tau) | \Psi_0(\tau) \rangle \right].
\end{aligned} \tag{3.12}$$

This expression is still equivalent to Eq. (3.5), since no further approximations have been made up to this point, apart from those mentioned below Eq. (3.5). However, in order to proceed further, the following assumptions are made within the SFA:

- (1) The atomic binding potential $V(\mathbf{r})$ is neglected in the time evolution of the continuum states; $\hat{U} \approx \hat{U}_{le}$ under the integrals. This is justified since we assume that the laser field is *strong* compared to the binding potential.
- (2) The final state is a plane wave; $|\Psi_{\mathbf{p}}(t)\rangle \approx |\mathbf{p}(t)\rangle$ with $\langle \mathbf{r} | \mathbf{p}(t) \rangle = (2\pi)^{-3/2} e^{i\mathbf{p}\cdot\mathbf{r}} e^{-iE_p t}$ and the photoelectron energy $E_p = p^2/2$.
- (3) The initial state is not coupled to any other atomic bound state by the laser field.

With the first assumption, the time evolution operator $\hat{U} \approx \hat{U}_{le}$ can be expanded in the complete basis of continuum states $|\chi_{\mathbf{k}}(t)\rangle$ of the Hamiltonian \hat{H}_{le} , which are characterized by the momenta \mathbf{k} ,

$$\hat{U}_{le}(t, t') = \int d^3\mathbf{k} |\chi_{\mathbf{k}}(t)\rangle \langle \chi_{\mathbf{k}}(t')|. \tag{3.13}$$

Together with assumptions 2 and 3, this allows us to write Eq. (3.12) as

$$\begin{aligned} \mathbb{T}(\mathbf{p}) = \lim_{t \rightarrow \infty, t_0 \rightarrow -\infty} & \left[-i \int_{t_0}^t d\tau \int d^3\mathbf{k} \langle \mathbf{p}(t) | \chi_{\mathbf{k}}(t) \rangle \langle \chi_{\mathbf{k}}(\tau) | V_{\text{le}}(\mathbf{r}, \tau) | \Psi_0(\tau) \rangle \right. \\ & + (-i)^2 \int_{t_0}^t d\tau \int_{\tau}^t d\tau' \int d^3\mathbf{k} \langle \mathbf{p}(t) | \chi_{\mathbf{k}}(t) \rangle \\ & \left. \times \langle \chi_{\mathbf{k}}(\tau') | V(\mathbf{r}) \hat{U}_{\text{le}}(\tau', \tau) V_{\text{le}}(\mathbf{r}, \tau) | \Psi_0(\tau) \rangle \right]. \end{aligned} \quad (3.14)$$

The limit $t \rightarrow \infty$ can be taken using the identity⁴

$$\lim_{t \rightarrow \infty} \langle \mathbf{p}(t) | \chi_{\mathbf{k}}(t) \rangle = e^{i\varphi_{\infty}} \delta(\mathbf{p} - \mathbf{k}), \quad (3.15)$$

where φ_{∞} is a constant phase that is physically not relevant and can therefore be dropped. If we take the limit in Eq. (3.14) and make use of Eq. (3.15), we arrive at the form of the SFA transition amplitude that is commonly used in ATI problems:

$$\mathbb{T}(\mathbf{p}) = \mathbb{T}_0(\mathbf{p}) + \mathbb{T}_1(\mathbf{p}), \quad (3.16a)$$

$$\mathbb{T}_0(\mathbf{p}) = -i \int_{-\infty}^{\infty} d\tau \langle \chi_{\mathbf{p}}(\tau) | V_{\text{le}}(\mathbf{r}, \tau) | \Psi_0(\tau) \rangle, \quad (3.16b)$$

$$\mathbb{T}_1(\mathbf{p}) = (-i)^2 \int_{-\infty}^{\infty} d\tau \int_{\tau}^{\infty} d\tau' \langle \chi_{\mathbf{p}}(\tau') | V(\mathbf{r}) \hat{U}_{\text{le}}(\tau', \tau) V_{\text{le}}(\mathbf{r}, \tau) | \Psi_0(\tau) \rangle, \quad (3.16c)$$

where $\mathbb{T}_0(\mathbf{p})$ and $\mathbb{T}_1(\mathbf{p})$ are the so-called *direct* and *rescattering* transition amplitudes, respectively. This result has an instructive physical interpretation that directly corresponds to the three-step model described in Sec. 3.1: the direct amplitude $\mathbb{T}_0(\mathbf{p})$ describes an electron that is released from the ground state $|\Psi_0(\tau)\rangle$ under the influence of the laser field (V_{le}), corresponding to the tunneling step in the three-step model, and subsequently propagates ($\langle \chi_{\mathbf{p}}(\tau) |$) in the laser field without feeling the influence of the atomic binding potential. In the rescattering amplitude, the electron is released from the ground state, propagates in the laser field (\hat{U}_{le}) and then scatters at the binding potential $V(\mathbf{r})$, before propagating again under the influence of the laser field. Thus, the rescattering amplitude incorporates the third step of the three-step model. The formal connection between the SFA and the three-step model becomes more explicit in the so-called quantum-orbit theory that arises if a saddle-point approximation is made to evaluate the integrals in Eqs. (3.16) (Kopold et al., 2002).

⁴ It is not clear at this point that this identity is true in general and it strictly holds only in velocity gauge. We will show its validity at the end of Sec. 3.3.1 within the dipole approximation. Note, however, that one may derive the direct transition amplitude $\mathbb{T}_0(\mathbf{p})$ in the form (3.16b) also without the use of this identity (Becker et al., 2002). We can therefore use the direct transition amplitude in this form also for the case that nondipole interactions are included.

For the remainder of this dissertation, we will focus only on the direct transition amplitude and will approximate $\mathbb{T}(\mathbf{p}) \approx \mathbb{T}_0(\mathbf{p})$. While this is a good approximation for circular polarization, we will discuss in Chap. 5 that rescattering contributions are important for linear polarization. When only the direct transition amplitude is considered, it is convenient to perform an integration by parts in Eq. (3.16b) to cast it in a form that is more handy for specific calculations. To this end, we note that $V_{le} = \hat{H}_{le} - \hat{H}_A + V(\mathbf{r})$ in the matrix element in the integral and therefore

$$\begin{aligned} \langle \chi_{\mathbf{p}}(\tau) | V_{le}(\mathbf{r}, \tau) | \Psi_0(\tau) \rangle &= \langle \chi_{\mathbf{p}}(\tau) | \hat{H}_{le} - \hat{H}_A + V(\mathbf{r}) | \Psi_0(\tau) \rangle \\ &= \langle \chi_{\mathbf{p}}(\tau) | -i \frac{\overleftarrow{\partial}}{\partial \tau} - i \frac{\overrightarrow{\partial}}{\partial \tau} + V(\mathbf{r}) | \Psi_0(\tau) \rangle, \end{aligned} \quad (3.17)$$

where we have used the respective Schrödinger equations for $\langle \chi_{\mathbf{p}}(\tau) |$ and $|\Psi_0(\tau)\rangle$. Now, assuming that the vector and scalar potentials are nonzero only within some interval $t_i \leq t \leq t_f$, the direct transition amplitude becomes

$$\begin{aligned} \mathbb{T}_0(\mathbf{p}) &= (-i)^2 \int_{t_i}^{t_f} d\tau \left(\langle \chi_{\mathbf{p}}(\tau) | \frac{\overleftarrow{\partial}}{\partial \tau} + \frac{\overrightarrow{\partial}}{\partial \tau} | \Psi_0(\tau) \rangle \right) - i \int_{t_i}^{t_f} d\tau \langle \chi_{\mathbf{p}}(\tau) | V(\mathbf{r}) | \Psi_0(\tau) \rangle \\ &= - \langle \chi_{\mathbf{p}}(\tau) | \Psi_0(\tau) \rangle \Big|_{t_i}^{t_f} - i \int_{t_i}^{t_f} d\tau \langle \chi_{\mathbf{p}}(\tau) | V(\mathbf{r}) | \Psi_0(\tau) \rangle. \end{aligned} \quad (3.18)$$

In this expression, only the continuum states $|\chi_{\mathbf{p}}(\tau)\rangle$ of the laser-electron interaction Hamiltonian \hat{H}_{le} depend on the laser field. In the derivation above, we have not made any assumptions about its precise form in terms of the scalar and vector potentials $\phi(\mathbf{r}, t)$ and $\mathbf{A}(\mathbf{r}, t)$. In particular, our final expression (3.18) for the direct transition amplitude is valid regardless of the specific temporal and spatial dependence of the potentials. For a given initial bound state $|\Psi_0(\tau)\rangle$, the form of the continuum states in the laser field determines the photoionization probability $\mathbb{P}(\mathbf{p})$, if rescattering contributions are neglected. Thus, in order to compute $\mathbb{P}(\mathbf{p})$ within the SFA, the remaining problem is to find $|\chi_{\mathbf{p}}(\tau)\rangle$. Within the dipole approximation, these states are the so-called Volkov states, which are derived in the next section. If the spatial structure of the laser fields needs to be included, Volkov-type states are required that go beyond the dipole approximation. We will derive such *nondipole Volkov states* in Chap. 4 and they will allow us to treat nondipole effects within the SFA.

The SFA derived in the above form is generally expected to be valid in the tunneling regime $\gamma < 1$ and has been applied to many experimental scenarios in this regime (Amini et al., 2019). According to the definition of the Keldysh parameter (3.1), for $\gamma < 1$ the strength of the atomic binding potential (given by I_p) is small compared to the strength of the laser-electron interaction (given by U_p). In turn, this justifies our

assumption (1) above and allows us to neglect the binding potential in the electron continuum.

3.3.1 Volkov states in dipole approximation

The continuum states of an electron in an oscillating electromagnetic field were first derived by Volkow (1935). In this original work, these states were obtained as solutions to the Dirac equation and for a laser field that can be written as superpositions of monochromatic plane waves with parallel wave vectors. Here, we will focus on non-relativistic Volkov states, which are solutions to the Schrödinger equation

$$i \frac{d}{dt} |\chi(t)\rangle = \hat{H}_{le} |\chi(t)\rangle, \quad \hat{H}_{le} = \frac{\hat{\mathbf{p}}^2}{2} + V_{le}(\mathbf{r}, t), \quad (3.19)$$

where the dipole approximation (cf. Sec. 3.2) is made in $V_{le}(\mathbf{r}, t)$. The form of the laser-electron interaction potential (3.8) depends on the gauge used for the laser field. In the following, we will derive the Volkov states in the so-called length and velocity gauges and we will briefly discuss which gauge is used within the SFA in Sec. 3.3.2. The *length gauge* is defined by a vanishing vector potential, $\mathbf{A}(t) = 0$. The relation (2.2a) between the potentials and the electric field then implies $\phi(\mathbf{r}, t) = -\mathbf{r} \cdot \mathbf{E}(t)$ and, consequently, the interaction potential is given by

$$V_{le}(\mathbf{r}, t) = -\phi(\mathbf{r}, t) = \mathbf{r} \cdot \mathbf{E}(t). \quad (3.20)$$

The *velocity gauge*, on the other hand, is defined by a vanishing scalar potential, $\phi(\mathbf{r}, t) = 0$, and therefore

$$V_{le}(\mathbf{r}, t) = \mathbf{A}(t) \cdot \hat{\mathbf{p}} + \frac{1}{2} \mathbf{A}^2(t). \quad (3.21)$$

It can be easily verified that the gauge transformation function in (2.3) for the gauge transform from velocity to length gauge is given by $f(\mathbf{r}, t) = -\mathbf{r} \cdot \mathbf{A}(t)$.

The Volkov states can be readily derived in velocity gauge, in which the Schrödinger equation (3.19) in momentum space reads

$$i \frac{\partial}{\partial t} \chi(\mathbf{p}, t) = \frac{1}{2} (\mathbf{p} + \mathbf{A}(t))^2 \chi(\mathbf{p}, t), \quad (3.22)$$

and can be integrated in time to give

$$\chi(\mathbf{p}, t) = e^{-iS_V(t)}, \quad S_V(t) = \frac{1}{2} \int^t d\tau (\mathbf{p} + \mathbf{A}(\tau))^2, \quad (3.23)$$

where $S_V(t)$ is called the *Volkov phase*. Performing the inverse Fourier transform from momentum to position space leads to

$$\chi(\mathbf{r}, t) = \frac{1}{(2\pi)^{3/2}} \int d^3\mathbf{p} e^{-iS_V(t)} e^{i\mathbf{p}\cdot\mathbf{r}}. \quad (3.24)$$

Thus, the general position space wave function is a superposition of Volkov states

$$\chi_{\mathbf{p}}^{(\text{VG})}(\mathbf{r}, t) = \frac{1}{(2\pi)^{3/2}} e^{-iS_V(t)} e^{i\mathbf{p}\cdot\mathbf{r}}, \quad S_V(t) = \frac{1}{2} \int^t d\tau (\mathbf{p} + \mathbf{A}(\tau))^2, \quad (3.25)$$

which are characterized by the momentum \mathbf{p} .

In order to obtain the Volkov states in length gauge, we use the fact that a gauge transform (2.3) induces a phase shift in the wave function,

$$\chi_{\mathbf{p}}^{(\text{LG})}(\mathbf{r}, t) = \chi_{\mathbf{p}}^{(\text{VG})}(\mathbf{r}, t) e^{-if(\mathbf{r}, t)} = \frac{1}{(2\pi)^{3/2}} e^{-iS_V(t)} e^{i(\mathbf{p} + \mathbf{A}(t))\cdot\mathbf{r}}, \quad (3.26)$$

where we inserted $f(\mathbf{r}, t) = -\mathbf{r} \cdot \mathbf{A}(t)$.

With the explicit form of the dipole Volkov states in velocity gauge, we are now in a position to derive the identity (3.15) used in the derivation of the SFA transition amplitude (3.16):

$$\begin{aligned} \lim_{t \rightarrow \infty} \langle \mathbf{p}(t) | \chi_{\mathbf{k}}^{(\text{VG})}(t) \rangle &= \lim_{t \rightarrow \infty} e^{iE_{\mathbf{p}}t} e^{-iS_V(t)} \frac{1}{(2\pi)^3} \int d^3\mathbf{r} e^{-i(\mathbf{p}-\mathbf{k})\cdot\mathbf{r}} \\ &= \lim_{t \rightarrow \infty} e^{iE_{\mathbf{p}}t} e^{-iS_V(t)} \delta(\mathbf{p} - \mathbf{k}) \\ &= e^{i\varphi_{\infty}} \delta(\mathbf{p} - \mathbf{k}), \end{aligned} \quad (3.27)$$

with a constant real phase φ_{∞} . In the same way, we find in length gauge that

$$\lim_{t \rightarrow \infty} \langle \mathbf{p}(t) | \chi_{\mathbf{k}}^{(\text{LG})}(t) \rangle = e^{i\varphi_{\infty}} \delta(\mathbf{p} - \mathbf{k} - \mathbf{A}(t_f)), \quad (3.28)$$

where $\mathbf{A}(t_f)$ is the final value of the vector potential at the end of the laser pulse. The direct SFA transition amplitude in length gauge can therefore be obtained from the direct transition amplitude (3.18) in velocity gauge by replacing the momentum \mathbf{p} characterizing the Volkov states by the momentum $\tilde{\mathbf{p}} = \mathbf{p} - \mathbf{A}(t_f)$.

3.3.2 Choice of gauge

Since measurable quantities like the ionization probability $\mathbb{P}(\mathbf{p})$ are gauge invariant, the general transition amplitude (3.5) does not depend on the gauge used for the laser field. However, approximations have been made in the derivation of the SFA transition

amplitude (3.16), rendering the results obtained in SFA-based calculations gauge-dependent. This is especially so if only the direct transition amplitude is considered, $\mathbb{T}(\mathbf{p}) \approx \mathbb{T}_0(\mathbf{p})$, and it is therefore important to choose a gauge that leads to results for the photoionization probability that agree with experiments. This problem has been addressed by Bauer et al. (2005). The authors compared the ATI spectra obtained from the direct SFA transition amplitude in velocity and length gauge, respectively, with numerical solutions of the Schrödinger equation for different initial states $|\Psi_0(t)\rangle$. It was found that the SFA calculations in length gauge yield correct results independent of the symmetry of the initial state, while the velocity gauge calculations were only in agreement with the numerical solutions for spherically symmetric s -states, leading to the conclusion that the length gauge should generally be preferred in SFA calculations.

One goal of this dissertation is to incorporate nondipole contributions to the laser-electron interaction within the SFA. In general, the vector and scalar potentials that describe the laser field will then depend on both \mathbf{r} and t . In this case, however, the length gauge does not exist, since $\mathbf{A}(\mathbf{r}, t) = 0$ cannot be achieved by any gauge transformation due to the spatial degrees of freedom of the laser field. Since we will only consider $1s$ initial states in our explicit calculations, we will work in velocity gauge for the remainder of this dissertation. It should, however, be kept in mind that the question of gauge dependence of nondipole SFA theories needs to be addressed in the future, especially if it is applied to less symmetric initial states.

3.4 ATI WITH PLANE-WAVE BEAMS AND PULSES

In this section, we apply the SFA formalism in dipole approximation to the ATI of an atomic target with plane-wave laser pulses of the form (2.12). We will focus on circular polarization ($\varepsilon = 1$) for which any rescattering of the photoelectron with the parent ion is suppressed and we can neglect the rescattering amplitude in Eq. (3.16).

We consider an atomic target, initially in a hydrogen-like $1s$ initial state of the form

$$\Psi_0(\mathbf{r}, t) = \Phi_0(r)e^{iI_p t} = \frac{(2I_p)^{3/4}}{\sqrt{\pi}} e^{-\sqrt{2I_p}r} e^{iI_p t}, \quad (3.29)$$

where the ionization potential I_p is adapted to the experimental target in question and we will here set $I_p = 14$ eV, applicable to Krypton. The atomic binding potential $V(\mathbf{r})$ is modeled simply as a Coulomb potential (Milošević et al., 2006). Upon ionization of the atom, a photoelectron is emitted with momentum $\mathbf{p} = (p, \vartheta_p, \varphi_p)$. At the detector, the photoionization probability (3.4) is measured in terms of the relative number of photoelectrons emitted with this momentum.

It is instructive to consider a continuous driving laser beam before turning to a pulse of finite duration. For the vector potential (2.12) in dipole approximation ($z = 0$) and with $\varepsilon = 1$, $\mathbf{A}(\mathbf{r}, t) = \frac{A_0}{\sqrt{2}} (\cos(\omega t) \mathbf{e}_x + \varepsilon \sin(\omega t) \mathbf{e}_y)$, the velocity gauge Volkov phase in Eq. (3.25) reads [cf. Eq. (B.8) in App. B]

$$S_V(t) = E_p t + \frac{A_0^2}{4} t + \frac{p_x A_0}{\sqrt{2}\omega} \sin(\omega t) - \frac{p_y A_0}{\sqrt{2}\omega} \cos(\omega t). \quad (3.30)$$

Upon insertion of Eq. (3.25) with $S_V(t)$ and the initial state (3.29) into the direct SFA transition amplitude (3.18), we obtain⁵

$$\mathbb{T}_0(\mathbf{p}) = -iV(\mathbf{p}) \int_{-\infty}^{\infty} d\tau e^{i(I_p + S_V(t))}, \quad (3.31)$$

where the matrix element of the Coulomb potential is given by

$$V(\mathbf{p}) = \langle \mathbf{p} | V(\mathbf{r}) | \Phi_0 \rangle = \frac{1}{(2\pi)^{3/2}} \int d^3\mathbf{r} \frac{e^{-\sqrt{2}I_p r}}{r} e^{-i\mathbf{p}\cdot\mathbf{r}} = -\frac{2^{3/4} I_p^{5/4}}{\pi} \frac{1}{\frac{p^2}{2} + I_p}. \quad (3.32)$$

In order to evaluate Eq. (3.31) further, we apply the Jacobi-Anger expansion (cf. App. A) to the exponential of the Volkov phase,

$$\begin{aligned} \mathbb{T}_0(\mathbf{p}) &= -iV(\mathbf{p}) \sum_{n,m=-\infty}^{\infty} (-i)^m J_n \left(\frac{p_x A_0}{\sqrt{2}\omega} \right) J_m \left(\frac{p_y A_0}{\sqrt{2}\omega} \right) \int_{-\infty}^{\infty} d\tau e^{i(E_p + E_{nm})} \\ &= -2\pi i V(\mathbf{p}) \sum_{n,m=-\infty}^{\infty} (-i)^m J_n \left(\frac{p_x A_0}{\sqrt{2}\omega} \right) J_m \left(\frac{p_y A_0}{\sqrt{2}\omega} \right) \delta(E_p + E_{nm}), \end{aligned} \quad (3.33)$$

where $J_l(x)$ are the Bessel functions of the first kind, δ is the Dirac delta function and $E_{nm} = I_p + U_p + (n+m)\omega$ with the ponderomotive potential $U_p = A_0^2/4$ defined in the beginning of the chapter.

Due to the symmetry of the continuous circularly polarized plane-wave beam in the $x-y$ -plane, the direct transition amplitude (3.31) is symmetric in p_x and p_y . This is in contrast to linearly polarized beams, where the photoelectron is most likely emitted along the polarization direction. For simplicity, we can therefore set $p_x = p$ and $p_y = 0$ and use $J_m(0) = \delta_{m,0}$ to eliminate the sum over m . The differential photoionization probability (3.4) for emission in the polarization plane is then

$$\mathbb{P}(E_p) = (2\pi)^2 \sqrt{2E_p} V^2(\sqrt{2E_p}) \sum_{n=-\infty}^{\infty} J_n^2 \left(\frac{\sqrt{2E_p} A_0}{\sqrt{2}\omega} \right) \delta^2(I_p + E_p + U_p + n\omega). \quad (3.34)$$

⁵ Note that the first term in the direct transition amplitude (3.18) vanishes for a continuous beam.

Here, we replaced $p = \sqrt{2E_p}$ to obtain the energy spectrum of the photoelectrons measured by a detector along a particular direction. This spectrum is commonly called the *ATI spectrum* and it is helpful to examine the meaning of the terms in Eq. (3.34): the delta function defines peaks in the ATI spectrum and its argument defines their specific positions $E_n = n\omega - U_p - I_p$, spaced by the photon energy ω . These are the ATI peaks indicated in Fig. 1.1 (b). The magnitudes of the ATI peaks are defined by the respective prefactors of the delta function, $P_n = \mathbb{P}(E_n) \sim J_n^2\left(\frac{\sqrt{2E_n}A_0}{\sqrt{2}\omega}\right)$. The relation for E_n now allows the following interpretation: via absorption of n photons from the laser beam, the bound electron can overcome the ionization threshold I_p and the classical ponderomotive potential U_p to enter the continuum and absorb even more photons, depending on \mathbb{P}_n . Of course, it cannot absorb an arbitrary number of photons. Instead, the Bessel functions in the photoionization probability define a *cut-off*, i.e. a maximum number $n = n_{\max}$ beyond which \mathbb{P}_n drops off exponentially. Since $J_n(x) \sim e^{-n}$ for $n > x$, this cut-off is given by the relation $n_{\max}^2 = \sqrt{2E_{n_{\max}}}A_0/\sqrt{2}\omega$ and increases with both the intensity (via A_0) and the wavelength (via ω).

The sharply defined ATI peaks for a continuous laser beam are a result of an averaging over many optical cycles in the temporal integral in the transition amplitude (3.31). For a realistic pulse of finite duration, the integral runs only over the pulse duration T_p and, as a result, the ATI peaks are broadened: in the dipole approximation, the vector potential (2.21) of a plane-wave pulse with the pulse envelope (2.22) reads

$$\mathbf{A}^{(P)}(t) = \frac{A_0}{\sqrt{1 + \varepsilon^2}} \sin^2\left(\frac{\omega t}{2n_p}\right) (\cos(\omega t + \phi_{\text{CEP}}) \mathbf{e}_x + \varepsilon \Lambda \sin(\omega t + \phi_{\text{CEP}}) \mathbf{e}_y), \quad (3.35)$$

for $0 \leq t \leq T_p = n_p T$ and $\mathbf{A}^{(P)}(t) = 0$ otherwise.

The explicit form of the Volkov phase in (3.25) resulting from this vector potential is rather cumbersome and we state it in App. B. For circular polarization [see Eq. (B.6)], it may be directly compared to the expression (3.30) for the continuous beam. As a result of the \sin^2 –envelope in Eq. (3.35), the Volkov phase not only contains trigonometric functions of frequency ω , but also terms oscillating with frequencies $(1 \pm 1/n_p)\omega$, ω/n_p and $2\omega/n_p$, depending on the number of optical cycles n_p comprising the driving pulse. These additional frequencies in the Volkov phase have a pronounced impact on the ATI spectra: the direct SFA transition amplitude is now given by

$$\mathbb{T}_0(\mathbf{p}) = -\langle \mathbf{p} | \Phi_0 \rangle e^{i(I_p t + S_V(t))} \Big|_0^{T_p} - iV(\mathbf{p}) \int_0^{T_p} d\tau e^{i(I_p + S_V(t))}, \quad (3.36)$$

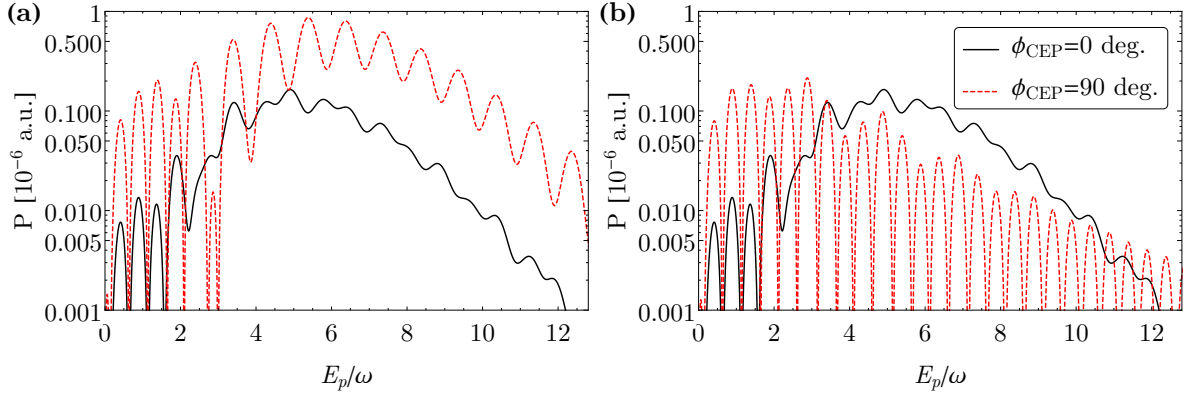


Figure 3.3: ATI spectra for a 2-cycle plane-wave pulse for two different values of the carrier-envelope phase ϕ_{CEP} . The spectra are shown for photoelectrons emitted in the polarization plane ($p_z = 0$) along the (a) positive ($\varphi_p = 0$) and (b) negative ($\varphi_p = \pi$) x -direction, respectively. Parameters used: $n_p = 2$, $\lambda = 800$ nm, $I_{\text{max}} = 10^{14}$ W/cm 2 , $I_p = 14$ eV (Krypton target).

where $V(\mathbf{p})$ is given by Eq. (3.32) and $\langle \mathbf{p} | \Phi_0 \rangle$ denotes the Fourier transform of the initial state wave function (3.29),

$$\langle \mathbf{p} | \Phi_0 \rangle = \frac{(2I_p)^{5/4}}{\pi\sqrt{2}} \frac{1}{(\frac{p^2}{2} + I_p)^2}. \quad (3.37)$$

If, as before, the Jacobi-Anger expansion is applied to the exponential of $S_V(t)$ in the integral above, each term in the Volkov phase (B.6) leads to an infinite sum similar to Eq. (3.31). Since these terms are coherently summed in the transition amplitude, they do not lead to the sharp ATI peaks that we found for continuous beams.

Instead, the energy spectra $P(E_p)$ of the photoelectrons shown in Fig. 3.3 are found, which are extensively discussed by Milošević et al. (2006). The ATI peaks are visible but they are broadened due to interferences of the different terms in the transition amplitude. Moreover, we see a dependence on the carrier-envelope phase ϕ_{CEP} . While for $\phi_{\text{CEP}} = \pi/2$, the spectra measured in opposite directions along the x -axis are identical, they differ strongly for $\phi_{\text{CEP}} = 0$. This difference due to the asymmetry of the vector potential (3.35) in the $x - y$ -plane was utilized by Paulus et al. (2001) to determine ϕ_{CEP} from ATI experiments. If the pulse duration is increased, the asymmetry disappears.

The SFA in dipole approximation explains many features of ATI spectra that have been measured in the past and, in addition to the discussion above, also rescattering effects can successfully be described (Milošević et al., 2006). Our considerations here have, however, neglected any nondipole contributions to the photoelectron dynamics and we will develop a nondipole formulation of the SFA in the next chapter. The present discussion will then be extended including nondipole interactions in Chap. 5.

NONDIPOLE SFA FOR SPATIALLY STRUCTURED LASER FIELDS

In this chapter, we will present an extension of the SFA to include also nondipole interactions between the driving laser field and the photoelectron in the continuum. We will discuss the need for such an extension and state the precise formulation of the problem in the first section. There, we will also give an overview of previous work in this direction. In Sec. 4.2, we will then turn to the derivation of so-called nodipole Volkov states for spatially structured laser fields, which form the basis of the nondipole SFA.

Parts of the material presented in this chapter were published previously in the following reference:

Nondipole strong-field approximation for spatially structured laser fields

B. Böning, W. Paufler, and S. Fritzsche

PHYSICAL REVIEW A **99**, 053404 (2019)

4.1 NONDIPOLE SFA THEORIES

In the previous chapter, we have dealt with the description of ATI processes of atomic targets in the dipole approximation, where the driving laser field is approximated at the position of the target atom as a purely time-dependent function. However, we saw in Sec. 3.2 that it is not always allowed to make this approximation. In particular, if the ionization is driven by a plane-wave laser field of sufficiently long wavelength, the dynamics of the photoelectron is significantly altered by the spatial dependence of the laser field, or, equivalently, its magnetic field. In Chap. 5, we will discuss the ATI driven by mid-IR plane-wave laser fields in more detail and, as a particular consequence of nondipole interactions, we will analyze the characteristic peak shifts in the PEMD (Smeenk et al., 2011). Besides, the driving laser field may exhibit a more complex spatial dependence than a plane wave. As a first example, realistic laser beams used in experiments often have an intensity profile that decreases with the radial distance to the beam axis. Such beams are commonly described as Gaussian

laser beams (Saleh and Teich, 1991, chapter 3), where this radial dependence is a Gaussian function. Another example has been introduced in Sec. 2.4 in the form of twisted light beams, whose intensity profile varies strongly with the radial distance as a result of a non-vanishing orbital angular momentum. In general, one cannot expect that the theoretical description of the interaction between such laser fields and matter can be satisfactorily described under the assumption of the dipole approximation (Quinteiro et al., 2017a; Quinteiro et al., 2017b). Indeed, in ionization or excitation scenarios of atoms by weak-field twisted light beams, higher-order multipoles play a significant role (Matula et al., 2013; Scholz-Marggraf et al., 2014).

To properly account for nondipole interactions in the theoretical description of ATI or other strong-field processes, the frameworks developed over the past decades have to be extended. For plane-wave laser fields, several works have incorporated these interactions based on numerical simulations (Brennecke and Lein, 2018) as well as semi-classical methods (Willenberg et al., 2019). Most importantly for us, several versions of nondipole SFA theories have been developed in the past and we will discuss them in Sec. 4.1.2. Of particular significance is the work of Rosenberg and Zhou (1993), who derived (non-relativistic) Volkov states that describe an electron in a laser field formed by a *discrete* finite superposition of plane waves. This provides a starting point for the work presented in Sec. 4.2.

4.1.1 Formulation of the problem

In this chapter, we will focus on the extension of the SFA description of ATI processes introduced in Sec. 3.3 towards laser fields of an *arbitrary* spatial dependence. Not only will this allow to treat plane-wave fields, but it will also provide a formalism to account for a more complex \mathbf{r} -dependence of the vector potential. More precisely, we will start from a vector potential¹ that is written as an integral superposition of plane-wave modes,

$$\mathbf{A}(\mathbf{r}, t) = \int d^3\mathbf{k} \mathbf{A}(\mathbf{k}, t), \quad (4.1a)$$

$$\mathbf{A}(\mathbf{k}, t) = \text{Re} \left\{ \mathbf{a}(\mathbf{k}) e^{i\mathbf{u}_{\mathbf{k}}} \right\}, \quad (4.1b)$$

with the wave vector \mathbf{k} and the (complex) Fourier coefficients $\mathbf{a}(\mathbf{k})$ that characterize the spatial dependence. For convenience, we have introduced the notation $\mathbf{u}_{\mathbf{k}} = \mathbf{u}_{\mathbf{k}}(\mathbf{r}, t) = \mathbf{k} \cdot \mathbf{r} - \omega_{\mathbf{k}}t$ with the frequencies $\omega_{\mathbf{k}} = kc$ of the individual modes given by the dispersion relation. Here and for the remainder of this chapter, we will drop

¹ We will work in velocity gauge in which the scalar potential $\phi(\mathbf{r}, t) = 0$. See Sec. 3.3.2 for a discussion of the choice of gauge in the nondipole case.

the explicit \mathbf{r} - and t -dependencies of $u_{\mathbf{k}}$. One can see that starting from the vector potential in the form (4.1) makes it possible to describe quite general classes of laser fields, e.g. the vector potential of a twisted Bessel beam (2.25) is readily given in the form (4.1). Also, if we set $\mathbf{a}(\mathbf{k}) = \frac{A_0}{\sqrt{1+\varepsilon^2}}(\mathbf{e}_1 + i\varepsilon\Lambda\mathbf{e}_2)\delta(\mathbf{k} - \mathbf{k}_0)$, we recover the elliptically polarized plane-wave laser beam (2.15) that propagates along the \mathbf{k}_0 -direction (cf. Sec. 5.3.1).

Our aim is to construct an SFA formalism that allows us to treat driving laser fields of the form (4.1). Since we did not make any assumptions about the laser field in the derivation leading to the SFA transition amplitude (3.16) and the particular form of the direct transition amplitude (3.18), these equations are still valid here. For the remainder of this dissertation, we will be concerned only with the direct transition amplitude, which we state here again for convenience:

$$\mathbb{T}_0(\mathbf{p}) = - \langle \chi_{\mathbf{p}}(\tau) | \Psi_0(\tau) \rangle \Big|_{t_i}^{t_f} - i \int_{t_i}^{t_f} d\tau \langle \chi_{\mathbf{p}}(\tau) | V(\mathbf{r}) | \Psi_0(\tau) \rangle. \quad (4.2)$$

The laser-electron interaction operator $V_{le}(\mathbf{r}, t) = \mathbf{A}(\mathbf{r}, t) \cdot \hat{\mathbf{p}} + \frac{1}{2}\mathbf{A}^2(\mathbf{r}, t)$ has been replaced by the atomic binding potential $V(\mathbf{r})$ in this expression via the partial integration in Eq. (3.18). This is of great advantage in the present case, where the laser field may possess a complex \mathbf{r} -dependence that renders the evaluation of (matrix elements of) $V_{le}(\mathbf{r}, t)$ cumbersome. In the transition amplitude (4.2), then, the only point where the laser field enters the formalism is through the Volkov states $|\chi_{\mathbf{p}}(\tau)\rangle$ that describe the dynamics of the photoelectron in the presence of the laser field.

Accordingly, the goal of this chapter will be to derive an expression of these Volkov states $|\chi_{\mathbf{p}}(\tau)\rangle$, which accounts for the full spatial dependence of the vector potential $\mathbf{A}(\mathbf{r}, t)$. In other words, we will construct solutions to the Schrödinger equation

$$i \frac{d}{dt} |\chi(t)\rangle = \hat{H}_{le} |\chi(t)\rangle, \quad \hat{H}_{le} = \frac{\hat{\mathbf{p}}^2}{2} + \mathbf{A}(\mathbf{r}, t) \cdot \hat{\mathbf{p}} + \frac{1}{2}\mathbf{A}^2(\mathbf{r}, t), \quad (4.3)$$

with $\mathbf{A}(\mathbf{r}, t)$ given by Eqs. (4.1). Together with Eq. (4.2), such solutions will then result in an SFA theory that allows us to describe ATI processes of atoms driven by laser fields of an arbitrary spatial dependence. Since this treatment goes beyond the dipole approximation, such a theory is commonly called *nondipole* SFA and the corresponding Volkov states are called nondipole Volkov states. In order to distinguish our result from other nondipole SFA theories applicable to plane-wave fields, we will call it *nondipole SFA for spatially structured laser fields*. According to our discussion in Sec. 2.2, this SFA will then be capable of accounting for the magnetic field of the driving laser beam or, equivalently, the photon momentum.

4.1.2 Previous approaches

Originally, wave functions for an electron in an oscillating electromagnetic field were derived by Volkov (1935) as solutions to the (relativistic) Dirac equation for a light field which can be written as a superposition of (co-propagating) plane waves with different frequencies. These *Dirac-Volkov states* give rise to a relativistic SFA. If only the linear term in an expansion of the Dirac-Volkov states in $1/c$ is accounted for, a so-called *quasi-relativistic* SFA is obtained, which accounts for nondipole interactions in non-relativistic scenarios. In particular, it has been shown that radiation pressure effects are included in this quasi-relativistic SFA and that the momentum transfer from photons to the photoelectron (peak shifts; see Chap. 5) in ATI with a plane-wave laser field can be calculated in good agreement with the relativistic SFA (Krajewska and Kaminski, 2015).

Another approach by Titi and Drake (2012) uses the Henneberger transform to obtain approximate nondipole Volkov states as solutions to the Schrödinger equation and also compute the peak shifts within the SFA. While their work is also limited to plane-wave laser beams, the authors additionally account for the Coulomb potential of the ion in the Volkov states.

An *exact* solution to the Schrödinger equation for an electron in a plane-wave laser field was constructed by He et al. (2017). These exact non-relativistic nondipole Volkov states have the form $\psi_{\mathbf{p}}(\mathbf{r}, t) = (2\pi)^{-3/2} \exp(-iE_{\mathbf{p}}t + i\mathbf{p} \cdot \mathbf{r})f(t - z/c)$ with a function f that includes a Volkov-type phase. The authors discuss the relation to the dipole Volkov states and also analyze the peak shifts in ATI.

Finally, we mention the work of Rosenberg and Zhou (1993), which provides the starting point for our derivation below. Here, the authors considered a vector potential that is formed by a discrete superposition of plane-wave modes,

$$\mathbf{A}(\mathbf{r}, t) = \sum_{j=1}^N \mathbf{A}_j(u_j), \quad (4.4)$$

where $\mathbf{A}(u_j) = \text{Re} \{ \mathbf{a}_j \exp(iu_j) \}$ with $u_j = \mathbf{k}_j \cdot \mathbf{r} - \omega_j t$ and amplitudes \mathbf{a}_j . We can see that our general form (4.1) of the vector potential is very similar to Eq. (4.4), however, we allow for *continuous* instead of discrete superpositions. Rosenberg and Zhou (1993) then constructed approximate Volkov-type solutions to the Schrödinger equation, which have the form $\psi_{\mathbf{p}} = (2\pi)^{-3/2} \exp(-iE_{\mathbf{p}}t + i\mathbf{p} \cdot \mathbf{r})f(u_1, \dots, u_N)$, where f is an initially unknown function of the u_j defining the vector potential. The authors did not examine ionization processes but considered transitions between these Volkov states, which describe laser-assisted scattering processes.

4.2 NONDIPOLE VOLKOV STATES FOR INTEGRAL SUPERPOSITIONS OF PLANE WAVES

We have seen above that previous approaches to incorporate nondipole interactions within the SFA have focused on either plane-wave driving beams or discrete superpositions of them. Therefore, Gaussian or twisted light beams are not incorporated within these formalisms. We now turn to the more general case of a vector potential that is written as an integral superposition of plane waves, given by Eq. (4.1), and derive nondipole Volkov states for an electron in such a laser field.

4.2.1 Solution of the Schrödinger equation

In order to construct solutions to the Schrödinger equation (4.3) with the vector potential (4.1), we follow lines similar to those of Rosenberg and Zhou (1993) for discrete superpositions. In position space, we make the ansatz

$$\chi_{\mathbf{p}}(\mathbf{r}, t) = \frac{1}{(2\pi)^{3/2}} e^{-i(E_{\mathbf{p}}t - \mathbf{p}\cdot\mathbf{r})} f(\mathbf{r}, t) \quad (4.5)$$

for the wave function of the electron. Here $E_{\mathbf{p}} = p^2/2$ and we assume that the wave function can be characterized by a momentum \mathbf{p} as in the dipole approximation. Indeed, this is the momentum that is measured at the detector when the laser field is asymptotically turned off. Our ansatz (4.5) represents a plane-wave solution factorized by an unknown function $f(\mathbf{r}, t)$. Thus, for $\mathbf{A}(\mathbf{r}, t) = 0$ we expect that $f(\mathbf{r}, t) = 1$ and we recover the solution for a free electron.

To find the function $f(\mathbf{r}, t)$, we write it as a *functional* of the functions $u_{\mathbf{k}}$ that appear in the vector potential (4.1),

$$f(\mathbf{r}, t) = f[u_{\mathbf{k}}(\mathbf{r}, t)] = f[u_{\mathbf{k}}]. \quad (4.6)$$

Upon insertion of our ansatz (4.5) into the Schrödinger equation (4.3), we then obtain a functional integro-differential equation for f in which we neglect the second derivatives of f since they lead only to higher-order relativistic corrections (Rosenberg and Zhou, 1993). To reexpress the Schrödinger equation (4.3), we need to use the product rule in the derivatives of Eq. (4.5) and the fact that

$$\frac{\partial f[u_{\mathbf{k}}]}{\partial x_j} = \int d^3\mathbf{k}' \frac{\delta f[u_{\mathbf{k}}]}{\delta u_{\mathbf{k}'}} \frac{\partial u_{\mathbf{k}'}}{\partial x_j}, \quad (4.7)$$

where x_j may stand for x, y, z and t , and where we used the functional derivative with respect to $u_{\mathbf{k}}(\mathbf{r}, t)$, defined as (Gelfand and Fomin, 2000)

$$\frac{\delta f[u_{\mathbf{k}}]}{\delta u_{\mathbf{k}}} = \lim_{\epsilon \rightarrow 0} \frac{f[u_{\mathbf{k}} + \epsilon h] - f[u_{\mathbf{k}}]}{\epsilon}, \quad (4.8)$$

for an arbitrary test function h . The functional derivative satisfies the usual rules of differentiation and can therefore be evaluated according to them for our purposes.

The resulting equation for the functional f then has the form

$$i \int d^3 \mathbf{k}' \eta_{\mathbf{k}'} \frac{\delta f[u_{\mathbf{k}}]}{\delta u_{\mathbf{k}'}} \approx \frac{1}{2} \left(-2i \mathbf{A}(\mathbf{r}, t) \cdot \nabla + 2 \mathbf{A}(\mathbf{r}, t) \cdot \mathbf{p} + \mathbf{A}^2(\mathbf{r}, t) \right) f[u_{\mathbf{k}}], \quad (4.9)$$

where we introduced $\eta_{\mathbf{k}} = \mathbf{p} \cdot \mathbf{k} - \omega_{\mathbf{k}}$. In order to proceed from this equation, we decompose $f[u_{\mathbf{k}}]$ in the form

$$f[u_{\mathbf{k}}] = f^{(0)}[u_{\mathbf{k}}](1 + g[u_{\mathbf{k}}]), \quad (4.10)$$

where $f^{(0)}$ solves Eq. (4.9) if the gradient term proportional to $\mathbf{A}(\mathbf{r}, t) \cdot \nabla f^{(0)}$ is neglected, and g provides a subsequent correction to this zeroth-order approximation $f^{(0)}$. Accordingly, solving the Schrödinger equation now amounts to finding $f^{(0)}$ and g as functionals of $u_{\mathbf{k}}$. From here, we continue in two steps: first, we approximate $f \approx f^{(0)}$, neglect the gradient term and solve the resulting integro-differential equation. Second, with the solution for $f^{(0)}$, we return to Eq. (4.10) and the full Schrödinger equation in the form (4.9), which then becomes an equation for g upon insertion. It turns out that this equation can indeed be solved, if we keep only terms of first order in $f^{(0)}$ and g in the gradient term proportional to $\mathbf{A}(\mathbf{r}, t) \cdot \nabla f$. We will argue that the resulting approximate solution $\chi_{\mathbf{p}}(\mathbf{r}, t)$ to the Schrödinger equation can be considered exact since any further correction would be of order $(v/c)^2$ in the photoelectron velocity v .

For convenience, we now make the following definitions² in analogy with Rosenberg and Zhou (1993):

$$\mathbf{p} \cdot \mathbf{A}(\mathbf{k}, t) = \lambda_{\mathbf{k}} \cos(u_{\mathbf{k}} + \theta_{\mathbf{k}}), \quad (4.11a)$$

$$\frac{1}{4} \mathbf{a}(\mathbf{k}) \cdot \mathbf{a}(\mathbf{k}') = \Delta_{\mathbf{k}\mathbf{k}'}^+ \exp(i\theta_{\mathbf{k}\mathbf{k}'}^+), \quad (4.11b)$$

$$\frac{1}{4} \mathbf{a}(\mathbf{k}) \cdot \mathbf{a}^*(\mathbf{k}') = \Delta_{\mathbf{k}\mathbf{k}'}^- \exp(i\theta_{\mathbf{k}\mathbf{k}'}^-), \quad (4.11c)$$

$$-\mathbf{k} \cdot \mathbf{A}(\mathbf{k}', t) = \sigma_{\mathbf{k}\mathbf{k}'} \cos(u_{\mathbf{k}'} + \xi_{\mathbf{k}\mathbf{k}'}), \quad (4.11d)$$

² Note that in the second and third lines $\mathbf{a}(\mathbf{k}) \cdot \mathbf{a}(\mathbf{k}') = a_1(\mathbf{k})a_1(\mathbf{k}') + a_2(\mathbf{k})a_2(\mathbf{k}') + a_3(\mathbf{k})a_3(\mathbf{k}')$ and similar for $\mathbf{a}(\mathbf{k}) \cdot \mathbf{a}^*(\mathbf{k}')$, although $\mathbf{a}(\mathbf{k})$ is a complex vector.

$$\rho_{\mathbf{k}} = \frac{\lambda_{\mathbf{k}}}{\eta_{\mathbf{k}}}, \quad (4.11e)$$

$$\alpha_{\mathbf{k}\mathbf{k}'}^{\pm} = \frac{\Delta_{\mathbf{k}\mathbf{k}'}^{\pm}}{\eta_{\mathbf{k}} \pm \eta_{\mathbf{k}'}}. \quad (4.11f)$$

Our final solution for the nondipole Volkov states will be expressed in terms of the functions $\rho_{\mathbf{k}} = \rho(\mathbf{k})$, $\theta_{\mathbf{k}} = \theta(\mathbf{k})$, $\alpha_{\mathbf{k}\mathbf{k}'}^{\pm} = \alpha^{\pm}(\mathbf{k}, \mathbf{k}')$, $\theta_{\mathbf{k}\mathbf{k}'}^{\pm} = \theta^{\pm}(\mathbf{k}, \mathbf{k}')$, $\sigma_{\mathbf{k}\mathbf{k}'} = \sigma(\mathbf{k}, \mathbf{k}')$ and $\xi_{\mathbf{k}\mathbf{k}'} = \xi(\mathbf{k}, \mathbf{k}')$, which encode all details of the laser field via the above definitions.

We start our procedure to solve Eq. (4.9) with the approximation $f \approx f^{(0)}$ and neglect the gradient term $\mathbf{A}(\mathbf{r}, t) \cdot \nabla f^{(0)}$. If we make use of the integral form of the vector potential (4.1), we obtain the following equation for $f^{(0)}$:

$$\begin{aligned} i \int d^3\mathbf{k}' \eta_{\mathbf{k}'} \frac{\delta f^{(0)}[\mathbf{u}_{\mathbf{k}}]}{\delta \mathbf{u}_{\mathbf{k}'}} &= \left(\int d^3\mathbf{k} \lambda_{\mathbf{k}} \cos(\mathbf{u}_{\mathbf{k}} + \theta_{\mathbf{k}}) \right) f^{(0)}[\mathbf{u}_{\mathbf{k}}] \\ &+ \left[\int d^3\mathbf{k} \int d^3\mathbf{k}' (\Delta_{\mathbf{k}\mathbf{k}'}^+ \cos(\theta_{\mathbf{k}\mathbf{k}'}^+ + \mathbf{u}_{\mathbf{k}} + \mathbf{u}_{\mathbf{k}'}) \right. \\ &\quad \left. + \Delta_{\mathbf{k}\mathbf{k}'}^- \cos(\theta_{\mathbf{k}\mathbf{k}'}^- + \mathbf{u}_{\mathbf{k}} - \mathbf{u}_{\mathbf{k}'}) \right] f^{(0)}[\mathbf{u}_{\mathbf{k}}]. \end{aligned} \quad (4.12)$$

Although it appears rather complicated, this equation can be treated by guessing the solution,

$$f^{(0)}[\mathbf{u}_{\mathbf{k}}] = e^{-i\Gamma^{(0)}[\mathbf{u}_{\mathbf{k}}]}, \quad (4.13a)$$

$$\begin{aligned} \Gamma^{(0)}[\mathbf{u}_{\mathbf{k}}] &= \int d^3\mathbf{k} \rho_{\mathbf{k}} \sin(\mathbf{u}_{\mathbf{k}} + \theta_{\mathbf{k}}) \\ &+ \int d^3\mathbf{k} \int d^3\mathbf{k}' (\alpha_{\mathbf{k}\mathbf{k}'}^+ \sin(\theta_{\mathbf{k}\mathbf{k}'}^+ + \mathbf{u}_{\mathbf{k}} + \mathbf{u}_{\mathbf{k}'}) + \alpha_{\mathbf{k}\mathbf{k}'}^- \sin(\theta_{\mathbf{k}\mathbf{k}'}^- + \mathbf{u}_{\mathbf{k}} - \mathbf{u}_{\mathbf{k}'})), \end{aligned} \quad (4.13b)$$

and it can be proven by insertion (see App. C) that this expression indeed provides an exact solution to Eq. (4.12).

In the second step of our solution, we are now left with the unknown functional g in Eq. (4.10). An equation for g is obtained if the ansatz (4.10) is inserted into the full Schrödinger equation (4.9). In doing so, we make use of the solution (4.13) for $f^{(0)}$ and neglect all terms of *second* order in $f^{(0)}$ and g in the gradient term proportional to $\mathbf{A}(\mathbf{r}, t) \cdot \nabla f$. We will discuss the physical meaning of this omission in hindsight below. As a result, we obtain the following functional integro-differential equation for g :

$$i \int d^3\mathbf{k}' \eta_{\mathbf{k}'} \frac{\delta g[\mathbf{u}_{\mathbf{k}}]}{\delta \mathbf{u}_{\mathbf{k}'}} = \int d^3\mathbf{k}' \int d^3\mathbf{k}'' \sigma_{\mathbf{k}'\mathbf{k}''} \cos(\mathbf{u}_{\mathbf{k}''} + \xi_{\mathbf{k}'\mathbf{k}''}) \frac{\delta \Gamma^{(0)}[\mathbf{u}_{\mathbf{k}}]}{\delta \mathbf{u}_{\mathbf{k}'}}}, \quad (4.14)$$

with $\Gamma^{(0)}$ given by Eq. (4.13b).

Its solution can be written in the form

$$\begin{aligned}
g[\mathbf{u}_k] = & \frac{1}{2i} \int d^3\mathbf{k} \int d^3\mathbf{k}' \sigma_{\mathbf{k}\mathbf{k}'} \rho_{\mathbf{k}} \left(\frac{\sin(\mathbf{u}_{\mathbf{k}} + \mathbf{u}_{\mathbf{k}'} + \theta_{\mathbf{k}} + \xi_{\mathbf{k}\mathbf{k}'})}{\eta_{\mathbf{k}} + \eta_{\mathbf{k}'}} + \frac{\sin(\mathbf{u}_{\mathbf{k}} - \mathbf{u}_{\mathbf{k}'} + \theta_{\mathbf{k}} - \xi_{\mathbf{k}\mathbf{k}'})}{\eta_{\mathbf{k}} - \eta_{\mathbf{k}'}} \right) \\
& + \frac{1}{i} \int d^3\mathbf{k} \int d^3\mathbf{k}' \int d^3\mathbf{k}'' \sigma_{\mathbf{k}\mathbf{k}'} \alpha_{\mathbf{k}\mathbf{k}''}^+ \left(\frac{\sin(\mathbf{u}_{\mathbf{k}} + \mathbf{u}_{\mathbf{k}'} + \mathbf{u}_{\mathbf{k}''} + \theta_{\mathbf{k}\mathbf{k}''}^+ + \xi_{\mathbf{k}\mathbf{k}'})}{\eta_{\mathbf{k}} + \eta_{\mathbf{k}'} + \eta_{\mathbf{k}''}} \right. \\
& \quad \left. + \frac{\sin(\mathbf{u}_{\mathbf{k}} - \mathbf{u}_{\mathbf{k}'} + \mathbf{u}_{\mathbf{k}''} + \theta_{\mathbf{k}\mathbf{k}''}^+ - \xi_{\mathbf{k}\mathbf{k}'})}{\eta_{\mathbf{k}} - \eta_{\mathbf{k}'} + \eta_{\mathbf{k}''}} \right) \\
& + \frac{1}{i} \int d^3\mathbf{k} \int d^3\mathbf{k}' \int d^3\mathbf{k}'' \sigma_{\mathbf{k}\mathbf{k}'} \alpha_{\mathbf{k}\mathbf{k}''}^- \left(\frac{\sin(\mathbf{u}_{\mathbf{k}} + \mathbf{u}_{\mathbf{k}'} - \mathbf{u}_{\mathbf{k}''} + \theta_{\mathbf{k}\mathbf{k}''}^- + \xi_{\mathbf{k}\mathbf{k}'})}{\eta_{\mathbf{k}} + \eta_{\mathbf{k}'} - \eta_{\mathbf{k}''}} \right. \\
& \quad \left. + \frac{\sin(\mathbf{u}_{\mathbf{k}} - \mathbf{u}_{\mathbf{k}'} - \mathbf{u}_{\mathbf{k}''} + \theta_{\mathbf{k}\mathbf{k}''}^- - \xi_{\mathbf{k}\mathbf{k}'})}{\eta_{\mathbf{k}} - \eta_{\mathbf{k}'} - \eta_{\mathbf{k}''}} \right), \tag{4.15}
\end{aligned}$$

which can again be verified by insertion in steps very similar to those shown in App. C. Of course, the expression (4.15) is not particularly easy to evaluate for a given vector potential and more convenient and closed forms of the functional g and, as a result, the functional f are needed to evaluate the nondipole Volkov states (4.5) for a specific physical scenario.

Let us therefore examine the correction induced by the functional g to the functional f via Eq. (4.10). Upon a close inspection of Eq. (4.15) and the functions defined in Eqs. (4.11), we can write the function³ $g(\mathbf{r}, t)$ as

$$g(\mathbf{r}, t) = 4a\delta_1 g_1(\mathbf{r}, t) + a\delta_2 g_2(\mathbf{r}, t), \tag{4.16}$$

where g_1 and g_2 are of order unity and we have extracted the dimensionless factors

$$a = \frac{q^2 A_0^2}{4m_e c k_0}, \quad \delta_1 = \frac{p}{m_e c}, \quad \delta_2 = \frac{q A_0}{m_e c}, \tag{4.17}$$

which we have written in SI units with the electron's charge q , mass m_e , its characteristic momentum p , and a characteristic wave number k_0 and amplitude A_0 of the vector potential, respectively. Our treatment of the electron dynamics is based on the Schrödinger equation. This equation is non-relativistic and therefore, in order to be consistent, the wave function that we have derived in terms of Eqs. (4.5), (4.10), (4.13)

³ From here on, we will write all functionals of $\mathbf{u}_{\mathbf{k}} = \mathbf{u}_{\mathbf{k}}(\mathbf{r}, t)$ as functions of \mathbf{r} and t , e.g. $g(\mathbf{r}, t) = g[\mathbf{u}_{\mathbf{k}}(\mathbf{r}, t)]$.

and (4.15) is restricted to situations in which the characteristic electron velocity v is small compared to the speed of light,

$$1 \gg \frac{v}{c} = \frac{1}{cm_e} |\mathbf{p} - q\mathbf{A}|. \quad (4.18)$$

We are therefore left with the requirement $\delta_1, \delta_2 \ll 1$. According to Eq. (4.16), this means that the function g is only a *small* correction to the function f and therefore to the wave function. Returning to Eq. (4.17), we can ascribe a physical meaning to this statement: on the one hand, if $\delta_1 \ll 1$, the asymptotic momentum \mathbf{p} of the electron, measured at the detector, is small compared to $m_e c$. Thus, the *free* electron motion is non-relativistic. On the other hand, if $\delta_2 \ll 1$, the intensity of the laser field (in terms of the amplitude A_0) is non-relativistic. That is, the *induced* electron motion due to the laser field is non-relativistic. Moreover, both terms in Eq. (4.16) scale with the dimensionless parameter α . For a plane-wave laser field, we may also write $\alpha = 4cq^2\beta_0$ with the amplitude β_0 of the (classical) figure-eight motion that the electron performs in the laser field (cf. Sec. 3.2). Thus, the correction to the wave function of the electron that is given by the function $g(\mathbf{r}, t)$ scales with both the relativistic velocity of the electron in the field and the classical nondipole effects.

4.2.2 Modified Volkov phase

We have solved the Schrödinger equation (4.9) iteratively by first finding a *zeroth-order* approximation $f^{(0)}$ and then constructing a *first-order* correction g . In principle, we could continue this procedure and solve for a *second-order* correction h to the factor $1 + g$. In doing so, we would insert the functional $f = f^{(0)}(1 + g + h)$ into the Schrödinger equation (4.9) and keep all second-order terms in $f^{(0)}$ and g in the gradient term proportional to $\mathbf{A}(\mathbf{r}, t) \cdot \nabla f$. However, according to our estimates from the last paragraphs of the preceding section, these terms would be of order $\delta_1 g \sim (v/c)^2$ and $\delta_2 g \sim (v/c)^2$, respectively. In the non-relativistic treatment that we assumed by starting from the Schrödinger equation, these terms can therefore be neglected and the functional h would provide no further correction to the solution in terms of $f^{(0)}$ and g . Taking this discussion into account, we consider the wave function (4.5) with the functional f as constructed above as *exact* within the non-relativistic treatment of the Schrödinger equation. In a final step, we will now express the full nondipole Volkov state (4.5) in a form that resembles the dipole Volkov state discussed in Sec. 3.25.

In certain experimental situations, the relative magnitude $\delta_2/\delta_1 = qA_0/4p$ of the two terms in Eq. (4.16) is small compared to one. The second term can then

be neglected and we may write $g(\mathbf{r}, t) = 4a\delta_1 g_1(\mathbf{r}, t)$. This estimate is true for the laser-assisted scattering analyzed by Rosenberg and Zhou (1993) and results in the moderate intensity limit discussed therein. However, in strong-field atomic experiments like ATI or HHG, the ratio δ_2/δ_1 need not be small and may be of order unity. Nevertheless, as we have estimated above, the correction induced by g is small ($|g| \ll 1$) in all non-relativistic situations. We can therefore write $g = -i\delta\Gamma(\mathbf{r}, t)$ and

$$1 + g(\mathbf{r}, t) = 1 - i\delta\Gamma(\mathbf{r}, t) \approx e^{-i\delta\Gamma(\mathbf{r}, t)}. \quad (4.19)$$

The wave function (4.5) then takes the form

$$\chi_{\mathbf{p}}(\mathbf{r}, t) = \frac{1}{(2\pi)^{3/2}} e^{-i(E_{\mathbf{p}}t - \mathbf{p}\cdot\mathbf{r})} e^{-i\Gamma(\mathbf{r}, t)}, \quad (4.20a)$$

with the *modified* Volkov phase

$$\begin{aligned} \Gamma(\mathbf{r}, t) &= \Gamma_0(\mathbf{r}, t) + \delta\Gamma(\mathbf{r}, t) \\ &= \int d^3\mathbf{k} \rho_{\mathbf{k}} \sin(u_{\mathbf{k}} + \theta_{\mathbf{k}}) \\ &\quad + \int d^3\mathbf{k} \int d^3\mathbf{k}' (\alpha_{\mathbf{k}\mathbf{k}'}^+ \sin(u_{\mathbf{k}} + u_{\mathbf{k}'} + \theta_{\mathbf{k}\mathbf{k}'}^+) + \alpha_{\mathbf{k}\mathbf{k}'}^- \sin(u_{\mathbf{k}} - u_{\mathbf{k}'} + \theta_{\mathbf{k}\mathbf{k}'}^-)) \\ &\quad + \frac{1}{2} \int d^3\mathbf{k} \int d^3\mathbf{k}' \sigma_{\mathbf{k}\mathbf{k}'} \rho_{\mathbf{k}} \left(\frac{\sin(u_{\mathbf{k}} + u_{\mathbf{k}'} + \theta_{\mathbf{k}} + \xi_{\mathbf{k}\mathbf{k}'})}{\eta_{\mathbf{k}} + \eta_{\mathbf{k}'}} + \frac{\sin(u_{\mathbf{k}} - u_{\mathbf{k}'} + \theta_{\mathbf{k}} - \xi_{\mathbf{k}\mathbf{k}'})}{\eta_{\mathbf{k}} - \eta_{\mathbf{k}'}} \right) \\ &\quad + \mathcal{O}(a\delta_2). \end{aligned} \quad (4.20b)$$

Here, the $\mathcal{O}(a\delta_2)$ -term includes the triple integrals over \mathbf{k} , \mathbf{k}' and \mathbf{k}'' in Eq. (4.15). As long as $\delta_2/\delta_1 \ll 1$, this term can be neglected and in many situations, depending on the precise form of the vector potential, these integrals will vanish identically (cf. Sec. 5.3.1). Therefore, we did not include this term explicitly in the above formula for the modified Volkov phase $\Gamma(\mathbf{r}, t)$. When evaluating this formula for a given vector potential, however, one should keep in mind that this term may be non-negligible.

Equations (4.20) constitute the main result of this chapter. The wave functions $\chi_{\mathbf{p}}(\mathbf{r}, t)$ are nondipole Volkov states that describe the dynamics of a non-relativistic electron moving under the influence of the spatially dependent laser field defined by the vector potential (4.1). In order to find explicit expressions for the Volkov states for a given vector potential, one needs to evaluate the functions $\rho_{\mathbf{k}}$, $\theta_{\mathbf{k}}$, $\alpha_{\mathbf{k}\mathbf{k}'}^{\pm}$, $\theta_{\mathbf{k}\mathbf{k}'}^{\pm}$, $\sigma_{\mathbf{k}\mathbf{k}'}$ and $\xi_{\mathbf{k}\mathbf{k}'}$ according to Eqs. (4.11) and solve the integrals occurring in Eq. (4.20b). In general, this is not straightforward. However, in Chaps. 5 and 6 we will discuss two physical scenarios in which the nondipole SFA based on the nondipole Volkov states (4.20) allows the calculation of measurable quantities that cannot be obtained within

the dipole approximation. The special cases discussed in these chapters provide an important testing ground for our nondipole SFA in terms of the nondipole Volkov states (4.20) and the transition amplitude (4.2), since they can either be treated within other nondipole SFA formalisms or allow a comparison with experiments. Most importantly, the applications discussed in the following chapters can be readily extended to experimentally realistic beam shapes within our nondipole SFA.

4.2.3 Relation to other nondipole SFA theories

Before we turn to specific applications of the nondipole SFA, let us conclude this chapter with a comparison of the nondipole Volkov states (4.20) to other approaches known from the literature (cf. Sec. 4.1.2). We will also discuss the dipole limit of Eq. (4.20) for the special case of a plane-wave laser field at the end of Sec. 5.3.1 and show that it reduces to the dipole Volkov state (3.25).

Regarding the electron dynamics, our nondipole Volkov states account for the same first-order relativistic corrections as the quasi-relativistic approximation of Krajewska and Kaminski (2015). Furthermore, although we did not construct a mathematically exact solution to the Schrödinger equation, we argued above that it can be considered exact in terms of the non-relativistic treatment. Therefore, one should expect to obtain results in agreement with He et al. (2017) for a plane-wave laser field. Indeed, we will see in Sec. 5.3.1 that our nondipole Volkov states agree with those of Krajewska and Kaminski (2015) and He et al. (2017) in this case.

Moreover, since we followed the derivation of Rosenberg and Zhou (1993), their result for a discrete superposition of the form (4.4) is included in our solution: if the integral in Eq. (4.1) is reduced to a discrete superposition via a sum of delta functions $\delta(\mathbf{k} - \mathbf{k}_j)$, Eqs. (4.13) and (4.15) yield their equations (A6) and (A8), respectively.

Most notably, in contrast to all other nondipole SFA theories that have been developed previously, the nondipole SFA derived here for continuous superpositions of plane waves (4.1) allows the incorporation of an *arbitrary* spatial dependence of the laser field into the electron continuum.

PEAK SHIFTS IN THE ATI WITH PLANE-WAVE BEAMS

In this chapter, we will apply the nondipole SFA developed in the previous chapter to a specific physical problem: the ATI driven by a plane-wave laser beam including nondipole interactions in the continuum. A specific quantity that can be measured in experiments is the so-called *peak shift* towards nonzero p_z in the PEMD, which we will introduce in Sec. 5.1. In this chapter, we will focus on its calculation and the comparison with experimental values. After discussing the experimental setup in more detail in Sec. 5.2, we will turn to the calculation of the PEMD within the nondipole SFA in Sec. 5.3 and will analyze the results following from it in Sec. 5.4.

Parts of the material presented in this chapter were published previously in the following reference:

Nondipole strong-field approximation for spatially structured laser fields

B. Böning, W. Paufler, and S. Fritzsche

PHYSICAL REVIEW A **99**, 053404 (2019)

5.1 NONDIPOLE EFFECTS IN PLANE-WAVE LASER FIELDS

The nondipole Volkov states derived in Chap. 4 allow the analysis of the quantum dynamics of an electron in a spatially dependent laser field of a very general form. Within the dipole approximation, the spatial dependence of the laser field is omitted and, therefore, the interaction between the magnetic field and the electron cannot be described. Equivalently, in the particle picture, one can say that the photon momentum is neglected and, thus, cannot be transferred to the electron (or the ion). The SFA in the dipole approximation successfully explains many features of ATI- (and HHG-) spectra and PEMD that have been measured over the past decades with plane-wave driving laser fields in the near-IR (see Sec. 3.4).

In recent years, however, new developments in the generation and control of long-wavelength laser sources have enabled the realization of both ATI and HHG experiments in the mid-IR range (Popmintchev et al., 2012; Dura et al., 2013; Wolter

et al., 2015). The use of mid-IR driving fields has several advantages both for the theoretical understanding of strong-field experiments and their utilization for table-top laser sources. First, the Keldysh parameter (3.1) scales with the laser wavelength as $\gamma \sim \lambda^{-1}$, so that the use of mid-IR instead of near-IR driving beams provides access to small Keldysh parameters $\gamma < 1$. The picture that the photoelectron tunnels out of a quasi-static barrier in the first step of the three-step model described in Sec. 3.1 is, strictly speaking, only applicable for small Keldysh parameters. Therefore, mid-IR driving laser fields allow one to probe the dynamics of strong-field processes deeper in this tunneling regime and to test this picture that is often employed also for near-IR driving fields (Colosimo et al., 2008). As a second advantage of mid-IR driving fields, the spectra of photons emitted in HHG exhibit a cut-off at $I_p + 3.2U_p$, where $U_p \sim \lambda^2$ is the ponderomotive energy introduced in Eq. (3.2). Thus, the cut-off scales with the square of the laser wavelength and this allows the generation of harmonic photons in the x-ray regime and the generation of ultrashort and stable laser pulses of attosecond or even sub-attosecond duration when the process is driven by mid-IR laser beams (Colosimo et al., 2008; Popmintchev et al., 2012; Hernández-García et al., 2013).

However, such experiments are performed close to or beyond the long-wavelength limit of the dipole approximation (cf. Fig. 3.2 in Sec. 3.2): the photoelectron in the continuum is influenced by the magnetic part of the Lorentz force so that it performs a figure-eight motion of considerable amplitude along the laser propagation direction. For HHG experiments in the mid-IR this presents a serious limitation as it suppresses the recombination of the photoelectron with the parent ion (Pisanty et al., 2018).

For strong-field *ionization* experiments, on the other hand, the magnetic Lorentz force has a measurable consequence, which we will analyze in the following based on the formalism developed in the previous chapter: when the wavelength of the driving field lies in the mid-IR, the momentum distributions of photoelectrons are shifted towards nonzero p_z , i.e. along the laser propagation direction (Smeenck et al., 2011; Ludwig et al., 2014; Wolter et al., 2015; Maurer et al., 2018). This shift is now commonly called the *peak shift* Δp_z of the PEMD. In a pioneering work, Smeenck et al. (2011) measured the PEMD in the $p_x - p_z$ -plane using velocity map imaging for circularly polarized driving laser fields at 800 nm and 1400 nm and for varying intensities. The authors found that the peak shift is in the order of $\Delta p_z = 5 \times 10^{-3}$ a.u. to $\Delta p_z = 20 \times 10^{-3}$ a.u. and that it increases linearly with the laser intensity. These values correspond to a transfer of few photon momenta ($\hbar k \approx 2 \times 10^{-4}$ a.u. at $\lambda = 1400$ nm) to the photoelectron during the ionization process. As one would expect from the scaling of the classical nondipole effects ($\beta_0 \sim I\lambda^3$, cf. Sec. 3.2), the peak shift also increases with the wavelength (Ludwig et al., 2014). However, its

accurate and reliable measurement still presents a significant technical challenge (Wolter et al., 2015; Hartung et al., 2019).

Surprisingly, Ludwig et al. (2014) found that the peak shift may be *negative* if the driving laser field is linearly polarized. This finding has been called the *counterintuitive peak shift* in subsequent works. Since the photon momentum points along the positive z -axis, one would expect that the peak shift is also always positive. This is indeed true for the direct electrons that do not recollide with the parent ion after emission from the atom. However, for linear polarization, the electrons may be driven back to the ion and rescatter at the Coulomb potential before reaching the detector (cf. Fig. 3.1). Numerical solutions of the Schrödinger equation have shown that the combination of the Lorentz force and the Coulomb potential leads to the negative peak shifts measured in experiments (Chelkowski et al., 2015). Later, this interpretation was confirmed based on semi-classical Coulomb-corrected quantum trajectories including nondipole interactions (Keil and Bauer, 2017; Daněk et al., 2018b). A detailed analysis of the high-energy plateau resulting from rescattered photoelectrons in terms of numerical solutions of the Schrödinger equation has shown that the peak shift for linearly polarized driving fields depends on the photoelectron energy and that a precise understanding of the underlying mechanism must be based on a better knowledge about the rescattering process (Brennecke and Lein, 2018). Other theoretical works have reproduced the peak shifts for circularly polarized driving laser fields based on nondipole versions of the SFA (Titi and Drake, 2012; He et al., 2017). While the respective results agree qualitatively with experiments, small discrepancies remain between the actually predicted and measured values, respectively, which can be attributed to the nonuniform intensity of the (Gaussian) laser pulse used in experiments (Smeenk et al., 2011; Titi and Drake, 2012).

Here, we will discuss the peak shifts within the nondipole SFA, based on the nondipole Volkov states derived in the previous chapter. We will demonstrate how the nondipole Volkov states can be explicitly evaluated for a plane-wave laser field and how the peak shifts can then be computed. We will, however, restrict our analysis to direct photoelectrons, described by the direct SFA amplitude (4.2), and neglect any rescattering with the parent ion. Although we will present results also for linear polarization, the above discussion must be kept in mind when comparing them with experiments. In contrast to other nondipole SFA theories, our approach has the advantage that a realistic beam shape may be assumed instead of the simple plane-wave ansatz. In the future, this will allow to include corrections to the photoelectron dynamics induced by a Gaussian beam shape, i.e. the focal averaging mentioned above, and therefore to compute peak shifts in quantitative agreement

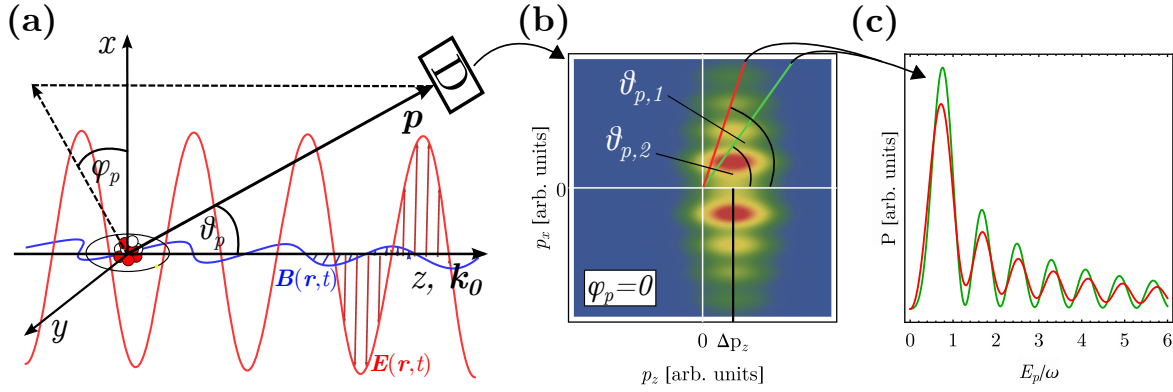


Figure 5.1: ATI with a plane-wave laser beam. (a) Geometry: the laser beam propagates along the positive z -direction ($\mathbf{k}_0 = k_0 \mathbf{e}_z$) and is polarized in the $x - y$ -plane. Shown are the electric (red) and magnetic (blue) fields for linear polarization. The photoelectron emitted from the target atom is measured at the detector D with momentum $\mathbf{p} = (p, \vartheta_p, \varphi_p)$. (b) The detector records the PEMD in the $p_x - p_z$ -plane ($\varphi_p = 0$). Due to nondipole interactions, the maxima in the PEMD are shifted towards nonzero $p_z = \Delta p_z$ (peak shift). (c) ATI spectra $P(E_p) = \mathbb{P}(\sqrt{2E_p}, \vartheta_p, \varphi_p = 0)$ as measured for two different polar angles $\vartheta_{p,1}$ (red) and $\vartheta_{p,2}$ (green). The position $(E_{p,\max}, \vartheta_{p,\max})$ of the overall maximum of spectra measured under a sufficient number of polar angles ϑ_p defines the peak shift $\Delta p_z = \sqrt{2E_{p,\max}} \sin \vartheta_{p,\max}$. Figures (b) and (c) are schematic representations.

with experiments. We will discuss this extension and its usefulness for the calculation of nondipole effects at the end of the chapter.

5.2 SETUP AND PARAMETERS

Figure 5.1 shows the setup considered in this chapter: an intense, continuous, monochromatic and elliptically polarized plane-wave laser beam that propagates along the z -axis ionizes an atomic target. As illustrated in Fig. 5.1, the atom is positioned at the origin. As in Sec. 3.4, we will consider it to be in a hydrogen-like $1s$ initial state, given by Eq. (3.29), with an ionization potential I_p adapted to the atomic target in question. In contrast to the setup considered in Sec. 3.4, here we include both the electric and magnetic fields of the beam in our description. Upon ionization of the atom, a photoelectron is emitted from the target and detected with momentum $\mathbf{p} = (p, \vartheta_p, \varphi_p)$ in spherical coordinates and $\mathbf{p} = (p_x, p_y, p_z)$ in Cartesian coordinates, respectively. Below, it will be convenient to use both coordinate systems in order to have a compact notation. At the detector, the PEMD $\mathbb{P}(\mathbf{p})$ is measured. The peak shift Δp_z is visible in the $p_x - p_z$ -plane of the PEMD as the shift of the maximal ionization probability $\mathbb{P}_{\max}(p_x, 0, p_z)$ from $p_z = 0$ as expected in the dipole approximation to $p_z = \Delta p_z \neq 0$ due to nondipole interactions.

In accordance with Sec. 2.3, the vector potential of the laser beam is given by

$$\mathbf{A}(\mathbf{r}, t) = \frac{A_0}{\sqrt{1 + \varepsilon^2}} (\cos(\mathbf{k}_0 \cdot \mathbf{r} - \omega_0 t) \mathbf{e}_x - \varepsilon \Lambda \sin(\mathbf{k}_0 \cdot \mathbf{r} - \omega_0 t) \mathbf{e}_y), \quad (5.1)$$

where the wave number $\mathbf{k}_0 = k_0 \mathbf{e}_z = \omega_0 / c \mathbf{e}_z$ with the laser frequency $\omega_0 = 2\pi c / \lambda$ and the wavelength λ . We define the ellipticity as $0 \leq \varepsilon \leq 1$ and use $\Lambda = \pm 1$ to denote the helicity of the beam. The intensity I of the beam is given by Eq. (2.13) in terms of the amplitude A_0 .

5.3 PHOTOIONIZATION PROBABILITY

The photoionization probability $\mathbb{P}(\mathbf{p})$ is written in terms of the SFA transition amplitude via [cf. Eq. (3.4)]

$$\mathbb{P}(\mathbf{p}) = p |\mathbb{T}(\mathbf{p})|^2 \approx p |\mathbb{T}_0(\mathbf{p})|^2, \quad (5.2)$$

where we approximate the full transition amplitude $\mathbb{T}(\mathbf{p})$ by the direct amplitude $\mathbb{T}_0(\mathbf{p})$, given by Eq. (4.2). Our aim in this section is to evaluate the direct transition amplitude with the continuum described by the nondipole Volkov states derived in the previous chapter.

5.3.1 Nondipole Volkov states

According to Eq. (4.20), the nondipole Volkov states have the form

$$\chi_{\mathbf{p}}(\mathbf{r}, t) = \frac{1}{(2\pi)^{3/2}} e^{-i(E_{\mathbf{p}}t - \mathbf{p} \cdot \mathbf{r})} e^{-i\Gamma(\mathbf{r}, t)}. \quad (5.3)$$

In order to evaluate the modified Volkov phase $\Gamma(\mathbf{r}, t)$, given in general by Eq. (4.20b), we rewrite the vector potential (5.1) in the form (4.1):

$$\mathbf{A}(\mathbf{r}, t) = \frac{A_0}{\sqrt{1 + \varepsilon^2}} \text{Re} \left\{ (\mathbf{e}_x + i\Lambda\varepsilon\mathbf{e}_y) e^{i(\mathbf{k}_0 \cdot \mathbf{r} - \omega_0 t)} \right\} = \int d^3\mathbf{k} \mathbf{A}(\mathbf{k}, t), \quad (5.4a)$$

with $\mathbf{A}(\mathbf{k}, t) = \text{Re} \{ \mathbf{a}(\mathbf{k}) e^{i\mathbf{u}_{\mathbf{k}}} \}$, $\mathbf{u}_{\mathbf{k}} = \mathbf{k} \cdot \mathbf{r} - \omega_{\mathbf{k}} t$, $\omega_{\mathbf{k}} = kc$ and the Fourier coefficients

$$\mathbf{a}(\mathbf{k}) = \frac{A_0}{\sqrt{1 + \varepsilon^2}} (\mathbf{e}_x + i\Lambda\varepsilon\mathbf{e}_y) \delta(\mathbf{k} - \mathbf{k}_0). \quad (5.4b)$$

With this expression for the vector potential, we are in a position to evaluate the functions defined in Eqs. (4.11).

The results are (see App. D.1 for the derivation):

$$\rho_{\mathbf{k}} = \frac{A_0}{\sqrt{1+\varepsilon^2}} \frac{\sqrt{p_x^2 + \varepsilon^2 p_y^2}}{\mathbf{p} \cdot \mathbf{k} - \omega_{\mathbf{k}}} \delta(\mathbf{k} - \mathbf{k}_0), \quad (5.5a)$$

$$\theta_{\mathbf{k}} = \varphi_p^{(\varepsilon)} := \Lambda \arctan(\varepsilon \tan \varphi_p), \quad (5.5b)$$

$$\alpha_{\mathbf{k}\mathbf{k}'}^{\pm} = \frac{A_0^2}{4} \frac{1 \mp \varepsilon^2}{1 + \varepsilon^2} \frac{1}{\mathbf{p} \cdot (\mathbf{k} \pm \mathbf{k}') - (\omega_{\mathbf{k}} \pm \omega_{\mathbf{k}'})} \delta(\mathbf{k} - \mathbf{k}_0) \delta(\mathbf{k}' - \mathbf{k}_0), \quad (5.5c)$$

$$\theta_{\mathbf{k}\mathbf{k}'}^{\pm} = 0, \quad (5.5d)$$

$$\sigma_{\mathbf{k}\mathbf{k}'} = -\frac{A_0}{\sqrt{1+\varepsilon^2}} \sqrt{k_x^2 + \varepsilon^2 k_y^2} \delta(\mathbf{k}' - \mathbf{k}_0), \quad (5.5e)$$

$$\xi_{\mathbf{k}\mathbf{k}'} = 0. \quad (5.5f)$$

Upon insertion of these expressions, the modified Volkov phase (4.20b) reduces to

$$\begin{aligned} \Gamma(\mathbf{r}, t) &= A_0 \frac{\sqrt{p_x^2 + \varepsilon^2 p_y^2}}{\sqrt{1+\varepsilon^2}} \int d^3\mathbf{k} \frac{\sin(u_{\mathbf{k}} + \varphi_p^{(\varepsilon)})}{\eta_{\mathbf{k}}} \delta(\mathbf{k} - \mathbf{k}_0) \\ &+ \frac{A_0^2}{4} \frac{1 - \varepsilon^2}{1 + \varepsilon^2} \int d^3\mathbf{k} \int d^3\mathbf{k}' \frac{\sin(u_{\mathbf{k}} + u_{\mathbf{k}'})}{\eta_{\mathbf{k}} + \eta_{\mathbf{k}'}} \delta(\mathbf{k} - \mathbf{k}_0) \delta(\mathbf{k}' - \mathbf{k}_0) \\ &+ \frac{A_0^2}{4} \int d^3\mathbf{k} \int d^3\mathbf{k}' \frac{\sin(u_{\mathbf{k}} - u_{\mathbf{k}'})}{\eta_{\mathbf{k}} - \eta_{\mathbf{k}'}} \delta(\mathbf{k} - \mathbf{k}_0) \delta(\mathbf{k}' - \mathbf{k}_0) \\ &+ \frac{1}{2} \int d^3\mathbf{k} \int d^3\mathbf{k}' \sigma_{\mathbf{k}\mathbf{k}'} \rho_{\mathbf{k}} \frac{\sin(u_{\mathbf{k}} + u_{\mathbf{k}'} + \varphi_p^{(\varepsilon)})}{\eta_{\mathbf{k}} + \eta_{\mathbf{k}'}} \\ &+ \frac{1}{2} \int d^3\mathbf{k} \int d^3\mathbf{k}' \sigma_{\mathbf{k}\mathbf{k}'} \rho_{\mathbf{k}} \frac{\sin(u_{\mathbf{k}} - u_{\mathbf{k}'} + \varphi_p^{(\varepsilon)})}{\eta_{\mathbf{k}} - \eta_{\mathbf{k}'}} \end{aligned} \quad (5.6)$$

where $\eta_{\mathbf{k}} = \mathbf{p} \cdot \mathbf{k} - \omega_{\mathbf{k}}$. Note that we have omitted the $\mathcal{O}(\alpha\delta_2)$ -term that appears in Eq. (4.20b) and consists of the triple integrals over \mathbf{k} occurring in Eq. (4.15). For the plane-wave laser beam considered in this chapter, this term vanishes identically. We can see this if we insert $\alpha_{\mathbf{k}\mathbf{k}'}^{\pm}$ and $\sigma_{\mathbf{k}\mathbf{k}'}$ from Eqs. (5.5) into this term, carry out the \mathbf{k} integration and note that the result is proportional to $\sigma_{\mathbf{k}_0\mathbf{k}'} \sim \sqrt{k_{0,x}^2 + \varepsilon^2 k_{0,y}^2} = 0$. With the same argument, we can see that the last two lines in Eq. (5.6) vanish.

The \mathbf{k} -integral in the first line as well as the first integral in the second line of Eq. (5.6) can be easily evaluated by making use of the delta-functions. We then find

$$\begin{aligned} \Gamma(\mathbf{r}, t) &= \frac{A_0}{\eta_{\mathbf{k}_0}} \frac{\sqrt{p_x^2 + \varepsilon^2 p_y^2}}{\sqrt{1 + \varepsilon^2}} \sin(\mathbf{u}_{\mathbf{k}_0} + \varphi_p^{(\varepsilon)}) + \frac{A_0^2}{4} \frac{1 - \varepsilon^2}{1 + \varepsilon^2} \frac{\sin(2\mathbf{u}_{\mathbf{k}_0})}{2\eta_{\mathbf{k}_0}} \\ &\quad + \frac{A_0^2}{4} \int d^3\mathbf{k} \frac{\sin(\mathbf{u}_{\mathbf{k}} - \mathbf{u}_{\mathbf{k}_0})}{\eta_{\mathbf{k}} - \eta_{\mathbf{k}_0}} \delta(\mathbf{k} - \mathbf{k}_0). \end{aligned} \quad (5.7)$$

The remaining integral requires some care due to the apparent divergence at $\mathbf{k} = \mathbf{k}_0$:

$$\begin{aligned} \int d^3\mathbf{k} \frac{\sin(\mathbf{u}_{\mathbf{k}} - \mathbf{u}_{\mathbf{k}_0})}{\eta_{\mathbf{k}} - \eta_{\mathbf{k}_0}} \delta(\mathbf{k} - \mathbf{k}_0) &= \int dk_z \frac{\sin((z - ct)(k_z - k_0))}{(p_z - c)(k_z - k_0)} \delta(k_z - k_0) \\ &= \frac{1}{p_z - c} \int dk_z \left(z - ct + \mathcal{O}((k_z - k_0)^2) \right) \delta(k_z - k_0) \\ &= \frac{z - ct}{p_z - c} \\ &= \frac{\mathbf{u}_{\mathbf{k}_0}}{\eta_{\mathbf{k}_0}}. \end{aligned} \quad (5.8)$$

The final expression for the modified Volkov phase in an elliptically polarized plane-wave laser field is now given by

$$\Gamma(\mathbf{r}, t) = \rho_\varepsilon \sin(\mathbf{u}_{\mathbf{k}_0} + \varphi_p^{(\varepsilon)}) + \alpha \frac{1 - \varepsilon^2}{1 + \varepsilon^2} \sin(2\mathbf{u}_{\mathbf{k}_0}) + 2\alpha \mathbf{u}_{\mathbf{k}_0}, \quad (5.9a)$$

$$\rho_\varepsilon = \frac{A_0}{\eta_{\mathbf{k}_0}} \frac{\sqrt{p_x^2 + \varepsilon^2 p_y^2}}{\sqrt{1 + \varepsilon^2}}, \quad (5.9b)$$

$$\alpha = \frac{A_0^2}{8\eta_{\mathbf{k}_0}}. \quad (5.9c)$$

The nondipole Volkov states (5.3) can be expanded into plane waves in a similar way as the dipole Volkov states in Sec. 3.4. To do so, we again make use of the Jacobi-Anger expansion (see App. A):

$$\begin{aligned} \chi_{\mathbf{p}}(\mathbf{r}, t) &= \frac{1}{(2\pi)^{3/2}} e^{-i(E_{\mathbf{p}}t - \mathbf{p} \cdot \mathbf{r})} e^{-i\Gamma(\mathbf{r}, t)} \\ &= \frac{1}{(2\pi)^{3/2}} e^{-i(E_{\mathbf{p}}t - \mathbf{p} \cdot \mathbf{r} + 2\alpha \mathbf{u}_{\mathbf{k}_0})} e^{-i\rho_\varepsilon \sin(\mathbf{u}_{\mathbf{k}_0} + \varphi_p^{(\varepsilon)})} e^{-i\alpha \frac{1 - \varepsilon^2}{1 + \varepsilon^2} \sin(2\mathbf{u}_{\mathbf{k}_0})} \\ &= \frac{1}{(2\pi)^{3/2}} \sum_{n, m = -\infty}^{\infty} J_n(\rho_\varepsilon) J_m \left(\alpha \frac{1 - \varepsilon^2}{1 + \varepsilon^2} \right) e^{-in\varphi_p^{(\varepsilon)}} \\ &\quad \times e^{i\mathbf{p}_{nm} \cdot \mathbf{r}} e^{-i(E_{\mathbf{p}} + \tilde{U}_{\mathbf{p}} - (n+2m)\omega_0)t}, \end{aligned} \quad (5.10)$$

where we have defined the momentum $\mathbf{p}_{nm} = \mathbf{p} + (\tilde{U}_p/\omega_0 - (n + 2m))k_0\mathbf{e}_z$ and $\tilde{U}_p = \frac{U_p}{1-p_z/c}$ with the ponderomotive energy $U_p = A_0^2/4$.

It is instructive to compare the nondipole Volkov states (5.10) with the modified Volkov phase (5.9) to the corresponding dipole Volkov states. The dipole Volkov phase (3.25) is derived in App. B for an elliptically polarized plane-wave beam and is given by

$$S_V(t) = E_p t + U_p t + \frac{A_0}{\omega_0} \frac{\sqrt{p_x^2 + \varepsilon^2 p_y^2}}{\sqrt{1 + \varepsilon^2}} \sin(\omega_0 t - \varphi_p^{(\varepsilon)}) + \frac{A_0^2}{8\omega_0} \frac{1 - \varepsilon^2}{1 + \varepsilon^2} \sin(2\omega_0 t). \quad (5.11)$$

In fact, in the limit $k_0 \rightarrow 0$, Eqs. (5.9) reduce to this formula since $\eta_{k_0} \rightarrow -\omega_0$, and $u_{k_0} \rightarrow -\omega_0 t$ in this limit. In other words, the nondipole Volkov states reduce to the dipole Volkov states if the photon momentum is neglected. In hindsight, we can therefore write the modified Volkov phase for a single-mode plane-wave laser field in a convenient form that resembles the dipole Volkov phase:

$$\Gamma(\mathbf{r}, t) = E_p t + \frac{1}{2(\mathbf{p} \cdot \mathbf{k}_0 - \omega_0)} \int^{u_{k_0}} d\phi \left(\mathbf{A}(\phi) \cdot \mathbf{p} + \frac{1}{2} \mathbf{A}^2(\phi) \right), \quad (5.12)$$

where, for the moment, we used the common notation $\phi = \mathbf{k} \cdot \mathbf{r} - \omega t$ and $\mathbf{A}(\phi) = A_0/\sqrt{1 + \varepsilon^2}(\cos \phi \mathbf{e}_x + \varepsilon \Lambda \sin \phi \mathbf{e}_y)$. The expression (5.12) agrees with both the exact (nondipole) solution of the Schrödinger equation for this case (He et al., 2017, below Eq. (2) therein with $G(\eta) \rightarrow 1$) and the first-order non-relativistic ($1/c$) truncation of the Dirac-Volkov states (Krajewska and Kaminski, 2015, Eq. (47) therein). The equality to the latter confirms that our derivation from the Schrödinger equation up to first order in v/c in Chap. 4 is indeed consistent. Furthermore, the connection to the relativistic theory allows an important conclusion: the denominator $\mathbf{p} \cdot \mathbf{k}_0 - \omega_0$ (instead of $-\omega_0$ in the dipole Volkov states¹) has the effect of giving the photoelectron an effective momentum-dependent mass $m_{\text{eff}} = m_e - p_z/c$ (Krajewska and Kaminski, 2015). This *recoil correction* is indeed the main origin for the peak shift in the PEMD that we will discuss below.

5.3.2 SFA transition amplitude

With the nondipole Volkov states in their final form (5.10), we are in a position to write down the direct SFA transition amplitude for the ATI of the atomic target as described in Sec. 5.2 and to compute the photoionization probability. For the continuous laser beam considered here, the first term in the transition amplitude (4.2)

¹ Note that this appears in Eq. (3.25) by replacing the integration variable t by $-\omega t$.

vanishes and upon insertion of the nondipole Volkov states (5.10) and the initial state (3.29), we obtain

$$\begin{aligned}
\mathbb{T}_0(\mathbf{p}) &= -i \int_{-\infty}^{\infty} d\tau \langle \chi_{\mathbf{p}}(\tau) | V(\mathbf{r}) | \Psi_0(\tau) \rangle \\
&= -i \sum_{n,m=-\infty}^{\infty} J_n(\rho_\varepsilon) J_m \left(\alpha \frac{1-\varepsilon^2}{1+\varepsilon^2} \right) e^{in\vartheta_p^{(\varepsilon)}} \langle \mathbf{p}_{nm} | V(\mathbf{r}) | \Phi_0 \rangle \\
&\quad \times \int_{-\infty}^{\infty} d\tau e^{i(E_p + \tilde{U}_p + I_p - (n+2m)\omega_0)\tau} \\
&= -2\pi i \sum_{n,m=-\infty}^{\infty} J_n(\rho_\varepsilon) J_m \left(\alpha \frac{1-\varepsilon^2}{1+\varepsilon^2} \right) V_{nm}(\mathbf{p}) e^{in\vartheta_p^{(\varepsilon)}} \\
&\quad \times \delta(E_p + \tilde{U}_p + I_p - (n+2m)\omega_0). \tag{5.13}
\end{aligned}$$

In the last equality, we have defined the matrix element of the Coulomb potential

$$V_{nm}(\mathbf{p}) = \langle \mathbf{p}_{nm} | V(\mathbf{r}) | \Phi_0 \rangle = \frac{1}{(2\pi)^{3/2}} \int d^3\mathbf{r} \frac{e^{-\sqrt{2I_p}r}}{r} e^{-i\mathbf{p}_{nm}\cdot\mathbf{r}} = -\frac{2^{3/4}I_p^{5/4}}{\pi} \frac{1}{\frac{p_{nm}^2}{2} + I_p}. \tag{5.14}$$

The final form of the transition amplitude (5.13) can be interpreted in the following way. Given the polar angle ϑ_p under which the photoelectrons are detected, the argument of the delta function defines the positions E_p of the ATI peaks in the energy spectrum via the implicit equation

$$E_p + \frac{U_p}{1 - \frac{\sqrt{2E_p} \cos \vartheta_p}{c}} + I_p - (n+2m)\omega_0 = 0, \tag{5.15}$$

where we have used that $p_z = p \cos \vartheta_p = \sqrt{2E_p} \cos \vartheta_p$. For given integers n and m , that is, for a given number of photons absorbed by the photoelectron, this equation defines an ATI peak. The amplitude of this ATI peak is given by the prefactors of the corresponding delta function in Eq. (5.13).

From our discussion following Eq. (5.12), we expect to recover the direct SFA transition amplitude in dipole approximation in the limit $k_0 \rightarrow 0$ (and $c \rightarrow \infty$). This is indeed the case, since $\mathbf{p}_{nm} \rightarrow \mathbf{p}$ and $\tilde{U}_p \rightarrow U_p$ in this limit and therefore Eq. (5.13) reduces to Eq. (3.36) if $\varepsilon = 1$.

5.3.3 Computation of ATI spectra and peak shifts

From the transition amplitude (5.13), the photoionization probability follows according to Eq. (5.2). However, the transition amplitude involves two infinite sums, which, although they give a descriptive physical meaning to the ionization process in terms of absorbed photons, are difficult to evaluate exactly. In order to compute ATI spectra based on Eqs. (5.2) and (5.13), we therefore proceed in the following steps:

1. Fix the polar and azimuthal angles ϑ_p and φ_p , respectively (detector position).
2. Solve Eq. (5.15) for the energy values $E_p^{(N)}$ of the ATI peaks, where $N = n + 2m$. Thereby, n and m are subsequently increased until a predefined energy range $0 \leq E_p \leq E_{\max}$ has been covered. The upper limit of this range is given by the cut-offs of the Bessel functions in the transition amplitude (5.13), $J_l(x) \sim e^{-l}$ for $l > x$. Accordingly, in our calculations below, we will set $n_{\max} = \lceil |\rho_\varepsilon| \rceil$ and $m_{\max} = \lceil |\alpha| \frac{1-\varepsilon^2}{1+\varepsilon^2} \rceil$, where $\lceil x \rceil$ denotes the smallest integer larger than x .
3. For every energy value $E_p^{(N)}$ found in the previous step, i.e. every ATI peak, compute the photoionization probability according to Eq. (5.2) with the respective prefactor of the delta function in Eq. (5.13),

$$\mathbb{P}_N = (2\pi)^2 \sqrt{2E_p^{(N)}} \left| \sum_{n+2m=N} J_n(\rho_\varepsilon) J_m \left(\alpha \frac{1-\varepsilon^2}{1+\varepsilon^2} \right) V_{nm} \left(\sqrt{2E_p^{(N)}} \mathbf{e}_p \right) e^{in\varphi_p^{(\varepsilon)}} \right|^2, \quad (5.16)$$

where \mathbf{e}_p is the unit vector defined by ϑ_p and φ_p . Note that we have to sum coherently over all values of n and m which yield the same energy value.

In the following, we will always set $\varphi_p = 0$, that is, we will only analyze photoelectrons emitted with $p_y = 0$ in the $p_x - p_z$ -plane. For a linearly polarized beam ($\varepsilon = 0$, $\mathbf{A}(\mathbf{r}, t) \sim \mathbf{e}_x$), one can expect that no photoelectrons are emitted along the p_y -direction, as in the dipole approximation (cf. Sec. 3.4). For a circularly polarized beam, the ionization probabilities measured along the p_x - and p_y -directions are expected to be equal due to the symmetry of the beam and the initial state wave function. Since our main focus lies in the analysis of the peak shifts Δp_z , the choice $\varphi_p = 0$ is therefore reasonable.

In order to extract the peak shift, we numerically compute the ATI spectra for discrete values of the polar angle in the range $\vartheta_p \in [0, \pi]$ according to steps 1–3 above. The peak shifts are then given by $\Delta p_z = \sqrt{2E_{p,\max}} \cos \vartheta_{p,\max}$ where $E_{p,\max}$ and $\vartheta_{p,\max}$ are the energy and polar angle, respectively, under which the maximum ionization probability \mathbb{P}_N is found (cf. Fig. 5.1).

5.4 RESULTS

In the previous section, we have derived explicit expressions for the ATI transition amplitude (5.13) and photoionization probability (5.16) within the nondipole SFA. In general, the resulting ATI spectra and peak shifts will depend on the laser intensity I , the wavelength λ , the ellipticity ε and the ionization potential I_p of the atomic target. In the following, we will analyze them for specific laser parameters and atomic targets and focus, in particular, on the dependence of the peak shifts on λ and I as well as the atomic target. As we have discussed in Sec. 5.1, the longitudinal motion β_0 of the photoelectron in the laser field increases with both λ and I . Therefore, the influence of nondipole interactions in the ATI can be controlled by these two parameters. The particular parameter ranges that have been used to measure peak shifts in experiments are in the mid-IR range at intensities up to 10^{14} W/cm² (Ludwig et al., 2014; Daněk et al., 2018a; Maurer et al., 2018), but also near-IR wavelengths have been used at intensities up to 10^{15} W/cm² (Smeenk et al., 2011). In order to compare with the experimental findings of these works, we choose intensities in the range $I = 10^{13}$ W/cm² to $I = 10^{15}$ W/cm² and vary the wavelength in the range from $\lambda = 800$ nm to $\lambda = 3400$ nm. Furthermore, we consider the noble gases He ($I_p = 24.6$ eV), Ne ($I_p = 21.6$ eV) and Ar ($I_p = 15.8$ eV) as atomic targets.

5.4.1 Circular polarization

We begin with circularly polarized beams: for $\varepsilon = 1$, the transition amplitude (5.13) can be written as

$$\mathbb{T}_0(\mathbf{p}) = -2\pi i \sum_{n=-\infty}^{\infty} J_n(\rho_C) V_n(\mathbf{p}) e^{in\Lambda\varphi_p} \delta(E_p + \tilde{U}_p + I_p - n\omega_0), \quad (5.17)$$

with $V_n(\mathbf{p}) = -\frac{2^{3/4} I_p^{5/4}}{\pi} \frac{1}{p_n^2/2 + I_p}$, $\mathbf{p}_n = \mathbf{p} + (\tilde{U}_p/\omega_0 - n)\mathbf{k}_0 \mathbf{e}_z$ and where we introduced $\rho_C = \frac{\Lambda_0 p \sin\vartheta_p}{\sqrt{2}\eta k_0}$. We can see from Eq. (5.17) that the transition amplitude depends on the helicity Λ only through a phase factor. Thus, the ionization probability of each ATI peak does not depend on Λ and our results will be identical for both right ($\Lambda = 1$) and left ($\Lambda = -1$) circularly polarized beams. This is plausible, since for a 1s initial state and a continuous laser beam, the system is symmetric in the polarization plane. Note, however, that a helicity dependence may arise for pulses of finite duration due to interferences between different terms in the summation in the transition amplitude, similar to the generalization from continuous beams to short pulses the dipole approximation (cf. Sec.3.4).

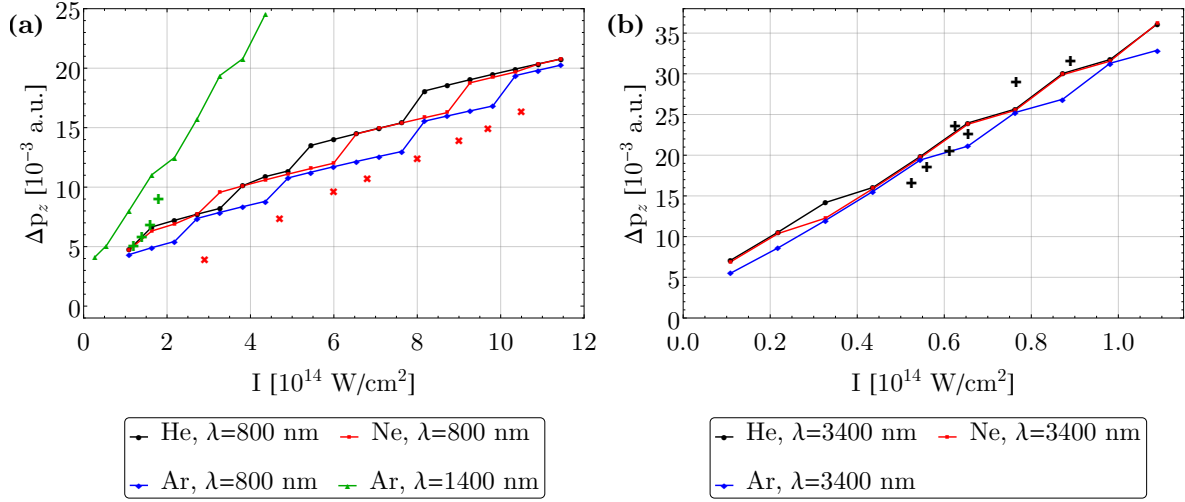


Figure 5.2: Peak shifts Δp_z of maxima in ATI spectra as a function of laser intensity I for a circularly polarized laser beam, computed within the nondipole SFA. Results are shown for different atomic targets and laser wavelengths λ . The parameters were chosen in order to be comparable to the following experimental works: (a) Smeenck et al., 2011 (Ne and Ar at 800 nm and Ar at 1400 nm); (b) Daněk et al., 2018a (He at 3400 nm). For Ar at 1400 nm [green +’s in (a)], Ne at 800 nm [red x’s in (a)] and He at 3400 nm [black +’s in (b)], the experimental values extracted from these references are included in the figures.

Experimental results for the peak shifts Δp_z have been discussed by Smeenck et al. (2011) for Ne and Ar gas targets at $\lambda = 800$ nm and at $\lambda = 1400$ nm. Together with their experimental values, Fig. 5.2 (a) shows the peak shifts computed via the procedure outlined in Sec. 5.3.3 within the nondipole SFA. The figure displays Δp_z as a function of the laser intensity I for He and Ne at $\lambda = 800$ nm as well as Ar at both $\lambda = 800$ nm and 1400 nm. Although Fig. 3.2 indicates that the dipole approximation is still applicable at these wavelengths and intensities, we find significant peak shifts. It is clear that the line ($\beta_0 = 1$) separating *dipole* and *nondipole* regimes in Fig. 3.2 is not a strict border but presents a smooth transition from one to the other. Close to this line, however, the detection of nondipole effects in strong-field ionization experiments is challenging: according to Smeenck et al. (2011), their measurements were sensitive to about five photon momenta (2×10^{-3} a.u. at $\lambda = 800$ nm). The results shown in Fig. 5.2 (a) for $\lambda = 800$ nm and at low intensities are therefore close to the limits of the experiment. For the longer wavelength of $\lambda = 1400$ nm the peak shifts are larger, as we would expect from the scaling of nondipole effects with $\beta_0 \sim I\lambda^3$.

We can further observe from the figure that the peak shift depends only slightly on the chosen atomic target. This can be expected within the SFA formalism since the atomic target is characterized only by the ionization potential I_p and the initial state wave function is modeled as a hydrogen-like 1s state (3.29), which disregards any details of the real atomic structure. This independence on the atomic target agrees

with the experimental data shown in Fig. 2 of Smeenk et al. (2011). Their results indicate, however, that the intensity dependence of Δp_z has a slightly larger slope for Ne than for Ar at $\lambda = 800$ nm. Since this discrepancy is only present at low intensities, it might be due to measurement errors.

One pronounced difference between our theory and experiments can be directly observed in Fig. 5.2 (a): independent of intensity and wavelength, the nondipole SFA predicts values for Δp_z that are systematically larger than the experimental ones by a factor of 1.5 to 2. This difference may be due to several effects. To begin with, the nondipole SFA that we use here takes the laser field into account only in the photoelectron continuum. That is, we account for the radiation pressure on the electron arising from the non-vanishing photon momentum but neglect any momentum transfer to the parent ion. Let us decompose the ionization process into a tunneling and a propagation step in the picture of the three-step model (cf. Sec. 3.1). During the tunneling step, momentum is transferred from the laser field to the combined system of electron and ion. It has been shown based on a relativistic tunneling theory that a total forward momentum of I_p/c is transferred in this step of which the electron acquires $I_p/(3c)$ while the remaining momentum is transferred to the ion (Yakaboylu et al., 2013; Klaiber et al., 2013b). While it is important to consider the ion in the tunneling step, we do not account for the momentum transfer I_p/c in the transition amplitude (5.17) at all. We would therefore expect our theoretical curves to *underestimate* the experimental values by $I_p/(3c) \approx 10^{-3}$ a.u. (for Ar).

However, we also neglect several contributions in the propagation step, where momentum from the laser beam is transferred only to the photoelectron. The discrepancy between our theoretical values and experiments must be rooted in an incomplete description of the continuum dynamics in terms of the nondipole Volkov states (5.10). Indeed, the model of a continuous plane-wave driving laser beam provides only a rough approximation to experiments. First, finite pulses are usually used whose intensity is not constant in time, leading to changes in the ionization dynamics. Second, the *spatial* dependence of the intensity in a real laser pulse imposes a Lorentz force acting on the photoelectron that is due to the gradient of the spatial envelope. To see this, let us assume a Gaussian laser pulse for which the vector potential (5.1) is multiplied by an envelope

$$g(r, z, t) = e^{-\left(\frac{r}{w_0}\right)^2} e^{-\frac{2 \ln 2}{c^2 \tau^2} (z-ct)^2}, \quad (5.18)$$

with the radial distance r from the beam axis, the beam waist w_0 and the pulse duration τ . The z -dependence of the envelope g leads to a correction $\Delta F_{L,z}$ of the

(time-averaged) Lorentz force acting on the photoelectron along the laser propagation direction (Smeenck et al., 2011; Smorenburg et al., 2011),

$$\Delta F_{L,z} = -\frac{\partial U_p}{\partial z}, \quad (5.19)$$

where $U_p = A^2(r, z)/4$ is the r - and z -dependent ponderomotive potential resulting from the pulse envelope. That is, this Lorentz force due to the Gaussian pulse envelope counteracts the radiation pressure on the photoelectron and leads to a shift of its longitudinal momentum towards smaller values. This negative shift is in the order of the discrepancy that we see between theoretical and the experimental results in Fig. 5.2 (Smeenck et al., 2011). In addition, the radial dependence of the envelope leads to a reduced average intensity and may also alter the peak shift. Accordingly, our results for Δp_z obtained on the assumption of a continuous plane-wave laser beam overestimate the experimental findings. In future work, our nondipole SFA approach to the peak shift Δp_z may be extended by starting with a Gaussian laser pulse, i.e. with the vector potential (5.1) multiplied by the pulse envelope (5.18). The approach developed in Chap. 4 allows one to include the full spatial (and temporal) dependence of the Gaussian pulse into the description of the photoelectron dynamics in terms of the nondipole Volkov states (4.20).

Let us now turn to the results presented in Fig. 5.2 (b). Here, peak shifts are shown for $\lambda = 3400$ nm in the mid-IR and for the same atomic targets as in Fig. 5.2 (a). We see that, although the intensities are lower by an order of magnitude than those in Fig. 5.2 (a), the peak shifts are comparable. This illustrates the strong dependence of nondipole interactions on the wavelength. Also, as above, the peak shift does not change significantly if the atomic target is changed. We can compare our results with the experimental data published by Daněk et al. (2018a) for a He target, which we also included in Fig. 5.2 (b). In contrast to the shorter wavelengths discussed above, our results seem to agree well with the experimental values. However, the theoretical analysis published by Maurer et al. (2018) indicates that a different definition of the laser intensity ($I = A_0^2 \omega^2 / 2$ instead of our $I = A_0^2 \omega^2 c / 8\pi$) was used by Daněk et al. (2018a). If this is accounted for, our theoretical values are again systematically larger by a factor of 1.5, which, as before, can be attributed to the neglect of the spatial dependence of a realistic laser pulse in our computations.

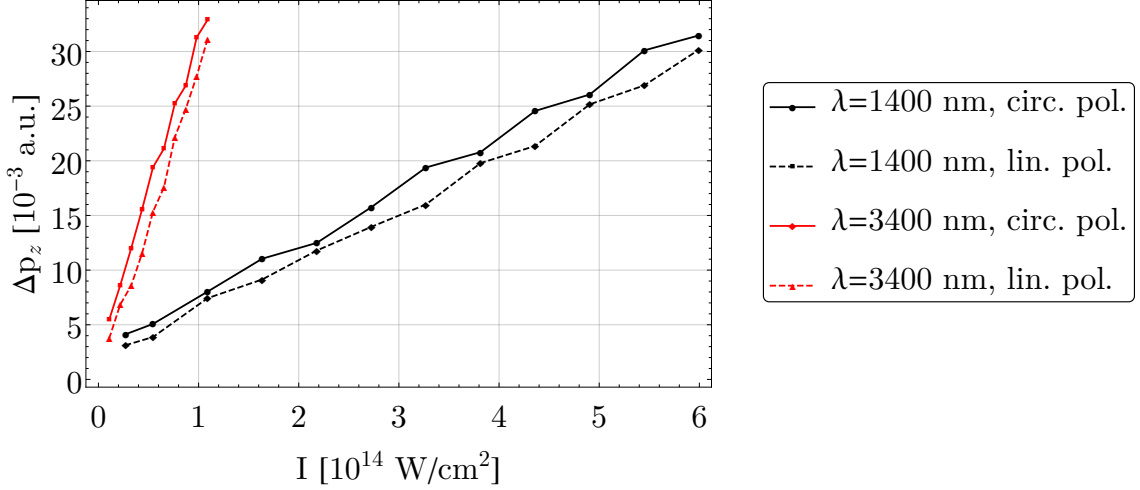


Figure 5.3: Peak shifts Δp_z of maxima in ATI spectra for an Ar target as a function of laser intensity I , computed within the nondipole SFA. Results are shown for circularly (solid curves) and linearly (dashed curves) polarized laser beams and for two wavelengths λ . The solid curves are identical to the corresponding ones in Fig. 5.2 (a) for 1400 nm and Fig. 5.2 (b) for 3400 nm, respectively.

5.4.2 Linear polarization

Experiments have found an interesting dependence of the peak shift on the polarization of the laser beam and we will now discuss it for linear polarization ($\varepsilon = 0$). In this case, the transition amplitude (5.13) reduces to

$$\mathbb{T}_0(\mathbf{p}) = -2\pi i \sum_{n,m=-\infty}^{\infty} J_n(\rho_L) J_m(\alpha) V_{nm}(\mathbf{p}) \delta(E_p + \tilde{U}_p(p_z) + I_p - (n+2m)\omega_0), \quad (5.20)$$

where $V_{nm}(\mathbf{p}) = -\frac{2^{3/4} I_p^{5/4}}{\pi} \frac{1}{p_{nm}^2/2 + I_p}$, $\mathbf{p}_{nm} = \mathbf{p} + (\tilde{U}_p/\omega_0 - (n+2m)) k_0 \mathbf{e}_z$ and $\rho_L = \frac{\Lambda_0 p_x}{\eta k_0}$. This expression is more complicated than the corresponding Eq. (5.17) for circular polarization, since different combinations of the integers n and m may lead to the same energy value $E_p^{(N)}$ with $N = n + 2m$ in the ATI spectrum. In the transition amplitude, several terms need to be summed over in order to compute the corresponding ionization probability [cf. Eq. (5.16)]. Each term corresponds to the absorption of $n + 2m$ photons from the beam, leading to a change of the photoelectron's longitudinal momentum of $(n + 2m)k_0$. In contrast, for a circularly polarized beam, the amplitude for the absorption of $2m$ photons vanishes.

On the experimental side, peak shifts for linearly polarized driving beams were discussed in detail by Ludwig et al. (2014) for He, Ne, Ar and Xe gas targets at a wavelength of $\lambda = 3400$ nm. Here, we limit our discussion to Ar targets, since, as

in Sec. 5.4.1 above, we see almost no dependence of the peak shift on the atomic target. The peak shifts computed for 1400 nm and 3400 nm are shown in Fig. 5.3 together with the corresponding results for circular polarization that were already included in Fig. 5.2 (b). Although smaller in magnitude, the peak shifts for linear polarization differ only slightly from the values for circular polarization. This is in disagreement with the experimental data from Ludwig et al. (2014), where Δp_z was found to be *negative* for linear polarization at all intensities. As we have already discussed in Sec. 5.1, this peak shift *opposite* to the beam propagation direction is due to the interaction of the photoelectron with the Coulomb potential of the parent ion: the photoelectron rescatters with the parent ion during which its p_z -momentum component is essentially reversed. This interpretation is experimentally supported by the fact that if the rescattering is suppressed by increasing the ellipticity of the driving laser pulse, the peak shift changes sign (Maurer et al., 2018). Furthermore, if rescattering is accounted for in a theoretical treatment, the peak shifts have the correct sign (Daněk et al., 2018b). Since we did not include the rescattering amplitude (3.16c) in the present computations, the results for linear polarization differ from the experimental findings and we will not discuss them in more detail at this point. However, in the future, one may additionally include the rescattering amplitude within the nondipole SFA. Indeed, with the continuum described by the nondipole Volkov states (5.10), the evaluation of $\mathbb{T}_1(\mathbf{p})$ might be nontrivial and its physical meaning needs to be clarified (Klaiber et al., 2005). Also, to properly account for the Coulomb potential of the parent ion, an expression for *nondipole Coulomb-Volkov states* might be required. Nevertheless, the computation of peak shifts based on the full SFA transition amplitude $\mathbb{T}(\mathbf{p}) = \mathbb{T}_0(\mathbf{p}) + \mathbb{T}_1(\mathbf{p})$ using the nondipole Volkov states (5.10) should yield values closer to the experimental ones and help to understand the underlying physical mechanism.

Although we have neglected rescattering terms, let us briefly discuss the differences for linear and circular polarization. As can be observed from Fig. 5.3, the peak shift computed within the nondipole SFA is smaller for linear than for circular polarization for both wavelengths shown and over the full intensity range. To understand the origin of this difference within our formalism, it is useful to look at the general ellipticity dependence of the differential ionization probability (5.16) of an ATI peak characterized by the integer $N = n + 2m$. To emphasize the ε -dependence, we write Eq. (5.16) in the form

$$\mathbb{P}_N = (2\pi)^2 \sqrt{2E_p^{(N)}} \left| \sum_{n+2m=N} J_n \left(\rho_C \sqrt{\frac{2}{1+\varepsilon^2}} \right) J_m \left(\alpha \frac{1-\varepsilon^2}{1+\varepsilon^2} \right) V_{nm} \left(\sqrt{2E_p^{(N)}} \mathbf{e}_p \right) \right|^2, \quad (5.21)$$

where we set $\varphi_p = 0$ and where ρ_C denotes the argument of the Bessel function J_n for circular polarization. The position $p_z = \Delta p_z$ of the maximum of \mathbb{P}_N for a given ε is the peak offset for this ellipticity. For $\lambda = 1400$ nm and I between 10^{14} and 10^{15} W/cm², we find that Δp_z increases by about 0.004 a.u. if ε is continuously changed from 0 (linear) to 1 (circular). This is in line with the offset between the curves shown in Fig. 5.3. Within the direct SFA used here, this increase of the peak shift is a manifestation of the ellipticity dependence of the electron motion in the continuum: the drift velocity of a classical electron in z -direction increases with ellipticity (Jameson and Khvedelidze, 2008), which leads to a larger p_z -component measured at the detector. Daněk et al. (2018a) have performed an analysis based on classical-trajectory monte carlo simulations and found that this ellipticity-dependent drift velocity of the photoelectron yields a qualitative agreement with the experimental ε -dependence of the peak shift. It will be a promising future task to incorporate rescattering contributions in the nondipole SFA to reproduce and extend these findings.

5.5 CONCLUSIONS

In this chapter, we have demonstrated how the nondipole SFA developed in Chap. 4 can be applied to the ATI of atoms driven by plane-wave laser beams. To this end, we have evaluated the nondipole Volkov states (4.20) explicitly for an elliptically polarized beam. We then used the nondipole SFA to compute peak shifts Δp_z in the ATI spectra in laser propagation direction, which are a direct measurable consequence of nondipole interactions between laser beam and photoelectron.

We showed that the results for circular polarization are in good qualitative agreement with existing experimental data and that remaining discrepancies can be explained with our simplified assumption of a *plane-wave* driving beam. For linear polarization, the theoretical peak shifts have the wrong sign, which can be attributed to our neglect of the rescattering amplitude and Coulomb interactions in the continuum.

The theoretical description used in this chapter may be extended in several ways to obtain more quantitatively reliable results. First, the nondipole Volkov states for spatially structured laser fields derived in the previous chapter can be evaluated for a laser pulse with a Gaussian envelope (5.18). In doing so, the Lorentz force (5.19) due to the envelope is directly included in the quantum description of the photoelectron dynamics instead of correcting for it in hindsight as previous studies have done (Smeenk et al., 2011; Titi and Drake, 2012). Second, the rescattering amplitude (3.16c) may be included for linearly and elliptically polarized laser beams. However, both extensions go beyond the work of this dissertation and will be implemented in a future study.

Furthermore, other theoretical questions remain regarding the nature of nondipole interactions in the ionization process, e.g. the precise mechanism of momentum transfer from laser beam to photoelectron and residual ion. Since in the SFA we work in coordinates relative to the (fixed) parent ion and describe only the dynamics of the photoelectron, this partition of photon momentum is not accessible. Future theoretical and experimental work will give insight in this direction and help extend applications of strong-field atomic (and molecular) physics towards long wavelengths.

The work presented in this chapter shows that the nondipole SFA yields reliable results for the ATI with plane-wave laser beams. Other theoretical approaches to this experimental scenario exist and, especially, other nondipole SFA formalisms allow the calculation of peak shifts. In the next chapter, we will turn to a more complicated driving laser field, where the quite general approach developed in Chap. 4 is advantageous.

HIGH-INTENSITY KAPITZA-DIRAC EFFECT

In this chapter, we will apply the nondipole SFA developed in Chap. 4 to the ATI driven by a standing light wave, also known as *high-intensity KDE*. As we will discuss in Sec. 6.1, free electrons are deflected by a standing light wave under certain conditions, an effect discovered by Kapitza and Dirac (1933). If, instead, a gas of neutral atoms is placed within the standing wave, ATI driven by the standing wave itself yields photoelectrons, which are subsequently accelerated in the fields of the standing wave. Thereby, they gain very high longitudinal momenta p_z that are measured at the detector. While we saw in the previous chapter that only a few photon momenta $\hbar\mathbf{k}$ are transferred to the photoelectron in the ATI driven by plane wave beams, this *momentum transfer* can be in the order of $500\hbar\mathbf{k}$ for a standing light wave. We discuss the specific setup considered here in Sec. 6.2, before we show in Sec. 6.3 how it can be described within the nondipole SFA. In Sec. 6.4, we then examine the characteristic polar-angle distribution (PAD) of the photoelectrons. In particular, we propose experimental conditions under which *low-energy photoelectrons* can be generated with remarkably high longitudinal momenta that exhibit a strong dependence on the ellipticity of the standing wave and were not observed previously.

Parts of the material presented in this chapter are contained in the following reference:

Polarization-dependent high-intensity Kapitza-Dirac effect in strong laser fields

B. Böning, W. Paufler, and S. Fritzsche

PHYSICAL REVIEW A (Rapid Communications)

Accepted for publication (2020)

6.1 ELECTRON DEFLECTION BY A STANDING LIGHT WAVE

In their original work, Kapitza and Dirac (1933) proposed that free electrons entering a standing light wave should be deflected from their path by a small angle, provided the light intensity is high enough. This deflection, illustrated in Fig. 6.1 (a), is nowadays called (free-electron) KDE. In 1933, no sufficiently intense and coherent light sources

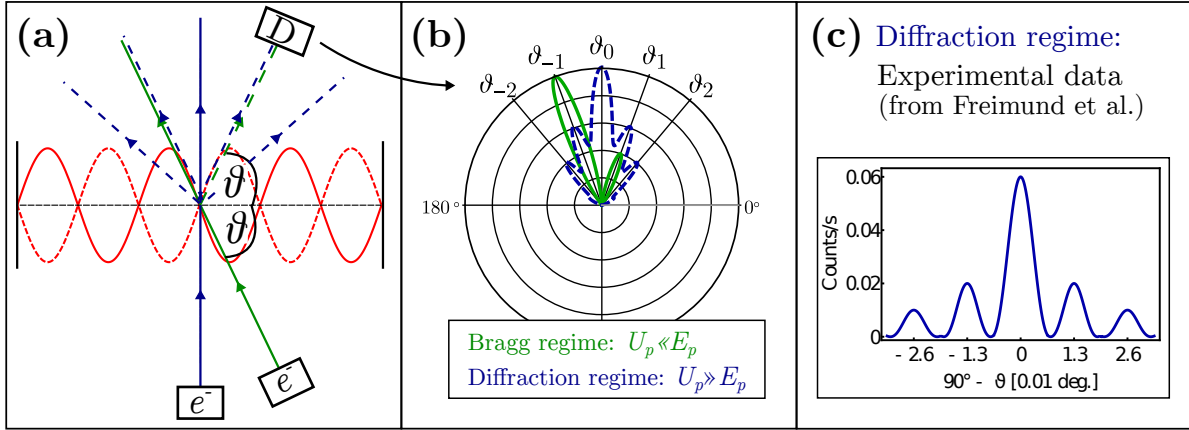


Figure 6.1: Free-electron KDE. (a) Electrons with well-defined kinetic energy $E_p = p^2/2$ are deflected by a standing light wave (red) and measured at the detector D under an angle ϑ . They enter the standing light wave either under the angle ϑ (Bragg regime for $U_p \ll E_p$) or perpendicularly (Diffraction regime for $U_p \gg E_p$). (b) In the Bragg regime deflection follows Bragg's law (green lines), while a diffraction pattern is formed in the diffraction regime (blue dashed lines; angles exaggerated). (c) Experimental data from Freimund et al. (2001) in the diffraction regime.

existed to observe the KDE and only decades later was the effect unambiguously detected (Freimund et al., 2001). Since the original publication, many variants of the KDE have been proposed and observed: in traveling waves (Smirnova et al., 2004), for neutral atoms (Martin et al., 1988) and even for molecules (Nairz et al., 2001). As a result, the KDE has attracted much interest owing to its potential to advance matter optics without the need for material gratings (Batelaan, 2007; Eichmann et al., 2009).

The electron deflection by a standing light wave can be understood from different perspectives. The classical viewpoint is instructive: a standing light wave is formed by two counter-propagating plane-wave beams of the form (2.12) with equal intensity, wavelength and ellipticity. A short calculation shows that the resulting electric and magnetic fields impose a non-vanishing time-averaged Lorentz force on an electron that has the form (Batelaan, 2007)

$$\mathbf{F}_p(z) = \nabla V_p(z), \quad V_p(z) = U_p \cos^2(kz), \quad (6.1)$$

where $U_p = A_0^2/4 = I\lambda^2/(2\pi c^3)$ is the ponderomotive energy of a single laser mode and $V_p(z)$ is the ponderomotive potential. The *ponderomotive force* \mathbf{F}_p points along the beam axis and has a spatial periodicity of $\lambda/2$. For an electron that impinges on the grating formed by the minima and maxima of F_p with momentum p and a de Broglie wavelength $\lambda_e = h/p$, Bragg's law $n\lambda_e/\lambda = 2 \sin \vartheta$ defines the angles ϑ_n ($n = 1, 2, \dots$) under which deflection occurs [green lines in Fig. 6.1 (a)]. This Bragg scattering was originally proposed by Kapitza and Dirac (1933).

The quantum perspective gives further insight: based on the Schrödinger equation for an electron in the ponderomotive potential $V_p(z)$, it can be shown that Bragg scattering occurs only for high-energy photoelectrons with $E_p \gg U_p$ (Batelaan, 2007). In contrast, for low-energy photoelectrons ($E_p \ll U_p$) that enter perpendicularly to the beam axis, a diffraction pattern is formed behind the standing wave [blue lines in Fig. 6.1 (a)]. Physically, for $E_p \gg U_p$ the electron can move over the crests of the ponderomotive potential, while, for $E_p \ll U_p$, the electron motion is bounded by the potential and different plane-wave contributions to its wave function can interfere (Batelaan, 2007). This distinction of two scattering *regimes* has also been verified by experiments (Freimund et al., 2001; Freimund and Batelaan, 2002).

Another perspective on the diffraction regime of the free-electron KDE is offered by the particle picture: the electron may absorb photons from the two counter-propagating laser modes forming the standing wave. In particular, it may absorb a photon from one mode and subsequently reemit a photon into the other mode, a process known as *virtual Compton scattering* (Rosenberg, 1994). Since both modes have the same wavelength and, thus, energy, the electron energy remains unchanged in this process. However, its momentum is changed by $2\hbar\mathbf{k}$. Multiple virtual Compton scattering events then lead to the peaks observed in the diffraction pattern.

In both the Bragg and diffraction regimes of the free-electron KDE, the momentum transfer to the photoelectron is in the order of one photon momentum $\hbar\mathbf{k}$, which leads to a very small angular separation of the maxima at the detector [cf. Fig. 6.1 (b) and (c)]. Thus, the observation and technical application of the free-electron KDE provides a significant challenge.

A (much) larger momentum transfer than in the free-electron KDE can be observed in the *high-intensity KDE*, which was first observed by Bucksbaum et al. (1988) and is illustrated in Fig. 6.2. Here, instead of a free-electron source, a cloud of neutral atoms is placed within the standing light wave. Due to the strong field of the standing wave, photoelectrons are generated by ATI of the atoms. Initially, these photoelectrons are emitted narrowly around the polarization plane of the standing wave and with distinct energies spaced by $\hbar\omega$. Similar to the free-electron KDE, they are then scattered in the continuum at the ponderomotive force field before they reach the detector with momentum $\mathbf{p} = (p, \vartheta_p, \varphi_p)$. There, they are measured with longitudinal momenta up to the order $p_z = p \cos \vartheta_p = 1000\hbar\mathbf{k}$. For fixed polar and azimuthal angles ϑ_p and φ_p , respectively, the detector measures an ATI spectrum of the photoelectrons emitted in these directions [cf. Fig. 6.2 (b)]. For photoelectrons with a fixed energy, i.e. within a particular ATI channel, the PAD exhibits distinct maxima away from the polarization plane due to the large longitudinal momentum [cf. Fig. 6.2 (c)]. Bucksbaum et al. (1988) showed that these maxima can be understood

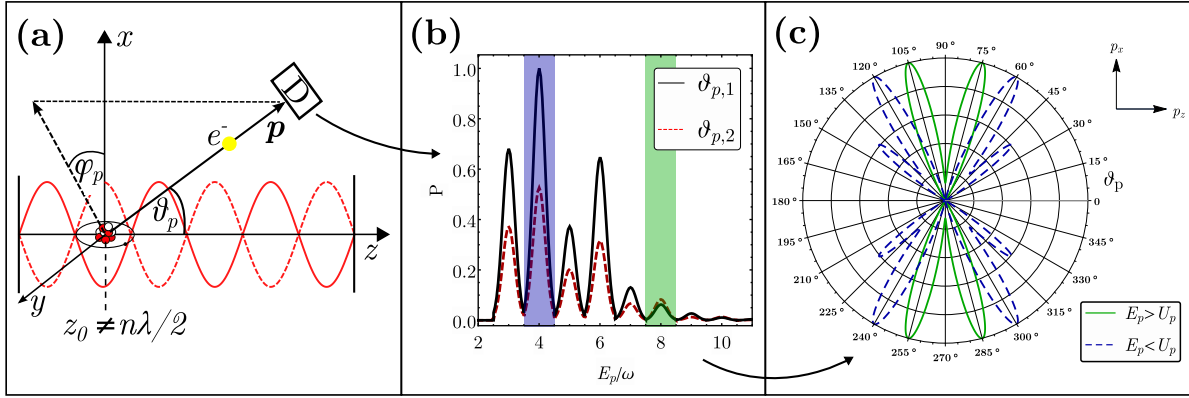


Figure 6.2: High-intensity KDE. (a) A neutral atom is placed in an intense standing light wave at $z = z_0$. Photoelectrons are emitted due to ATI driven by the standing wave itself and are measured at the detector D with momentum $\mathbf{p} = (p, \vartheta_p, \varphi_p)$. (b) Typical ATI spectra $P(E_p) = \mathbb{P}(\sqrt{2E_p}, \vartheta_p, \varphi_p = 0)$ for two values of the polar angle ϑ_p (black solid and red dashed curves) and for fixed azimuthal angle $\varphi_p = 0$. The electron count for a given ATI peak as a function of ϑ_p yields the PAD $P(\vartheta_p) = \mathbb{P}(\sqrt{2E_{p,0}}, \vartheta_p, \varphi_p = 0)$. (c) Typical PADs of high- (green solid curves) and low-energy (blue dashed curves) photoelectrons. The maxima in the PADs correspond to much larger longitudinal momenta Δp_z than in Fig. 6.1. The blue dashed curve illustrates a main finding of this chapter (see Sec. 6.4): low-energy photoelectrons exhibit a second set of maxima in their PADs, corresponding to a much larger momentum transfer Δp_z than the first set of maxima.

in terms of classical-trajectory monte carlo simulations based on the ponderomotive force (6.1) and, therefore, correspond to the Bragg scattering regime.

A more sophisticated quantum-mechanical treatment of the high-intensity KDE should account for the standing laser field in the continuum states available to the photoelectron. The large longitudinal momentum transfer in the high-intensity KDE resembles the strong nondipole interactions between photoelectron and standing wave. Thus, the nondipole SFA of Chap. 4 that can take into account superpositions of plane-wave laser modes in the continuum is suited as such a treatment. Other SFA-based approaches to the high-intensity KDE have been investigated: in the work of Guo and Drake (1992), also the laser field is quantized and transitions from the resulting QED-Volkov states to free-electron states are included. On this basis, the momentum transfer in the high-intensity KDE with circularly polarized standing waves as well as the free-electron KDE can be reproduced (Li et al., 2004; Yu et al., 2015). In a second approach (Rosenberg, 1994), the laser field was treated classically and the nondipole Volkov states by Rosenberg and Zhou (1993) were used, which exhibit phase singularities due to the virtual Compton scattering described above. When properly treated, they result in the large momentum transfer in the high-intensity KDE for linear polarization.

Most previous studies on the high-intensity KDE have focused on high-energy photoelectrons ($E_p > U_p$), similar to the Bragg regime in the free-electron KDE. Moreover, while the free-electron KDE was investigated also for elliptically polarized standing waves (Erhard and Bauke, 2015; Dellweg and Müller, 2017), only linear and circular polarizations were considered in the high-intensity KDE. Nowadays, standing light waves with elliptical polarization (Fang et al., 2016) and high intensities (Faure et al., 2006) can be generated. In principle, these allow the observation of low-energy photoelectrons with $E_p < U_p$ in the high-intensity KDE with different polarizations.

Here, we discuss the momentum transfer in the high-intensity KDE with elliptically polarized standing light waves. We make use of the nondipole SFA developed in Chap. 4, which leads to similar expressions as in Rosenberg (1994) that are, however, applicable to more general laser polarizations. As before, we will restrict ourselves to the direct SFA transition amplitude (4.2) and will show that the experimental results of Bucksbaum et al. (1988) can then be reproduced. We will demonstrate in Sec. 6.4 that low-energy photoelectrons exhibit markedly different PADs when compared to the high-energy photoelectrons considered in previous studies. This behavior depends on the ratio of the photoelectron energy E_p and the ponderomotive energy U_p of the standing wave and is quite analogous to the two regimes in the free-electron KDE. Finally, we will discuss that the momentum transfer to low-energy photoelectrons can be significantly enhanced [blue dashed curve in Fig. 6.2 (c)] and can be manipulated via the polarization of the standing wave.

6.2 SETUP AND PARAMETERS

In this chapter, we consider the setup shown in Fig. 6.2 (a): an atomic target is ionized by a strong standing light wave of intensity I and wavelength λ . We assume the z -axis as beam axis and allow for an elliptical polarization ε of the standing wave. We model the target as a single atom that is placed on the beam axis at some position $z = z_0 \neq n\lambda/2$, that is, away from the nodes of the standing wave¹. As before, we consider a hydrogen-like $1s$ initial state (3.29) with modified ionization potential I_p and where we account for the target position via a shift $\mathbf{r} \rightarrow \mathbf{r} - z_0\mathbf{e}_z$ in the coordinates. Upon ionization, photoelectrons are measured at the detector with momentum $\mathbf{p} = (p, \vartheta_p, \varphi_p)$ in spherical coordinates and $\mathbf{p} = (p_x, p_y, p_z)$ in Cartesian coordinates, respectively.

We describe the standing light wave by its vector potential $\mathbf{A}_\Lambda(\mathbf{r}, t)$ in Coulomb gauge. Here, we assume a very general vector potential, formed by two counter-

¹ See Sec. 6.3.4 for a discussion of the influence of the target position on the ionization process.

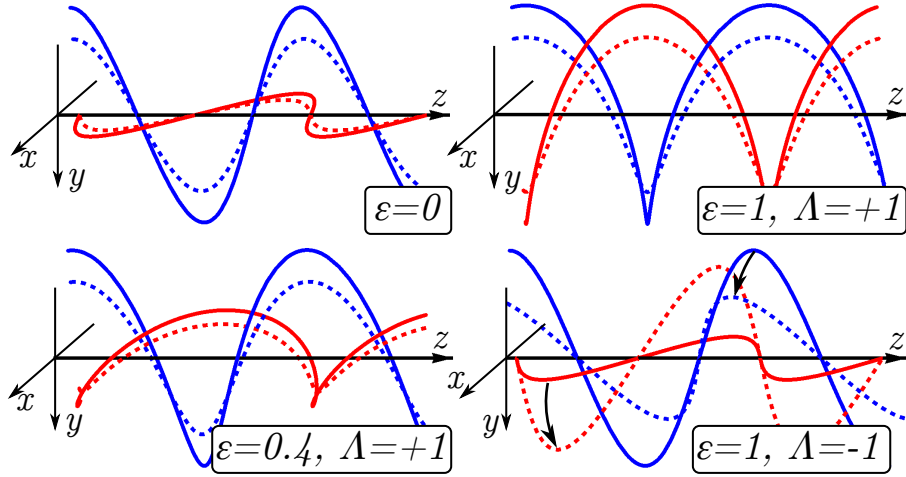


Figure 6.3: Standing light waves of different ellipticities ε and relative orientations Λ . The figures show the electric (red) and magnetic (blue) fields as functions of z for two different times $t = 0$ (solid) and $t = T_{\text{cycle}}/8$ (dashed) with the cycle length $T_{\text{cycle}} = 2\pi/\omega$.

propagating plane-wave laser modes $\mathbf{A}^{(1,2)}(\mathbf{r}, t)$ of equal intensity I , wavelength λ , ellipticity $-1 \leq \varepsilon \leq 1$ and with a relative orientation $\Lambda = \pm 1$,

$$\mathbf{A}^{(1)}(\mathbf{r}, t) = \frac{A_0}{\sqrt{1+\varepsilon^2}} (\cos(kz - \omega t)\mathbf{e}_x - \varepsilon \sin(kz - \omega t)\mathbf{e}_y), \quad (6.2a)$$

$$\mathbf{A}^{(2)}(\mathbf{r}, t) = \frac{A_0}{\sqrt{1+\varepsilon^2}} (-\cos(kz + \omega t)\mathbf{e}_x + \Lambda\varepsilon \sin(kz + \omega t)\mathbf{e}_y), \quad (6.2b)$$

with the amplitude A_0 , the frequency $\omega = 2\pi c/\lambda$ and the wave number $k = \omega/c$. As one can see from Eqs. (6.2), the two modes are *counter-rotating* for $\Lambda = -1$ and *co-rotating* for $\Lambda = +1$. The resulting vector potentials $\mathbf{A}_\Lambda(\mathbf{r}, t) = \mathbf{A}^{(1)}(\mathbf{r}, t) + \mathbf{A}^{(2)}(\mathbf{r}, t)$ of the standing light wave for the two relative orientations Λ are then given by

$$\mathbf{A}_{+1}(\mathbf{r}, t) = 2 \frac{A_0}{\sqrt{1+\varepsilon^2}} \sin(\omega t) (\sin(kz)\mathbf{e}_x + \varepsilon \cos(kz)\mathbf{e}_y), \quad (6.3a)$$

$$\mathbf{A}_{-1}(\mathbf{r}, t) = 2 \frac{A_0}{\sqrt{1+\varepsilon^2}} \sin(kz) (\sin(\omega t)\mathbf{e}_x - \varepsilon \cos(\omega t)\mathbf{e}_y). \quad (6.3b)$$

We will measure the intensity and ponderomotive energy of the standing light wave in terms of the corresponding values for each individual mode, given by $I = A_0^2 \omega^2 c / (8\pi)$ and $U_p = A_0^2 / 4$, respectively.

In order to comprehend the standing light wave as defined by the vector potentials (6.3), it is instructive to examine the electric and magnetic fields that correspond to $\mathbf{A}_\Lambda(\mathbf{r}, t)$ via Eqs. (2.2) with $\phi(\mathbf{r}, t) = 0$. The fields are shown in Fig. 6.3 for different parameters. In particular, for a relative orientation $\Lambda = +1$ of the counter-propagating modes, the fields oscillate in time, while the field vectors have constant magnitude

and rotate around the beam axis for $\Lambda = -1$. We will see in Sec. 6.4 that the relative orientation has a pronounced impact on the PADs in the high-intensity KDE.

6.3 PHOTOIONIZATION PROBABILITY

Our aim here is to compute the PADs of photoelectrons emitted in the ATI driven by the laser fields defined by Eqs. (6.3). To this end, we start from the photoionization probability, given in terms of the SFA transition amplitude via [cf. Eq. (3.4)]

$$\mathbb{P}(\mathbf{p}) = \mathbf{p} |\mathbb{T}(\mathbf{p})|^2 \approx \mathbf{p} |\mathbb{T}_0(\mathbf{p})|^2, \quad (6.4)$$

and where, as in Chap. 5, we approximate the full transition amplitude $\mathbb{T}(\mathbf{p})$ by the direct amplitude (4.2). In order to compute $\mathbb{T}_0(\mathbf{p})$, we need to derive the explicit expressions of the nondipole Volkov states with the above vector potential.

6.3.1 Nondipole Volkov states

In the evaluation of the nondipole Volkov states (4.20), we proceed similarly to Sec. 5.3.1. However, since the present vector potential consists of two plane-wave modes instead of a single mode, the derivation is more intricate.

Let us begin by rewriting the vector potential $\mathbf{A}_\Lambda(\mathbf{r}, t)$ in the form (4.1),

$$\mathbf{A}(\mathbf{r}, t) = \text{Re} \left\{ \int d^3\mathbf{k} \mathbf{a}(\mathbf{k}) e^{i\mathbf{u}_\mathbf{k}} \right\} = \int d^3\mathbf{k} \mathbf{A}(\mathbf{k}, t), \quad (6.5a)$$

with $\mathbf{u}_\mathbf{k} = \mathbf{k} \cdot \mathbf{r} - \omega_\mathbf{k} t$, $\omega_\mathbf{k} = kc$ and the Fourier coefficients

$$\mathbf{a}(\mathbf{k}) = \frac{A_0(\mathbf{k})}{\sqrt{1 + \varepsilon^2(\mathbf{k})}} (\mathbf{e}_1(\mathbf{k}) + i\varepsilon(\mathbf{k})\mathbf{e}_2(\mathbf{k})) (\delta(\mathbf{k} - \mathbf{k}_1) + \delta(\mathbf{k} - \mathbf{k}_2)). \quad (6.5b)$$

Here, we defined $\mathbf{k}_1 = \omega_1/c\mathbf{e}_z$, $\mathbf{k}_2 = -\omega_2/c\mathbf{e}_z$, $A_0(\mathbf{k}_j) = A_0^{(j)}$, $\varepsilon(\mathbf{k}_1) = \varepsilon$, $\varepsilon(\mathbf{k}_2) = \Lambda\varepsilon$, $\mathbf{e}_1(\mathbf{k}_1) = -\mathbf{e}_1(\mathbf{k}_2) = \mathbf{e}_x$ and $\mathbf{e}_2(\mathbf{k}_1) = \mathbf{e}_2(\mathbf{k}_2) = \mathbf{e}_y$. Since it does not introduce further difficulties in the following derivation, we allow for different amplitudes $A_0^{(1)}$, $A_0^{(2)}$ and frequencies ω_1 , ω_2 of the two counter-propagating modes and specialize only in our explicit computations to the case $A_0^{(1)} = A_0^{(2)} = A_0$ and $\omega_1 = \omega_2 = \omega$. This procedure is helpful in order to distinguish the two modes in the expressions below.

Based on the vector potential (6.5), the functions defined in Eqs. (4.11) can be evaluated in a similar way as for a plane-wave laser beam (cf. App. D.2). Due to the

occurring delta functions, the integrals in the modified Volkov phase (4.20b) can then easily be solved and the following form of the nondipole Volkov states is obtained:

$$\chi_{\mathbf{p}}(\mathbf{r}, t) = \frac{1}{(2\pi)^{3/2}} e^{-i(E_{\mathbf{p}}t - \mathbf{p} \cdot \mathbf{r})} e^{-i\Gamma(\mathbf{r}, t)}, \quad (6.6a)$$

$$\begin{aligned} \Gamma(\mathbf{r}, t) = & \alpha_1^- u_1 + \rho_1 \sin(u_1 + \theta_1) + \alpha_1^+ \sin(2u_1) \\ & + \alpha_{12}^+ \sin(u_1 + u_2) + \alpha_{12}^- \sin(u_1 - u_2) + [1 \leftrightarrow 2], \end{aligned} \quad (6.6b)$$

where we have introduced the short notation $u_j = u_{\mathbf{k}_j}$ and $[1 \leftrightarrow 2]$ denotes a repetition of all previous terms with the indices 1 and 2 interchanged. Furthermore, the coefficients in $\Gamma(\mathbf{r}, t)$ are explicitly given by

$$\alpha_1^- = \frac{(A_0^{(1)})^2}{4\omega_1} \frac{1}{p_z/c - 1}, \quad (6.7a)$$

$$\alpha_2^- = -\frac{(A_0^{(2)})^2}{4\omega_2} \frac{1}{p_z/c + 1}, \quad (6.7b)$$

$$\alpha_{1,2}^+ = \frac{\alpha_{1,2}^-}{2} \frac{1 - \varepsilon^2}{1 + \varepsilon^2}, \quad (6.7c)$$

$$\rho_1 = \frac{A_0^{(1)}}{\omega_1 \sqrt{1 + \varepsilon^2}} \frac{\sqrt{p_x^2 + \varepsilon^2 p_y^2}}{p_z/c - 1}, \quad (6.7d)$$

$$\rho_2 = -\frac{A_0^{(2)}}{\omega_2 \sqrt{1 + \varepsilon^2}} \frac{\sqrt{p_x^2 + \varepsilon^2 p_y^2}}{p_z/c + 1}, \quad (6.7e)$$

$$\theta_1 = -\Lambda \theta_2 = \arctan\left(\varepsilon \frac{p_y}{p_x}\right), \quad (6.7f)$$

$$\alpha_{12}^+ = \alpha_{21}^+ = \frac{A_0^{(1)} A_0^{(2)}}{4} \frac{1 + \Lambda \varepsilon^2}{1 + \varepsilon^2} \frac{1}{p_z/c(\omega_1 - \omega_2) - (\omega_1 + \omega_2)}, \quad (6.7g)$$

$$\alpha_{12}^- = -\alpha_{21}^- = \frac{A_0^{(1)} A_0^{(2)}}{4} \frac{1 - \Lambda \varepsilon^2}{1 + \varepsilon^2} \frac{1}{p_z/c(\omega_1 + \omega_2) - (\omega_1 - \omega_2)}. \quad (6.7h)$$

A few comments are in order regarding the above expressions. First, the Volkov states are symmetric under an interchange of the modes 1 and 2, as one would expect from the symmetry of the problem. Second, for linear polarization ($\varepsilon = 0$), the nondipole Volkov states (6.6) with the coefficients (6.7) reduce to the expressions derived by Rosenberg and Zhou (1993). Third, the modified Volkov phase (6.6b) is not simply a sum of the expressions one would obtain for the photoelectron in only one of the modes [cf. Eq. (5.9)]. Although all respective terms occur in Eq. (6.6b), additional mixed terms arise due to the nonlinearity of the Schrödinger equation. Below, it will become clear that these terms are accountable for the virtual Compton scattering that leads to the high-intensity KDE.

In order to obtain a form of the nondipole Volkov states (6.6) that has a physical interpretation and is useful for the evaluation of the transition amplitude in Sec. 6.3.2, we expand them into plane-wave contributions in a way analogous to Sec. 5.3.1 using the Jacobi-Anger expansion (see App. A),

$$\begin{aligned}\chi_{\mathbf{p}}(\mathbf{r}, t) &= \frac{1}{(2\pi)^{3/2}} e^{-i(E_{\mathbf{p}}t - \mathbf{p}\cdot\mathbf{r})} e^{-i\Gamma(\mathbf{r}, t)} \\ &= \frac{1}{(2\pi)^{3/2}} \sum_{n_1, \dots, n_6 = -\infty}^{\infty} C_{n_1, \dots, n_6}(\mathbf{p}) e^{-i(E_{n_1, \dots, n_6}t - \mathbf{p}_{n_1, \dots, n_6}\cdot\mathbf{r})},\end{aligned}\quad (6.8)$$

with the plane-wave expansion coefficients

$$C_{n_1, \dots, n_6}(\mathbf{p}) = J_{n_1}(\rho_1) J_{n_2}(\rho_2) J_{n_3}(\alpha_1^+) J_{n_4}(\alpha_2^+) J_{n_5}(2\alpha_{12}^+) J_{n_6}(2\alpha_{12}^-) e^{-in_1\theta_1} e^{-in_2\theta_2}, \quad (6.9)$$

and where the respective energies and momenta of the individual plane waves are

$$\begin{aligned}E_{n_1, \dots, n_6} &= E_{\mathbf{p}} - \alpha_1^- \omega_1 - \alpha_2^- \omega_2 - (n_1 + 2n_3 + n_5 + n_6)\omega_1 \\ &\quad - (n_2 + 2n_4 + n_5 - n_6)\omega_2,\end{aligned}\quad (6.10a)$$

$$\begin{aligned}\mathbf{p}_{n_1, \dots, n_6} &= \mathbf{p} - \alpha_1^- \mathbf{k}_1 - \alpha_2^- \mathbf{k}_2 - (n_1 + 2n_3 + n_5 + n_6)\mathbf{k}_1 \\ &\quad - (n_2 + 2n_4 + n_5 - n_6)\mathbf{k}_2.\end{aligned}\quad (6.10b)$$

These nondipole Volkov states for the photoelectron in the laser field formed by two counter-propagating plane-wave modes are the direct analogue to Eqs. (5.10) for a single-mode plane-wave laser field. Indeed, if we turn off one of the two laser modes by setting $A_0^{(2)} = 0$, $\alpha_2^- = \alpha_2^+ = \rho_2 = \alpha_{12}^+ = \alpha_{12}^- = 0$ and the corresponding Bessel functions in Eq. (6.9) become Kronecker deltas, $J_{n_j}(0) = \delta_{n_j, 0}$. Equation (6.8) then reduces to Eq. (5.10).

Finally, in order to cast the nondipole Volkov states into a more accessible form, we write $N_1 = n_1 + 2n_3 + n_5$, $N_2 = n_2 + 2n_4 + n_5$ and $N_{12} = n_6$, and use that $A_0^{(1)} = A_0^{(2)}$, $\omega_1 = \omega_2 = \omega$ and $\mathbf{k}_1 = -\mathbf{k}_2 = \mathbf{k}$ for the standing light wave:

$$\chi_{\mathbf{p}}(\mathbf{r}, t) = \frac{1}{(2\pi)^{3/2}} \sum_{N_1, N_2, N_{12} = -\infty}^{\infty} C_N(\mathbf{p}) e^{-i(E_N t - \mathbf{p}_N \cdot \mathbf{r})}, \quad (6.11a)$$

$$E_N = E_{\mathbf{p}} + 2\tilde{U}_{\mathbf{p}} - (N_1 + N_2)\omega, \quad (6.11b)$$

$$\mathbf{p}_N = \mathbf{p} + \frac{2\tilde{U}_{\mathbf{p}} p_z}{c\omega} \mathbf{k} - (N_1 - N_2)\mathbf{k} - 2N_{12}\mathbf{k}, \quad (6.11c)$$

where $N = (N_1, N_2, N_{12})$, $C_N(\mathbf{p})$ denotes the corresponding expansion coefficients that arise from Eq. (6.9), and $\tilde{U}_{\mathbf{p}} = U_{\mathbf{p}}/(1 - (p_z/c)^2)$. The above nondipole Volkov states allow the following interpretation: the individual terms in Eq. (6.11) denote

different contributions to the interaction of the photoelectron with the standing wave. The absorption of N_1 and N_2 photons from the laser modes $\mathbf{A}^{(1)}$ and $\mathbf{A}^{(2)}$, respectively, changes the photoelectron energy and momentum by $(N_1 + N_2)\omega$ and $(N_1 - N_2)\mathbf{k}$, respectively. Moreover, the photoelectron may absorb N_{12} photons from one mode and emit the same number into the *other*, which leaves its energy constant but changes its momentum by $2N_{12}\hbar\mathbf{k}$. This is the virtual Compton scattering process described in Sec. 6.1 that leads to a momentum transfer Δp_z along the beam axis to a photoelectron emitted within a certain ATI peak (fixed energy) and hence to the characteristic deflection of electrons in the high-intensity KDE.

6.3.2 SFA transition amplitude

With the nondipole Volkov states in the form (6.11), we can now evaluate the direct SFA transition amplitude for the ATI of an atomic target by a standing light wave. As for the continuous plane-wave laser beam considered in the previous chapter, the first term in the transition amplitude (4.2) vanishes. If we insert Eq. (6.11) and the initial state (3.29) into Eq. (4.2), we find

$$\begin{aligned} \mathbb{T}_0(\mathbf{p}) &= -i \int_{-\infty}^{\infty} d\tau \langle \chi_{\mathbf{p}}(\tau) | V(\mathbf{r}) | \Psi_0(\tau) \rangle \\ &= -2\pi i \sum_{N_1, N_2, N_{12}=-\infty}^{\infty} C_N(\mathbf{p}) V(p_N) \delta(E_N + I_p), \end{aligned} \quad (6.12)$$

where the matrix element $V(p_N)$ of the Coulomb potential $V(\mathbf{r})$ is given by Eq. (3.32) multiplied with a phase factor $e^{-ip_z z_0}$ due to the target position.

6.3.3 Computation of polar-angle distributions

In order to obtain the PADs discussed below, we numerically compute the differential ionization probability (6.4) with the transition amplitude (6.12) as a function of photoelectron energy $E_p = p^2/2$ and polar angle ϑ_p for fixed laser parameters $A_1^{(0)} = A_2^{(0)}$, $\omega_1 = \omega_2$, ε and $\Lambda = \pm 1$, as well as ionization potential I_p . The azimuthal angle is set to zero, $\varphi_p = 0$. For fixed photoelectron energy E_p , the PADs are then defined via $(\vartheta_p, \mathbb{P}(E_p, \vartheta_p, \varphi_p = 0))$. Since the transition amplitude is invariant under $\vartheta_p \rightarrow -\vartheta_p$, we consider only the range $0 \leq \vartheta_p \leq \pi$ and discretize it into 40 – 100 values. The differential ionization probability $\mathbb{P}(E_p, \vartheta_p, \varphi_p = 0)$ is then numerically computed via the following steps:

1. Reduce to finite summations: The argument of each Bessel function in the expansion coefficients (6.9) determines a cut-off for the respective index n_j beyond which the Bessel function drops off exponentially, $J_{n_j}(x) \sim e^{-n_j}$ for $|n_j| > |x| = n_{j,\max}$. To good approximation, the six infinite sums can therefore be reduced to the ranges $-n_{j,\max} \leq n_j \leq n_{j,\max}$.
2. Find positions of ATI peaks: The possible photoelectron energies (ATI peaks) measured at the detector are determined by the requirement that the argument of the delta function in Eq. (6.12) vanishes,

$$E_p - 2\tilde{U}_p - (N_1 + N_2)\omega + I_p = 0. \quad (6.13)$$

For N_1 and N_2 within the ranges set by the cut-offs from step 1, the solutions to this equation yield the possible values for E_p . Note that $\tilde{U}_p = U_p/(1 - (p_z/c)^2)$ is a function of $p_z = \sqrt{2E_p} \cos \vartheta_p$. Therefore, the above equation is not trivial, but is a polynomial of order four in $\sqrt{E_p}$. However, the solutions only slightly depend on ϑ_p because of the factor $1/c^2$ occurring in the denominator of \tilde{U}_p .

3. Compute \mathbb{P} : For each polar angle ϑ_p and photoelectron energy E_p , the differential ionization probability is now given by

$$\mathbb{P}(E_p, \vartheta_p, \varphi_p = 0) = (2\pi)^2 \sqrt{2E_p} \left| \sum_{n_1, \dots, n_6} C_{n_1, \dots, n_6}(\mathbf{p}) V(p_{n_1, \dots, n_6}) \right|^2, \quad (6.14)$$

where the summations run over all n_j that satisfy $N_1 = n_1 + 2n_3 + n_5$ and $N_2 = n_2 + 2n_4 + n_5$ for the values N_1 and N_2 giving rise to the value E_p according to step 2. The summation over n_6 runs over the range $-n_{6,\max} \leq n_6 \leq n_{6,\max}$.

6.3.4 Target position

In our computations, we consider a single atomic target that is placed on the beam axis at some position $z = z_0$. However, a realistic experimental target consists of a cloud of atoms distributed over some range $z_1 \leq z \leq z_2$ and also extends in the polarization plane. Since the ATI, as a nonlinear process, depends strongly on the intensity of the laser field at the target position, it is important to understand the influence of the target position in our theory in order to obtain experimentally realistic results.

Since we model the counter-propagating laser modes forming the standing wave as plane-wave fields, the intensity does not depend on the x and y coordinates. We can therefore consider a target placed on the beam axis ($x = y = 0$). If the target

is not placed at a node of the laser field ($z_0 = n\lambda/2$) for $\varepsilon = 0$, we found that the PADs always exhibit the same qualitative behavior. Therefore, in our computations, we always choose $z_0 = \lambda/8$. In general, this underestimates the momentum transfer for linearly polarized standing waves as measured in an experiment but will not change our main conclusions. For circular polarization, the results match the average distributions expected for a realistic cloud of atoms. For the discussion below, it is therefore sufficient to assume a single atom, placed at $z = z_0$, as the target.

6.4 RESULTS

With the photoionization probability (6.14) for the ATI of atoms in a standing light wave that we derived in the previous section, we now turn to the calculation of PADs for specific experimental parameters. Here, we are guided by the experiment of Bucksbaum et al. (1988), who used linearly and circularly polarized standing light waves with wavelength $\lambda = 1064$ nm and intensity $I = 8 \times 10^{13}$ W/cm², as well as a Xe gas target. Since it is not clear how the intensity I of the standing wave was defined in this experiment, we will for convenience set $\lambda = 1200$ nm in the following and assume a Kr target with ionization potential $I_p = 14$ eV. We will begin our discussion with the case of linear polarization and afterwards turn to the more general case of elliptical polarization.

Our analysis will be restricted to photoelectrons emitted in the $p_x - p_z$ -plane, that is, with azimuthal angle $\varphi_p = 0$. The PADs shown in the figures below are then computed according to the procedure outlined in Sec. 6.3.3. In particular, we are interested in the *momentum transfer* from the standing wave to a photoelectron with a particular energy E_p . It is defined as $\Delta p_z = \sqrt{2E_p} \cos \vartheta_{p,\max}$, where $\vartheta_{p,\max}$ is the position of a maximum in the PAD. Although this definition corresponds to the one of the peak shift in Chap. 5, it is common to call Δp_z the momentum transfer in the context of the high-intensity KDE. In order to obtain Δp_z , the maximum $\vartheta_{p,\max}$ is read off manually from the PADs.

As shown in Fig. 6.4 (a), for a linearly polarized standing wave ($\varepsilon = 0$) of intensity $I = 5 \times 10^{13}$ W/cm² ($U_p \approx 1.2$ eV) the PADs exhibit four maxima symmetric to the polarization plane ($\vartheta_p = 90^\circ$). This splitting in four maxima is the high-intensity KDE (cf. Fig. 6.2). The PADs have a similar shape for all photoelectron energies E_p . Although the positions $\vartheta_{p,\max}$ of the maxima depend on E_p , the respective transferred momenta $\Delta p_z \approx 560\hbar k$ are equal and comparable to the experimental results of Bucksbaum et al. (1988). Such an energy-independent momentum transfer leads to a polar angle $\vartheta_{p,\max}$ that follows the inverse square root law $\cos \vartheta_{\max} \sim E^{-1/2}$ as obtained also within the QED-Volkov approach (Guo and Drake, 1992).

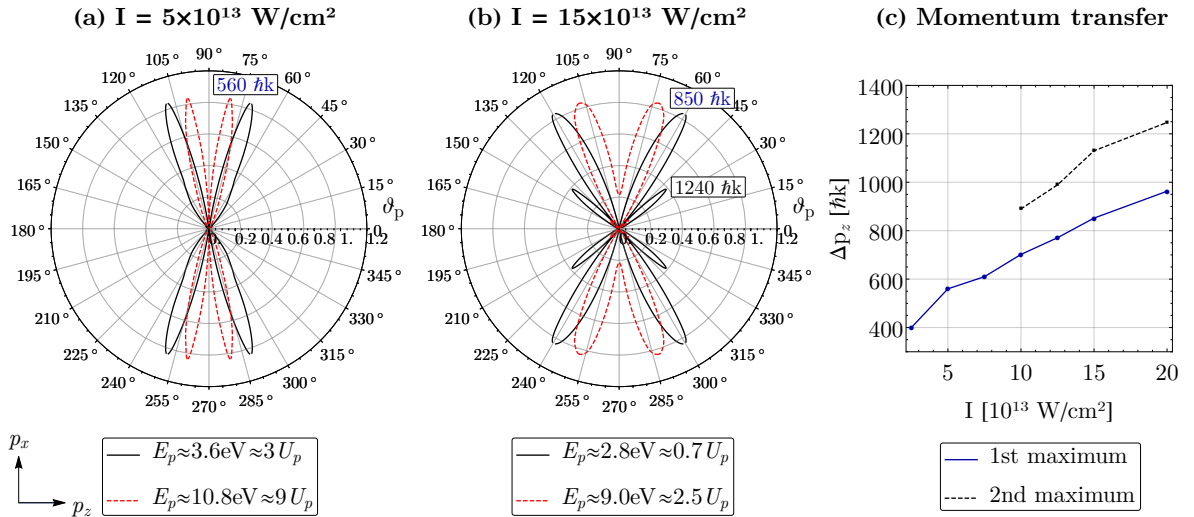


Figure 6.4: Momentum transfer in the high-intensity KDE with linearly polarized standing light waves ($\varepsilon = 0$). PADs of photoelectrons with $E_p \approx 3\omega$ (black solid) and $E_p \approx 10\omega$ (red dashed) are shown in the left two panels for two intensities: (a) $I = 5 \times 10^{13} \text{ W/cm}^2$ and (b) $I = 15 \times 10^{13} \text{ W/cm}^2$. In (a), both PADs refer to high-energy photoelectrons ($E_p > U_p$) and exhibit one set of maxima, corresponding to a momentum transfer $\Delta p_z \approx 560\hbar k$. In (b), in contrast, only the red dashed curve represents high-energy photoelectrons ($\Delta p_z \approx 850\hbar k$), while the black solid curve belongs to low-energy photoelectrons ($E_p < U_p$) and has an additional set of maxima ($\Delta p_z \approx 1240\hbar k$). (c) Momentum transfer to photoelectrons with energy $E_p \approx 3\omega$, corresponding to the maxima in their PADs, as a function of intensity. For $I \geq 10 \times 10^{13} \text{ W/cm}^2$, $E_p < U_p$ and the second set of maxima appears. The PADs in (a) and (b) are normalized to their respective maxima and the absolute magnitudes of the red dashed curves differ from the black solid curves by a factor of (a) 0.93 and (b) 0.71, respectively. Parameters used: $\lambda = 1200 \text{ nm}$ ($\omega = 1.03 \text{ eV}$), $I_p = 14 \text{ eV}$ (Kr target).

In Fig. 6.4 (b), we show the PADs computed for a higher intensity $I = 15 \times 10^{13} \text{ W/cm}^2$ of the standing wave. Here, the four maxima are also clearly discernible for *high-energy photoelectrons* (black solid curve) with $E_p > U_p \approx 4 \text{ eV}$ and the corresponding momentum transfer has increased with the intensity to $\Delta p_z \approx 850\hbar k$. Most notably, however, is the PAD for *low-energy photoelectrons* (red dashed curve) with $E_p < U_p$. Here, in addition to the maxima corresponding to $\Delta p_z \approx 850\hbar k$, a second set of four maxima is visible that implies a considerably larger momentum transfer $\Delta p_z \approx 1250\hbar k$. This different behavior of low- and high-energy photoelectrons was not observed in previous measurements, because the experimental laser parameters did not allow the observation of photoelectrons with $E_p < U_p$ (see below).

The different PADs for low- and high-energy photoelectrons can be understood in terms of the ponderomotive force (6.1) which acts on the photoelectron in the standing light wave. From the three-step model (cf. Sec. 3.1), we expect that after tunneling through the barrier the photoelectron exits the atom with a velocity along

the laser polarization direction, i.e. along the x -axis. The ponderomotive force then induces an oscillating motion along the beam axis, i.e. along the z -axis. As in the free-electron KDE [see our discussion below Eq. (6.1)], for $E_p > U_p$ the motion of the photoelectron is not bounded by the ponderomotive potential and can thus be described classically, leading to a distinct value of the longitudinal momentum p_z measured at the detector (Bucksbaum et al., 1988). On the other hand, for $E_p < U_p$ the photoelectron cannot classically move over the crests of the ponderomotive potential and the plane-wave contributions with different p_z in its wave function (6.11) interfere, which gives rise to another set of maxima in the PADs.

We may therefore conclude that two distinct regimes exist in the high-intensity KDE, one characteristic for low-energy photoelectrons with $E_p < U_p$ and one characteristic for high-energy photoelectrons with $E_p > U_p$. These two regimes are quite analogous to the Bragg and diffraction regimes in the free-electron KDE. From a classical viewpoint, we expect that the momentum transfer measured in both regimes should be determined by the magnitude $U_p k \sim I$ of the ponderomotive force. Indeed, this linear dependence of Δp_z on I is found within our nondipole SFA description and is shown in Fig. 6.4 (c).

As we have seen in Fig. 6.4 (a), low-energy photoelectrons with $E_p < U_p$ cannot be observed under all conditions, since the ponderomotive energy $U_p = I\lambda^2/(2\pi c^3)$ has to be sufficiently large. More precisely, it has to be in the order of a few photon energies, $U_p \geq n\omega$. From this requirement, experimental parameters can be estimated to observe low-energy photoelectrons: if we assume that PADs of photoelectrons with $E_p \approx 3\omega$ can be measured reliably, we find from $U_p \geq 3\omega$ that the minimum intensity of the standing wave with wavelength λ must be

$$I_{\min} \left[\frac{\text{W}}{\text{cm}^2} \right] = 2.16 \times 10^{23} \times (\lambda [\text{nm}])^{-3}, \quad (6.15)$$

in order to resolve the second set of maxima in the PADs. This is in line with Fig. 6.4 (c), where the second maximum appears only above $I \approx I_{\min}$. According to this argument, photoelectrons with $E_p < U_p$ could not be observed in the experiment by Bucksbaum et al. (1988) because of the small $U_p \approx \omega$, and are not visible in Fig. 6.4 (a). However, current laser technologies are capable of producing standing light waves in this intensity domain (Faure et al., 2006) and it should therefore be possible to observe the previously unknown behavior of low-energy photoelectrons in future experiments on the high-intensity KDE.

As we have stated already above, the momentum transfer to low-energy photoelectrons also depends on the ellipticity of the standing light wave. This ellipticity dependence can be observed in Fig. 6.5, where we show PADs of low-energy pho-

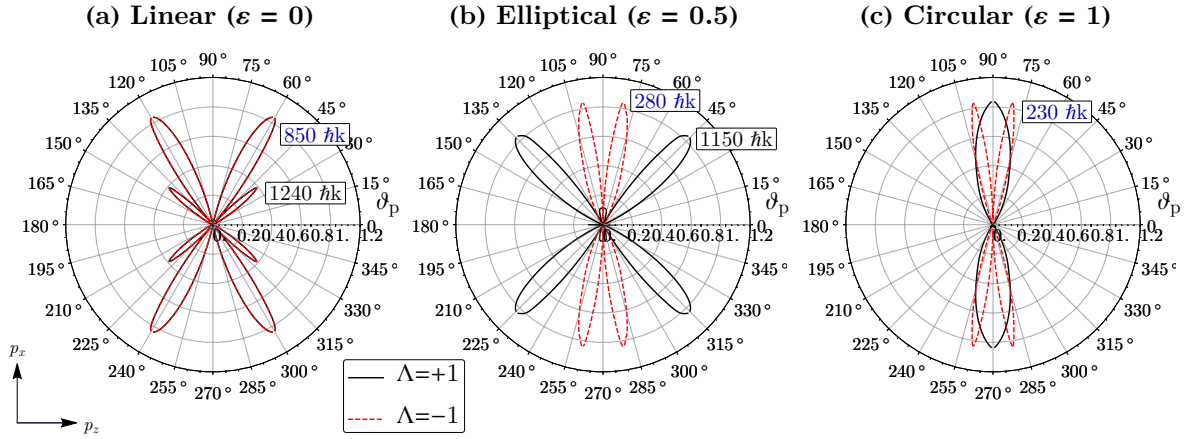


Figure 6.5: PADs of low-energy photoelectrons ($E_p = 2.8 \text{ eV} \approx 0.7U_p$) for (a) linear, (b) elliptical and (c) circular polarizations of the standing light wave. Results are shown for $I = 15 \times 10^{13} \text{ W/cm}^2$ and for both relative orientations $\Lambda = +1$ (black solid curves) and $\Lambda = -1$ (red dashed curves) of the counter-propagating laser modes. All PADs are normalized to their respective maxima and the absolute magnitudes of the red dashed curves differ from the black solid curves by a factor of (a) 1.0, (b) 0.33 and (c) 0.16, respectively. All other parameters are the same as in Fig. 6.4.

photoelectrons for three different ellipticities ($\varepsilon = 0$, $\varepsilon = 0.5$, $\varepsilon = 1$) and both relative orientations ($\Lambda = \pm 1$) of the standing wave. Note that both curves in Fig. 6.5 (a) are identical to the black curve in Fig. 6.4 (b). The red curves in Figs. 6.5 (a)–(c) show that for $\Lambda = -1$, the momentum transfer decreases if the ellipticity is increased and only one set of maxima remains for $\varepsilon > 0$. This is in contrast to the case of high-energy photoelectrons, where the momentum transfer is larger for circular than for linear polarization (Bucksbaum et al., 1988). Moreover, for $\Lambda = +1$, the momentum transfer vanishes for circular polarization, in agreement with Bucksbaum et al. (1988). The reason for this is that angular momentum conservation forbids the virtual Compton scattering process described in Sec. 6.1. However, the momentum transfer is (strongly) enhanced for an elliptically polarized standing wave with $\varepsilon = 0.5$ and $\Lambda = +1$: low-energy photoelectrons are emitted with a high probability with large longitudinal momenta ($\Delta p_z \approx 1150\hbar k$). We may therefore state that the momentum transfer to low-energy photoelectrons can be manipulated or controlled by a change of the ellipticity when all other parameters are fixed. Within the SFA formalism, this is a consequence of the ellipticity dependence of the expansion coefficients $C_N(\mathbf{p})$ in the Volkov states (6.11). Physically, the ponderomotive force field acting on the photoelectron is ellipticity-dependent (Smorenburg et al., 2011). In future work, it might be interesting to see how the (semi-)classical photoelectron dynamics in this polarization-dependent force field leads to the ellipticity dependent momentum transfer.

6.5 CONCLUSIONS

In this chapter, we have demonstrated how the nondipole SFA can be applied to a more complicated setup than the ATI driven by a single-mode plane-wave laser beam. We have considered the ATI of atoms in a standing light wave, in which the photoelectrons may be measured with very large longitudinal momenta, an effect known as the high-intensity KDE. The standing light wave is formed by two counter-propagating plane-wave laser beams, which allowed us to evaluate the nondipole Volkov states of Chap. 4 for a photoelectron in the standing light wave. Based on these Volkov states, we have calculated PADs of photoelectrons emitted in the high-intensity KDE and have shown that the results compare well with an existing experiment.

Furthermore, we have demonstrated that two regimes exist in the high-intensity KDE comparable to the Bragg and diffraction regimes in the free-electron KDE. While for high-energy photoelectrons one set of maxima is observed in the PADs, corresponding to a particular momentum transfer, low-energy photoelectrons exhibit two sets of maxima in their PADs and can be emitted with much larger longitudinal momenta. This large momentum transfer is experimentally accessible if the intensity of the standing wave exceeds a certain threshold I_{\min} that depends on the wavelength of the standing wave. Therefore, the nondipole SFA reveals that the high-intensity KDE allows the generation of low-energy photoelectrons with large and controllable longitudinal momentum. This might be utilized in future experiments and applications.

On the theoretical side, more work has to be done to better understand the ellipticity dependence of the momentum transfer. To this end, one might either work in the nondipole SFA or perform quantum-trajectory monte carlo simulations, in which the three-step model is employed and the dynamics of the photoelectron in the standing wave is simulated classically. Such simulations have been used by Bucksbaum et al. (1988) to explain their experimental findings and often allow a better insight into the underlying physical mechanism. In addition, it is necessary to understand the influence of Coulomb interactions between photoelectron and parent ion on the results discussed here. It is well-known from the ATI with single-mode plane-wave driving beams that the Coulomb potential significantly alters the low-energy part of the ATI spectra (Blaga et al., 2009) and one might therefore expect changes to our findings within the nondipole SFA. In general, however, the SFA underestimates the yield of low-energy photoelectrons in ATI and we can therefore expect that the inclusion of the Coulomb potential may further enhance the effect discussed above.

ATI WITH FEW-CYCLE BESSEL PULSES

In this chapter, we will investigate the ATI of localized atomic targets by intense few-cycle Bessel pulses, which are pulses formed from the Bessel beams introduced in Sec. 2.4. In order to compute ATI spectra within the SFA, we make use of a local dipole approximation (see Sec. 7.3.1). This approximation is only justified for short pulses and it does not include nondipole interactions. However, due to a longitudinal component of the electric field, we will find that photoelectrons can be emitted with a significant momentum component parallel to the beam axis. In Sec. 7.4, we will analyze the influence of the angular momentum as well as the opening angle of the pulse on this *forward emission*. Finally, in Sec. 7.5, we will briefly discuss the future extension of this work towards the nondipole SFA of Chap. 4

Parts of the material presented in this chapter were published previously in the following reference:

Above-threshold ionization by few-cycle Bessel pulses carrying orbital angular momentum

B. Böning, W. Paufler, and S. Fritzsche
PHYSICAL REVIEW A **98**, 023407 (2018)

7.1 TWISTED LIGHT IN ATOMIC PHYSICS

Owing to their non-vanishing orbital angular momentum, twisted laser beams and pulses have been of considerable interest in the interaction with atoms. Since they can nowadays routinely be generated using axicons (Arlt and Dholakia, 2000; McGloin and Dholakia, 2005), spiral phase plates (Beijersbergen et al., 1994) or computer-generated holograms (Heckenberg et al., 1992), both theory and experiments have studied processes driven by twisted light. In the perturbative regime, that is, for twisted light beams of low intensity, it was shown that the orbital angular momentum of the beam alters the single-photon ionization (Matula et al., 2013) and excitation

(Scholz-Marggraf et al., 2014; Schmiegelow et al., 2016; Peshkov et al., 2017) due to modified selection rules.

In the strong-field regime, twisted laser beams have especially been studied in the context of HHG. Here, it was shown that the angular momentum is transferred from the driving beam to the harmonic photons (Gariépy et al., 2014). This transfer enables the generation of high-energetic twisted beams and ultrashort pulses carrying orbital angular momentum, which can then be utilized to probe atoms and molecules (Hernández-García et al., 2017). In turn, the single-photon ionization of atoms driven by an ultrashort twisted pulse allows the inference of the local energy spectrum of the pulse (Müller et al., 2016).

In addition, two-color photoionization processes were theoretically investigated, in which a weak short-wavelength twisted pulse ionizes an atomic target in the presence of a strong plane-wave pulse. Depending on the details of the plane-wave pulse, either dichroism signals can be observed (Seipt et al., 2016; Baghdasaryan et al., 2019) or the temporal and spatial structure of the twisted pulse can be probed using the attosecond streaking technique (Böning et al., 2017).

While the role of the orbital angular momentum of light in HHG has been carefully investigated, less attention has been paid to the ATI of atoms driven by strong twisted light beams (Paufler et al., 2019). In a fully quantum-mechanical description of this process, it can be expected that the transfer of angular momentum from the laser beam to the photoelectron leads to significantly modified ATI spectra when compared to plane-wave driving beams. In other words, the spatial structure of the twisted beam (cf. Sec. 2.4) needs to be accounted for in the photoelectron continuum. The nondipole SFA developed in Chap. 4 allows this incorporation in terms of nondipole Volkov states. In this chapter, we will discuss a first step towards the description of ATI with twisted light beams, which, although it does not yet include nondipole interactions, already yields remarkable results.

7.2 SETUP AND PARAMETERS

The geometry of the setup considered in this chapter is shown in Fig. 7.1. A few-cycle Bessel pulse of duration T and wavelength λ interacts with a target consisting of a single atom that is placed at an impact parameter $\mathbf{b} = (b, \varphi_b, z_b = 0)$ with respect to the beam z -axis¹. As in previous chapters, the target is assumed to be in a hydrogen-like $1s$ initial state (3.29) with ionization potential I_p . Upon ionization, a photoelectron

¹ Indeed, such a localization is experimentally possible (Schmiegelow et al., 2016). We will briefly mention the extension to targets of finite size at the end of Sec. 7.4.

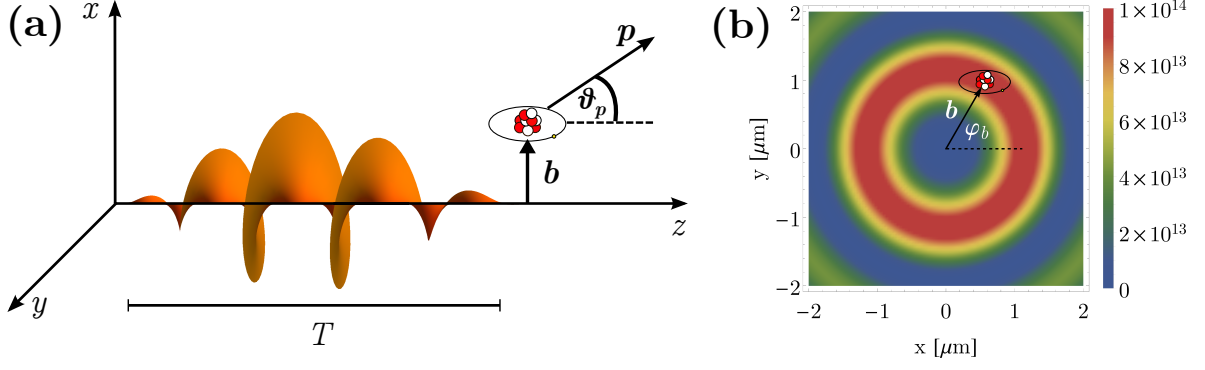


Figure 7.1: Setup of ATI with Bessel pulses. (a) ATI of a single atomic target with a few-cycle Bessel pulse (orange). The atom is localized at an impact parameter \mathbf{b} relative to the beam axis. Photoelectrons are emitted with momentum $\mathbf{p} = (p, \vartheta_p, \varphi_p)$. (b) Transverse intensity profile (in W/cm^2) of the Bessel pulse. The impact parameter is chosen so that the atomic target is placed on the first intensity maximum.

is emitted that is measured at the detector with momentum $\mathbf{p} = (p, \vartheta_p, \varphi_p)$ in spherical coordinates.

To describe Bessel pulses of a finite duration, we multiply the vector potential $\mathbf{A}_B(\mathbf{r}, t)$ of a continuous Bessel beam, given by Eqs. (2.32), by a \sin^2 -envelope of the form (2.22),

$$\mathbf{A}_p(\mathbf{r}, t) = f(t)\mathbf{A}_B(\mathbf{r}, t), \quad (7.1)$$

where $f(t) = A_0 \sin^2(\omega t/2n_p)$ for $0 \leq t \leq T = 2\pi n_p/\omega$ and $f(t) = 0$ otherwise. Here, n_p denotes the number of cycles comprising the pulse and we also introduced an amplitude A_0 in the envelope in order to control the maximum intensity of the Bessel pulse. We will measure the intensity of the pulse via the transverse intensity profile (2.29) of the continuous Bessel beam, which represents the limit of long pulse duration T . In the present case, Eq. (2.29) is modified by a factor A_0^2 . Note that, instead of multiplying the continuous Bessel beam with an envelope, one could also model a pulse as a weighted superposition of Bessel beams (2.28) in frequency space, which yields so-called X waves (Ornigotti et al., 2015). In order to obtain a simple model for a Bessel pulse, however, we only multiply by a temporal envelope.

In the computation of all the results presented in Sec. 7.4, we will again set the ionization potential $I_p = 14$ eV, applicable to a Kr target. Furthermore, we will choose a wavelength $\lambda = 800$ nm of the pulse and a maximum intensity of $I_{\max} = 10^{14}$ W/cm^2 . The remaining open parameters are then the pulse duration in terms of n_p , the helicity Λ , the TAM projection m_γ and the opening angle ϑ_k of the Bessel pulse (cf. Sec. 2.4). Since the intensity profile (2.29) of a Bessel beam depends on both m_γ and ϑ_k , the amplitude A_0 needs to be chosen depending on these parameters if the maximum intensity I_{\max} is required to be fixed.

7.3 PHOTOIONIZATION PROBABILITY

In order to compute PEMD and ATI spectra in the above setup, we start from the photoionization probability (3.4) in terms of the direct SFA transition amplitude (3.18),

$$\mathbb{P}_{\mathbf{b}}(\mathbf{p}) \approx p |\mathbb{T}_{0,\mathbf{b}}(\mathbf{p})|^2, \quad (7.2a)$$

$$\mathbb{T}_{0,\mathbf{b}}(\mathbf{p}) = - \langle \chi_{\mathbf{p}}(\tau) | \Psi_0(\tau) \rangle \Big|_0^{\mathbb{T}} - i \int_0^{\mathbb{T}} d\tau \langle \chi_{\mathbf{p}}(\tau) | V(\mathbf{r}) | \Psi_0(\tau) \rangle. \quad (7.2b)$$

Here, the subscripts \mathbf{b} indicate the parametric dependence on the impact parameter. Since the Bessel pulse is always locally circularly polarized (cf. Sec. 2.4), any rescattering of the photoelectron with the parent ion is suppressed and it is a good approximation to include only the direct transition amplitude, which we will explicitly evaluate below.

However, as we mentioned above and in the introduction to this dissertation, the dynamics of the photoelectron in a Bessel pulse is expected to be strongly influenced by nondipole interactions. That is, the nondipole Volkov states derived in Chap. 4 should be evaluated for the vector potential (7.1) and inserted as continuum states $|\chi_{\mathbf{p}}(\tau)\rangle$ in Eq. (7.2). Although this is a principle goal of the nondipole SFA for spatially structured laser fields, it goes beyond this dissertation and we will discuss this application of the nondipole SFA only at the end of this chapter in Sec. 7.5. Instead, we will here use the fact that nondipole contributions can be neglected if the Bessel pulse duration is sufficiently short.

7.3.1 Local dipole approximation

Let us assume that the photoelectron is ejected from the target atom and then propagates in the fields of the Bessel pulse. We can compute the distance it will propagate during the pulse duration \mathbb{T} . A sufficient estimate is obtained if, for simplicity, we consider a classical electron in a linearly polarized plane-wave laser pulse that has an electric field $\mathbf{E}(t) = E_0 \sin^2\left(\frac{\omega t}{2n_p}\right) \cos(\omega t) \mathbf{e}_x$ for $0 \leq t \leq 2\pi n_p/\omega$ and $\mathbf{E}(t) = 0$ otherwise. By integrating the classical equations of motion, $d^2\mathbf{x}/dt^2 = -\mathbf{E}(t)$, we find that the electron propagates over a distance of

$$\Delta x \approx n_p \lambda \left(3 \times 10^{-14} \sqrt{I [\text{W}/\text{cm}^2]} \lambda [\text{nm}] + \frac{v_0}{c} \right), \quad (7.3)$$

during the pulse duration \mathbb{T} , where v_0 is the initial electron velocity at $t = 0$. For typical parameters of $I = 10^{14} \text{ W}/\text{cm}^2$, $\lambda = 800 \text{ nm}$ and a rather high initial velocity of $v_0 = 1 \text{ a.u.}$, we find that $\Delta x \approx n_p \times 6 \text{ nm}$.

On the other hand, from the intensity profile in Fig. 7.1 (b), we see that the intensity of the Bessel pulse varies on a characteristic length scale of hundreds of nanometers. Therefore, the photoelectron does not see these spatial variations of the Bessel pulse over the time of propagation in the field. Thus, to a good approximation, we can neglect the influence of the spatial structure of the Bessel pulse on the dynamics of the photoelectron as long as the pulse is sufficiently short.

Based on this argument, we approximate the vector potential (7.1) at the position $\mathbf{r} = \mathbf{b}$ of the atom, $\mathbf{A}_{\mathbf{b}}(t) \approx \mathbf{A}_{\mathbf{p}}(\mathbf{b}, t)$ and call this the *local dipole approximation*. In the evaluation of the transition amplitude (7.2b), we can describe the electron continuum by the dipole Volkov states (3.25) with this purely time-dependent vector potential,

$$\chi_{\mathbf{p},\mathbf{b}}(\mathbf{r}, t) \approx \chi_{\mathbf{p}}^{(\text{VG})}(\mathbf{r}, t) = \frac{1}{(2\pi)^{3/2}} e^{-iS_{V,\mathbf{b}}(t)} e^{i\mathbf{p}\cdot\mathbf{r}}, \quad (7.4)$$

where $S_V(t)$ is the dipole Volkov phase. Note that we choose to work in velocity gauge in order to allow a comparison to a later extension to the nondipole SFA of Chap. 4. Since we consider a $1s$ initial state, we do not expect differences to results obtained within length gauge (Bauer et al., 2005).

Let us remark again at this point that the dynamics of the electron in the local field of the Bessel pulse may still be significantly different from that in a plane-wave pulse of the form (3.35) since the Bessel pulse vector potential has a longitudinal component $A_{\mathbf{b},z}(t)$ in addition to its transversal components $A_{\mathbf{b},x}(t)$ and $A_{\mathbf{b},y}(t)$. We will see in Sec. 7.4 that this has a influence on the ATI spectra.

7.3.2 SFA transition amplitude

We can now readily evaluate the dipole Volkov states (7.4) for the vector potential $\mathbf{A}_{\mathbf{b}}(t)$ at the position of the target atom. To this end, we need to carry out the t -integral in the dipole Volkov phase $S_{V,\mathbf{b}}(t)$. In principle, this integration is straightforward. Due to the three components of the Bessel pulse vector potential (7.1) with (2.32), however, the calculation is quite extensive and we only state the result at this point:

$$\begin{aligned} S_{V,\mathbf{b}}(t) &= \frac{1}{2} \int^t d\tau (\mathbf{p} + \mathbf{A}_{\mathbf{b}}(\tau))^2 \\ &= \frac{1}{2} \int^t d\tau \left(p^2 + p_x A_{P,x}(\mathbf{b}, \tau) + p_y A_{P,y}(\mathbf{b}, \tau) + p_z A_{P,z}(\mathbf{b}, \tau) + \mathbf{A}_{\mathbf{p}}^2(\mathbf{b}, \tau) \right) \\ &= \beta t + \sum_{j=1}^9 \gamma_j \cos(\varphi_j^{(c)} - \omega_j^{(c)} t) + \sum_{l=1}^{13} \sigma_l \sin(\varphi_l^{(s)} - \omega_l^{(s)} t). \end{aligned} \quad (7.5)$$

We have expressed $S_{V,b}(t)$ in a form that resembles the dipole Volkov phase for a plane-wave driving laser pulse derived in App. B. In Eq. (7.5), the introduced Fourier coefficients β , γ_j , σ_l and frequencies $\omega_j^{(c)}$, $\omega_l^{(s)}$ as well as the phases $\varphi_j^{(c)}$, $\varphi_l^{(s)}$ depend on the laser parameters A_0 , n_p , ω , Λ , m_γ , ϑ_k , the impact parameter \mathbf{b} and the photoelectron momentum \mathbf{p} . We state their explicit form in App. B.2. Physically, the frequencies $\omega_j^{(c)}$ and $\omega_l^{(s)}$ describe the quiver motion of the photoelectron in the field of the Bessel pulse and define the positions of the peaks in the ATI spectra.

The direct SFA transition amplitude (7.2b) can be reexpressed using the Volkov states (7.4),

$$T_{0,b}(\mathbf{p}) = -\langle \mathbf{p} | \Phi_0 \rangle e^{i(S_{V,b}(t) + I_p t)} \Big|_0^T - i \langle \mathbf{p} | V(\mathbf{r}) | \Phi_0 \rangle \int_0^T dt e^{i(S_{V,b}(t) + I_p t)}, \quad (7.6)$$

where the matrix element $\langle \mathbf{p} | V(\mathbf{r}) | \Phi_0 \rangle$ of the Coulomb potential and the momentum-space initial state wave function $\langle \mathbf{p} | \Phi_0 \rangle$ are given by Eqs. (3.32) and (3.37), respectively. The remaining task in computing the transition amplitude (7.6) for given pulse parameters and photoelectron momentum \mathbf{p} is the evaluation of $e^{iS_{V,b}(t)}$ and its integral. These computations will be performed numerically based on Eq. (7.5). The ATI spectra discussed in the following section are then given by the photoionization probability (7.2a) as a function of energy for fixed emission angles ϑ_p and φ_p of the photoelectron: $P(E_p) = \mathbb{P}_b(E_p, \vartheta_p, \varphi_p)$, where \mathbb{P}_b is numerically evaluated according to Eq. (7.2a). In principle, one could also perform a Jacobi-Anger expansion of the exponentials in Eq. (7.6), in line with our procedure in the previous two chapters. However, since this would not lead to further physical insight and only a one-dimensional integral occurs in the transition amplitude, its numerical evaluation is more appropriate.

7.4 RESULTS

We now use our result (7.6) for the SFA transition amplitude to compute the ATI spectra for the ionization of a single atom in a strong Bessel pulse. Thereby, our focus will be on photoelectrons emitted with $\vartheta_p \neq \pi/2$, i.e. with a momentum component along the beam axis. We will analyze the resulting ATI spectra for different laser parameters, in particular, for different TAM projections m_γ and opening angles ϑ_k of the Bessel pulse. Accordingly, we will fix all other parameters: the wavelength $\lambda = 800$ nm, the number of cycles $n_p = 2$, the maximum intensity $I_{\max} = 10^{14}$ W/cm², the helicity $\Lambda = +1$ and the ionization potential $I_p = 14$ eV. For each set of parameters m_γ and ϑ_k , the target atom is then placed at the impact parameter $\mathbf{b} = (b_{\max}, \varphi_b = 0, z = 0)$, where b_{\max} is the respective radial coordinate of maximum intensity I_{\max} [cf. Fig. 7.1 (b)].

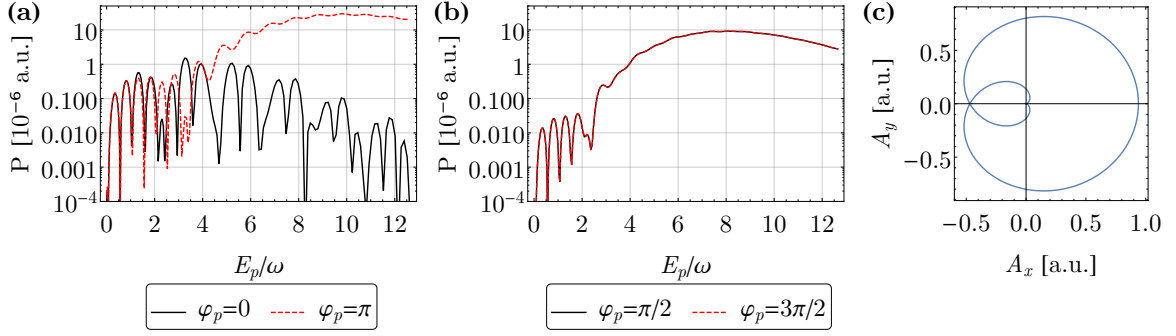


Figure 7.2: ATI with a 2-cycle Bessel pulse in the plane-wave limit (opening angle $\vartheta_k = 1$ deg. and TAM projection $m_\gamma = \Lambda = +1$). The ATI spectra are shown for photoelectrons emitted in the polarization plane ($\vartheta_p = \pi/2$) along the (a) $\pm x$ -directions ($\varphi_p = 0, \pi$) and (b) $\pm y$ -directions ($\varphi_p = \pi/2, 3\pi/2$). (c) Vector potential as a function of time. Parameters used: $\lambda = 800$ nm, $I_{\max} = 10^{14}$ W/cm 2 , $I_p = 14$ eV.

In order to take up the results discussed in Sec. 3.4 for plane-wave pulses, we first consider the ATI spectra computed for the ionization by a Bessel pulse in the *plane-wave limit*. As we have explained in Sec. 2.4, the Bessel vector potential (2.28) coincides with a circularly polarized (in the $x - y$ -plane) plane wave of helicity Λ in the limit $\vartheta_k \ll 1$ and $m = \Lambda$. Accordingly, in this limit, the vector potential (7.1) of the Bessel pulse becomes

$$\mathbf{A}_p(\mathbf{r}, t) = \tilde{A}_0 \sin^2\left(\frac{\omega t}{2n_p}\right) (\cos(\omega t - k_z z) \mathbf{e}_x + \Lambda \sin(\omega t - k_z z) \mathbf{e}_y), \quad (7.7)$$

where we have defined $\tilde{A}_0 = A_0 \sqrt{\frac{\pi}{4\pi}}$. That is, for $z = z_b = 0$, $\mathbf{A}_p(\mathbf{b}, t)$ is identical to the plane-wave pulse (3.35) with $\varepsilon = 1$ and $\phi_{\text{CEP}} = 0$ that we considered in Sec. 3.4. As a function of time it is illustrated in Fig. 7.2 (c).

In order to compute ATI spectra in the plane-wave limit, we start from our general result for the transition amplitude (7.6) and the Volkov phase (7.5). We consider photoelectrons emitted in the polarization plane ($\vartheta_p = \pi/2$) and vary the azimuthal angle φ_p . The resulting ATI spectra for four different azimuthal angles ($\varphi_p = 0, \pi$ and $\varphi_p = \pi/2, 3\pi/2$) are displayed in Figs. 7.2 (a) and (b). As one would expect, these figures are similar to those computed directly from the vector potential (7.7) in Sec. 3.4 and by (Milošević et al., 2006): for $\varphi_p = 0$, the characteristic ATI peaks can be observed and the symmetries of the ATI spectra observed in different directions φ_p mirror those of the vector potential in Fig. 7.2 (c). In particular, we see a pronounced asymmetry of the spectra in $\pm x$ -direction [Fig. 7.2 (a)]. Moreover, some ATI peaks are suppressed in Figs. 7.2 (a) and (b), which results from the short pulse duration of the ionizing pulse. The peaks would become more regular with increasing pulse duration due to interferences from many optical cycles (cf. our discussion in Sec. 3.4). These results in the plane-wave limit of the Bessel pulse show that our computations

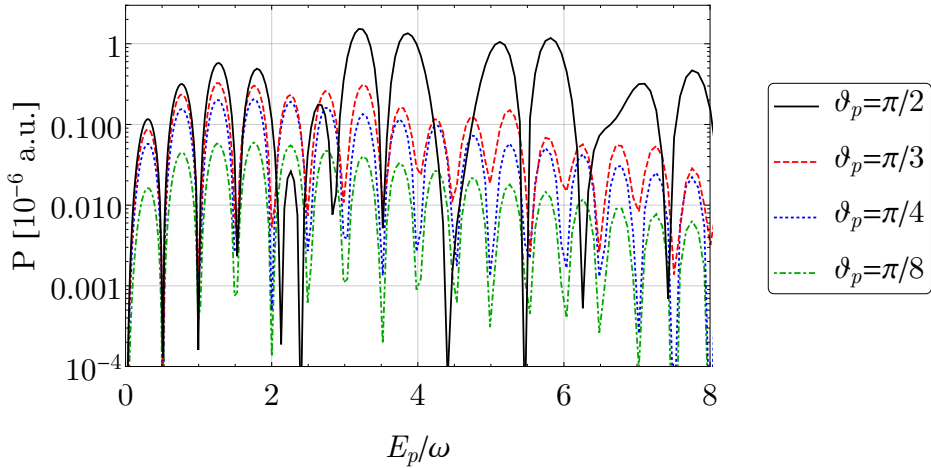


Figure 7.3: ATI spectra computed for different polar angles ϑ_p and an azimuthal angle $\varphi_p = 0$. Results are shown for a Bessel pulse with TAM projection $m_\gamma = 2$ and opening angle $\vartheta_k = 20$ deg. The target atom was placed at impact parameter $\mathbf{b} = (b_{\max}, \varphi_b = 0, z_b = 0)$, where b_{\max} is the radial coordinate of maximum intensity of the pulse. All other parameters are the same as in Fig. 7.2.

are consistent and we can now turn to the general case of the ATI with a Bessel pulse of arbitrary TAM and opening angle.

We have already mentioned above that the most characteristic property of the Bessel pulse vector potential (7.1) is its nonzero z -component. We can understand the consequences for the ionization dynamics in the present case from the classical conservation of canonical momentum of the photoelectron,

$$\mathbf{p}(t_0) - \mathbf{A}_p(\mathbf{b}, t_0) = \mathbf{p}(t \rightarrow \infty) - \mathbf{A}_p(\mathbf{b}, t \rightarrow \infty), \quad (7.8)$$

where t_0 is the time when, in the sense of the three-step model, the photoelectron tunnels out of the atom and enters the laser field, and $\mathbf{A}_p(\mathbf{b}, t \rightarrow \infty) = 0$. From the above equation, we expect that the photoelectron gains a momentum component $p_z(t \rightarrow \infty)$ along the propagation direction of the ionizing pulse if $A_{p,z}(\mathbf{b}, t_0) \neq 0$. The magnitude of p_z is then proportional to $A_{p,z}(\mathbf{b}, t_0)$. Motivated by this classical reasoning, we now analyze the ATI spectra of photoelectrons for $\vartheta_p \neq \pi/2$, i.e. $p_z \neq 0$.

In Fig. 7.3, we show the ATI spectra for photoelectrons emitted into different polar angles ϑ_p , while the azimuthal angle $\varphi_p = 0$ was held constant. The Bessel pulse has an opening angle $\vartheta_k = 20$ deg. and a TAM projection $m_\gamma = 2$, which gives rise to a significant magnitude of the $A_{p,z}$ -component. The black solid curve in Fig. 7.3 corresponds to the same detector placement (along the positive x -direction) as the black solid curve in Fig. 7.2 and serves here as a reference. All spectra in Fig. 7.3 exhibit ATI peaks similar to those computed for the plane-wave limit, since the positions of the ATI peaks are a result of the interferences due to all trigonometric

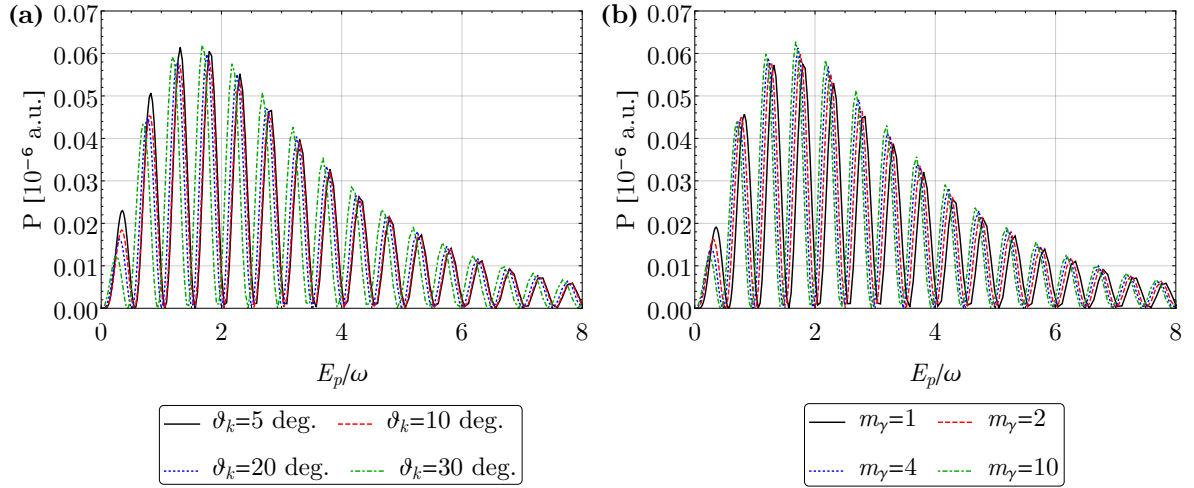


Figure 7.4: ATI spectra computed for (a) different opening angles ϑ_k with fixed TAM projection $m_\gamma = 2$ and (b) different TAM projections m_γ with fixed opening angle $\vartheta_k = 20$ deg. Results are shown for photoelectrons emitted into the polar angle $\vartheta_p = \pi/8$ and the azimuthal angle $\varphi_p = 0$. The target atom was placed at impact parameter $\mathbf{b} = (b_{\max}, \varphi_b = 0, z_b = 0)$, where b_{\max} is the radial coordinate of maximum intensity of the pulse. All other parameters are the same as in Fig. 7.2.

functions occurring in the Volkov phase (7.5). Their frequencies are determined solely by the central wavelength λ and the number of cycles n_p of the pulse and have no dependence on the other parameters of the Bessel pulse.

Most importantly, we can observe in Fig. 7.3 that the non-vanishing opening angle of the Bessel pulse results in a measurable photoionization probability in forward direction. For $\vartheta_p = \pi/3$ (red dashed curve in Fig. 7.3), one would measure about half the number of photoelectrons emitted in the $x - y$ -plane ($\vartheta_p = \pi/2$, green dot-dashed curve in Fig. 7.3). About 10 percent can still be observed under an angle of $\vartheta_p = \pi/4$ and this fraction decreases further when the detector is placed more and more towards the propagation axis. This confirms our argument based on the classical conservation of canonical momentum. Also, it is in line with previous work based on quantum-trajectory monte-carlo methods (Paufler et al., 2018a), where, however, no analysis of individual ATI peaks was possible.

Note that this observation of photoelectrons emitted with longitudinal momenta is the result of a completely different mechanism than in Chaps. 5 and 6, where nondipole interactions due to the magnetic field of the driving beam have lead to the longitudinal photoelectron momentum. For the Bessel pulse, on the other hand, the longitudinal *electric* field component gives rise to a longitudinal momentum of the photoelectron already within the dipole approximation.

Let us analyze the effect of the opening angle ϑ_k and the TAM projection m_γ of the Bessel pulse on the ATI spectra for photoelectrons with non-vanishing longitudinal momenta. In Fig. 7.4, the ATI spectra are shown for $\vartheta_k = \pi/8$. Here, the photoioniza-

tion probability is displayed on a linear scale for better visibility of the differences in the spectra. The dependence on the opening angle ϑ_k is shown for fixed TAM projection $m_\gamma = 2$ in Fig. 7.4 (a). Since the longitudinal component of the vector potential $A_z^{(P)} \sim c_0 \sim \sin \vartheta_k$ increases with the opening angle for $0 \leq \vartheta_k \leq \pi/2$, we also expect the photoionization probability measured away from the $p_x - p_y$ -plane to increase with the opening angle ϑ_k . Indeed, it can be observed in Fig. 7.4 (a) that increasing the opening angle from $\vartheta_k = 5$ deg. (black solid curve) to $\vartheta_k = 30$ deg. (green dot-dashed curve) leads to an increase of a few percent in ionization probability in the dominant part of the spectrum. This effect is more pronounced if the opening angle is further increased to $\vartheta_k = 40$ deg. (Böning et al., 2018). Also, a similar behavior is found if the TAM projection m_γ of the Bessel pulse is varied [cf. Fig. 7.4 (b)]: the number of photoelectrons emitted into $\vartheta_p = \pi/8$ is small compared to those observed perpendicular to the propagation direction of the pulse if $m_\gamma = 2$. However, the magnitude of the ATI peaks can be increased if the Bessel pulse carries a larger TAM. One would expect that the fraction of photoelectrons emitted with $p_z \neq 0$ and towards larger ϑ_p can be arbitrarily increased by changing the opening angle and, as a result, the longitudinal component $A_z^{(P)}$ of the vector potential. This possibility is limited, however, since it is experimentally difficult to generate Bessel-like beams with opening angle $\vartheta_k > 35$ deg. (Boucher et al., 2018).

Both Figs. 7.4 (a) and (b) also show another effect: an increase of the opening angle or the TAM projection leads to a constant shift of the ATI spectra towards lower energies. From a formal point of view, we can understand this shift by looking at the Volkov phase (7.5): the relative magnitudes and positions of the ATI peaks are determined by the Fourier coefficients γ_j and σ_j as well as the frequencies $\omega_j^{(c)}$ and $\omega_j^{(s)}$. A constant overall shift of the spectrum, however, results from a change in the coefficient β . In order to give this parameter a physical meaning, we write it in the form $\beta = \frac{p^2}{2} + U_p$, where U_p is the ponderomotive energy of the photoelectron in the Bessel pulse, given by (see App. B.2)

$$U_p = \frac{3}{32} A_0^2 \left(2\alpha_{-1}^2 + 2\alpha_1^2 + \alpha_0^2 \right), \quad (7.9)$$

where the coefficients α_j depend on the opening angle ϑ_k , the TAM projection m_γ and the impact parameter b .

The ponderomotive energy (7.9) is shown in Fig. 7.5 as function of ϑ_k for different values of the TAM projection. We see that it increases with the opening angle for all values of m_γ . Also, larger values of m_γ yield a higher ponderomotive energy for all ϑ_k and this difference increases with the opening angle. Thus, we conclude that for fixed intensity, both the opening angle and the TAM projection of the Bessel pulse determine U_p and accordingly lead to a constant shift in the observed ATI spectra.

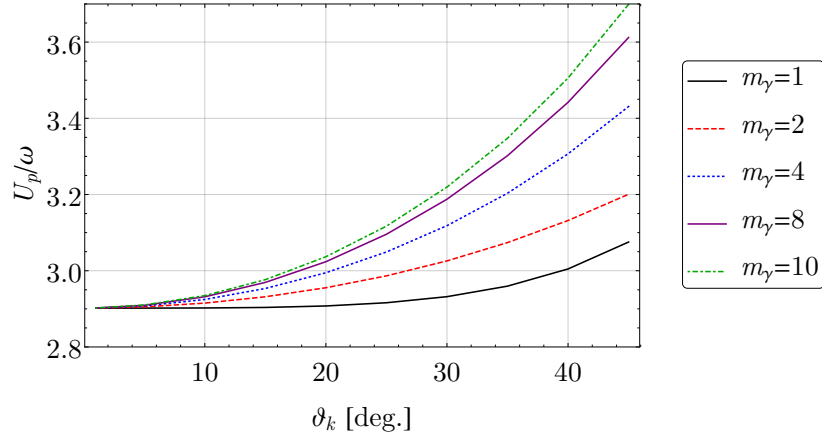


Figure 7.5: Ponderomotive energy $U_p = \beta - p^2/2$ of an electron in the Bessel pulse as function of the opening angle ϑ_k for different values of the TAM projection m_γ . All other laser parameters are the same as in Fig. 7.2.

The results presented above demonstrate that the ATI driven by few-cycle Bessel pulses leads to observable photoionization probabilities in forward direction. This forward momentum p_z of the photoelectrons is not the consequence of nondipole interactions with the Bessel pulse but is, instead, induced by a longitudinal electric field component. The ATI spectra were found to depend on both the opening angle and the TAM projection of the Bessel pulse. Although we did not examine the dependence on the helicity Λ , we note that these findings do not depend on the polarization of the Bessel pulse. Moreover, changes in the intensity or wavelength of the ionizing pulse or the ionization potential of the target should not significantly alter the process as long as the SFA is valid. In particular, the dependencies on the opening angle of the pulse and the polar emission angle do not change with intensity, since only the relative amplitudes of A_x and A_z are important for the emission direction of the photoelectron (Paufler et al., 2018a). Similarly, the effect of a different ionization potential or wavelength, respectively, is an overall shift of the ATI peaks due to energy conservation. Finally, it is a particularly important question how our results change with the size of the target when the single atom is replaced by a realistic cloud of atoms. For small mesoscopic targets, it can be expected that the dependencies on opening angle and TAM remain, while the same need not be true for large targets that extend over the intensity profile of the pulse.

7.5 TOWARDS NONDIPOLE EFFECTS

Although the results of the previous section markedly differ from the ATI with plane-wave laser pulses, they are entirely due to dipole interactions between the photoelectron and the Bessel pulse. Since the local dipole approximation that we

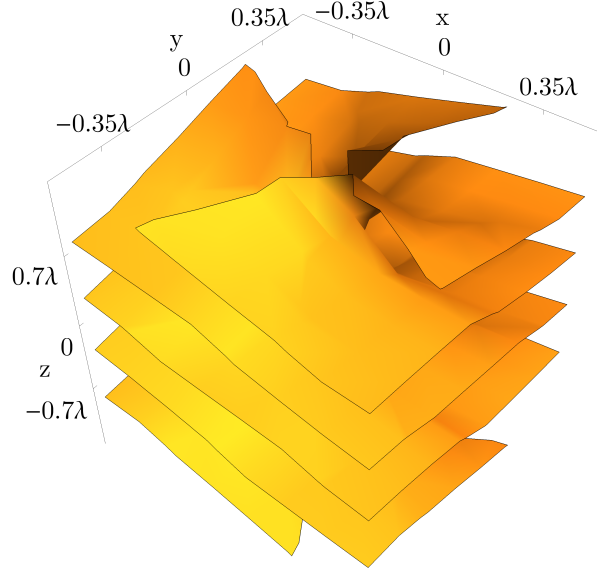


Figure 7.6: Surface of constant phase of the nondipole Volkov state (4.20) for an electron in a Bessel beam. To obtain this figure, the modified Volkov phase (4.20b) was numerically evaluated, based on analytical expressions for the functions defined in Eqs. (4.11), for a Bessel beam of the form (2.25) and with the following parameters: $\lambda = 800$ nm, $\Lambda = 1$, $m_\gamma = 2$, $\vartheta_k = 25$ deg. and $\mathbf{p} = (p_x, p_y, p_z) = (0, 0, 0.1$ a.u.). The surface $\Gamma(\mathbf{r}, t) = \text{const.}$ shows a winding structure around the beam (z -) axis of the Bessel beam, indicating a non-vanishing orbital angular momentum of the electron with respect to this axis.

made in Sec. 7.3.1 is only justified for few-cycle Bessel pulses, the extension to long Bessel pulses has to account for nondipole interactions.

Such an extension is possible in terms of the nondipole SFA for spatially structured laser fields developed in Chap. 4: in order to account for the spatial structure of a Bessel beam, we need to evaluate the functions defined in Eqs. (4.11) and the modified Volkov phase (4.20b) starting from the plane-wave expansion (2.25). Although the full analysis goes beyond this dissertation, let us have a look at the first integral in the modified Volkov phase,

$$\int d^3\mathbf{k} \rho_{\mathbf{k}} \sin(u_{\mathbf{k}} + \theta_{\mathbf{k}}) = C \int_0^{2\pi} d\varphi_k \frac{|\mathbf{p} \cdot \mathbf{e}_{\mathbf{k}\Lambda}|}{\frac{\mathbf{p} \cdot \mathbf{e}_{\mathbf{k}\Lambda}}{c} - 1} \sin\left(u_{\mathbf{k}} + \arg(\mathbf{p} \cdot \mathbf{e}_{\mathbf{k}\Lambda}) + m_\gamma\left(\varphi_k - \frac{\pi}{2}\right)\right), \quad (7.10)$$

with a constant $C = C(A_0, \vartheta_k, \omega)$ and where the integrals over k_z and the radial component k_\perp were carried out using delta functions. As a result, ϑ_k and $\mathbf{k}_\perp = \varkappa = \omega/c \sin \vartheta_k$ are fixed in the above expression.

Already this first term in the modified Volkov phase contains a quite complicated² integral over $\varphi_{\mathbf{k}}$. Without solving the integral, we can observe that the TAM projection m_{γ} appears in the modified Volkov phase. However, when numerically evaluated for specific parameters, our first calculations show that this does not lead to an azimuthal phase dependence of the nondipole Volkov states. That is, in this first approximation, these states do not carry an orbital angular momentum with respect to the z -axis. Further model calculations have been performed in order to obtain the *full* modified Volkov phase (4.20b), also including the $\mathcal{O}(a\delta_2)$ term, and a visualization for specific parameters is shown in Fig. 7.6. Here, a singular structure can be observed in the surfaces of constant phase, indicating a transfer of orbital angular momentum from the Bessel beam to the photoelectron.

Of course, such preliminary calculations only serve as a first illustration and further work is needed, especially since the integrands in the double integrals over \mathbf{k} and \mathbf{k}' in (4.20b) are not easy to handle. A future investigation of the precise structure of the modified Volkov phase for a Bessel driving beam promises interesting physical insight into the interaction of twisted light with electrons, particularly in the context of ATI and HHG experiments. First steps in in this direction could extend the considerations of this chapter towards long pulses and including nondipole interactions.

² Note that $\mathbf{e}_{\mathbf{k}\wedge}$ as defined in Eq. (2.16) also depends on $\varphi_{\mathbf{k}}$.

CONCLUSIONS AND OUTLOOK

In this dissertation, we have investigated ATI processes driven by spatially structured laser fields within the widely used SFA. Our approach is based on a nondipole formulation of the SFA and we have demonstrated that it successfully explains different experimental findings. In the following, we will briefly summarize the key findings from each chapter and will discuss possible future work in different directions.

We started with an overview of the description of light in Chap. 2. There, we introduced Maxwell's equations and discussed the relevance of the spatial structure of light beams. As particular solutions to Maxwell's equations, we presented plane-wave beams and pulses, which provide a model of standard laser beams used in experiments. We then turned to so-called Bessel beams that are a particular example of twisted light beams. Such beams have helical phase fronts due to their orbital angular momentum with respect to the beam axis. As a result, their vector potential, their electric and magnetic fields, as well as their intensity profile have a pronounced spatial dependence. Due to their orbital angular momentum, twisted beams are an attractive tool in laser-atom interactions and they have been applied in various scenarios in both the perturbative and strong-field regimes.

In Chap. 3, we reviewed the theoretical description of ATI in the framework of the SFA. This analytical approach allows the calculation of photoionization probabilities in laser fields with high intensity and is based on the assumption that the atomic binding potential can be neglected in the photoelectron dynamics in the continuum. Within the dipole approximation, i.e. if the spatial dependence of the laser field is neglected, the continuum states available to the electron are then given by so-called Volkov states. One can obtain these states as solutions to the Schrödinger equation for an electron in the (purely) time-dependent laser field. We applied the SFA in dipole approximation to the ATI of atoms driven by plane-wave laser pulses and showed that the characteristic ATI spectra can be computed. However, within the dipole SFA, effects related to the photon momentum or the spatial structure of the driving laser field cannot be described.

Chapter 4 therefore introduced our theoretical approach to ATI processes driven by spatially structured laser beams. We extended the SFA towards *nondipole* interactions between the photoelectron and the driving laser beam. To this end, we constructed nondipole Volkov states as solutions to the Schrödinger equation with a quite general ansatz for the spatial dependence of the beam's vector potential. This ansatz allows, for example, to also take Gaussian or twisted light beams into consideration. We discussed that the derived nondipole Volkov states are not exact solutions to the Schrödinger equation but can be considered exact as long as relativistic contributions of the order $(v/c)^2$ are small. Moreover, we showed that the nondipole Volkov states can be expressed in a form very similar to the dipole Volkov states with a *modified* Volkov phase. Finally, we discussed the relation to other nondipole SFA theories. In contrast to these, our nondipole SFA approach allows not only the treatment of plane-wave beams or discrete superpositions of them but can also account for an *arbitrary* spatial structure of the laser beam.

Besides specific applications, future work should be directed towards the examination of the mathematical foundation of this nondipole SFA and its physical interpretation. In particular, its relation to the relativistic SFA for single-mode (Krajewska and Kaminski, 2015) and multi-mode (Wolkow, 1935) laser fields as well as to a Coulomb-corrected nondipole SFA (Titi and Drake, 2012) should be worked out in more detail. Moreover, the gauge dependence of the nondipole SFA should be addressed [cf. Sec. 3.3.2] and the physical meaning of the rescattering term in the SFA transition amplitude [cf. Eq. (3.16)] should be clarified for the case that the continuum is described by nondipole Volkov states.

In Chap. 5, we turned to the application of the nondipole SFA to the ATI driven by plane-wave laser beams. At long laser wavelengths (mid-IR), the dipole approximation is not sufficient to describe the photoelectron dynamics in the beam's electric and magnetic fields. Most importantly, the Lorentz force induces a motion along the beam axis. In ATI experiments, the result of this motion can be seen in the PEMDs, which are shifted towards nonzero p_z . In the particle picture, this *peak shift* can also be interpreted as a momentum transfer from the photons to the photoelectron. We demonstrated how these peak shifts can be computed for different laser wavelengths and atomic targets within the nondipole SFA developed in Chap. 4. To this end, we explicitly evaluated the nondipole Volkov states and showed that the resulting expressions agree with previous nondipole SFA approaches.

Furthermore, for circular polarization, the computed peak shifts are in good agreement with available experimental data: they lie in the order of 10^{-2} a.u. and, as expected from the scaling of the classical motion due to nondipole effects, increase linearly with the laser intensity. However, small discrepancies remain between the

theoretical and the experimental values, due to the neglect of a realistic temporal and spatial structure of the driving laser pulse. For linear polarization, on the other hand, the experimental peak shifts are negative, while our theoretical values are consistently positive. This can be attributed to our neglect of Coulomb interactions in the continuum and any rescattering of the photoelectron with the parent ion during which the longitudinal photoelectron momentum is essentially reversed.

Future improvements can extend this work in several ways. For one thing, rescattering contributions should be included in the calculation of peak shifts. It would then be possible to compute the ellipticity dependence of the peak shifts, which was measured by Daněk et al. (2018a). From comparisons with theory, one might gain insight into the rescattering process when nondipole interactions become important, which goes well together with the abovementioned theoretical questions regarding the nondipole SFA. Moreover, in order to remove the quantitative discrepancies between our theoretical and experimental peak shifts, the nondipole SFA should be applied to the ATI with Gaussian laser beams. Since the nondipole SFA developed in Chap. 4 can account for their beam profile [cf. Eq. (5.18)] in the nondipole Volkov states, it allows a full quantum description of the focal averaging that had to be manually included in previous studies (Smeenk et al., 2011; Titi and Drake, 2012).

As a second application of the nondipole SFA, we examined the so-called *high-intensity KDE*, i.e. the ATI of atomic targets driven by a standing light wave of high intensity, in Chap. 6. The ponderomotive force acting on an electron in the combined electric and magnetic fields of a standing light wave leads to a momentum transfer to the electron along the beam axis. While the peak shifts in the ATI with plane-wave beams correspond to a few photon momenta, the momentum transfer in the high-intensity KDE can be in the order of 1000 photon momenta.

We demonstrated how the nondipole SFA of Chap. 4 can be applied to this scenario. To this end, we evaluated the nondipole Volkov states for an electron in a standing light wave and computed PADs of the emitted photoelectrons from which the momentum transfer can be extracted. We found that the theory agrees with a previous experiment for photoelectrons with high energy compared to the ponderomotive energy of the standing wave. For low-energy photoelectrons, on the other hand, we found that the momentum transfer can be much larger and that they show a diffraction-like behavior similar to the free-electron KDE. Furthermore, the nondipole SFA predicts a strong dependence of the momentum transfer on the ellipticity of the standing light wave.

Future theoretical work on the high-intensity KDE can proceed along different lines. First, the nondipole SFA description may be applied to a wider parameter regime and the dependence of the momentum transfer on the ellipticity of the standing wave may

be studied in more detail. As already mentioned above, rescattering contributions should be accounted for and, additionally, Coulomb effects should be included in the continuum for low-energy photoelectrons to obtain reliable results. As a complement to the SFA description, the photoelectron dynamics in a standing light wave may be simulated based on quantum-trajectory monte carlo methods. We expect that this will provide further insight into the role of the ellipticity-dependent ponderomotive force (Smorenburg et al., 2011).

In addition, a promising scenario is the ATI driven by two *crossed* plane-wave laser beams, which are not counter-propagating as in the case of a standing light wave, but which have beam axes that differ by a small angle. The combined field of the two laser beams has a pronounced impact on the electron dynamics in the continuum (Salamin et al., 2003) and, for the HHG driven by mid-IR beams, such a setup allows the control of the recombination between photoelectron and parent ion (Pisanty et al., 2018). Since the nondipole Volkov states of Chap. 4 can be readily evaluated for such a setup, it shall be interesting to investigate the possibility of using the crossing angle between the beams to control the ionization process.

In Chap. 7, we discussed the ATI of atoms driven by few-cycle Bessel pulses. We showed that the spatial structure of the pulse that is due to its orbital angular momentum can be neglected in the description of ATI experiments if the pulse duration is sufficiently short. In this case, a local dipole approximation can be made in which the vector potential is approximated at the position of the target atom. Already within this approximation and based on the dipole SFA, the ATI spectra are fundamentally different from those obtained for plane-wave driving pulses: due to a longitudinal component of the electric field, the photoelectrons are emitted with a high probability with a momentum component along the beam axis. We found that the ATI spectra computed along different polar emission angles depend on both the TAM of the Bessel pulse and its opening angle, which determines the magnitude of the field's z -component.

While it is possible to localize single atoms very precisely (Schmiegelow et al., 2016), atomic targets of a finite size should be considered in the future to properly describe experimental scenarios. As long as the target remains sufficiently small with respect to the spatial variations of the Bessel beam, we expect that the dependencies on opening angle and TAM remain. However, the situation might change if a macroscopic gas target is used that extends over the intensity profile of the Bessel pulse.

At the end of Chap. 7, we briefly discussed the extension of this work towards long Bessel pulses and continuous Bessel beams. While the Bessel beam's spatial structure cannot be accounted for in other SFA theories, the nondipole SFA for spatially structured laser fields developed in Chap. 4 readily allows its incorporation into the

photoelectron continuum. We briefly examined the nondipole Volkov states derived in Chap. 4 and presented a first numerical calculation. Their phase fronts exhibit a singularity on the beam axis and have a helical structure, which indicates that the photoelectron described by the nondipole Volkov state carries an orbital angular momentum with respect to the beam axis.

It will be a promising future task to extend these preliminary considerations. In particular, the transfer of orbital angular momentum from the twisted beam to the photoelectron and its impact on ATI spectra may be considered. In this way, the nondipole SFA for spatially structured laser fields will provide insights into the role of the photon's linear and orbital angular momentum in strong-field laser-atom interactions.

A

BESSEL FUNCTIONS OF THE FIRST KIND

The Bessel functions of the first kind $J_n(x)$ with integer n are solutions to the Bessel differential equation

$$x^2 \frac{d^2 y}{dx^2} + x \frac{dy}{dx} + (x^2 - n^2)y = 0, \quad (\text{A.1})$$

and can be written in the integral representation

$$J_n(x) = \frac{1}{\pi} \int_{-\pi}^{\pi} d\tau e^{i(x \sin \tau - n\tau)}. \quad (\text{A.2})$$

In particular, they fulfill the identity $J_n(-x) = J_{-n}(x) = -J_n(x)$ and behave like $J_n(x) \sim e^{-n}$ for $n > x$. A useful formula involving the Bessel functions of the first kind is the Jacobi-Anger expansion of exponentials of trigonometric functions (Abramowitz and Stegun, 1972),

$$e^{iz \sin \theta} = \sum_{n=-\infty}^{\infty} J_n(z) e^{in\theta}, \quad (\text{A.3})$$

or, equivalently,

$$e^{iz \cos \theta} = \sum_{n=-\infty}^{\infty} i^n J_n(z) e^{in\theta}. \quad (\text{A.4})$$

Generalizations of the Bessel functions of the first kind to non-integer n exist but are not relevant for this dissertation.

B

DIPOLE VOLKOV STATES: DERIVATIONS

In this appendix, we explicitly derive the dipole Volkov phase $S_V(t)$, defined in Eq. (3.25), for plane-wave laser beams and pulses, as well as Bessel pulses. The resulting dipole Volkov states are used in Sec. 3.4 and Chap. 7, respectively.

B.1 PLANE-WAVE LASER PULSE

In order to evaluate the dipole Volkov phase in Eq. (3.25), we rewrite the vector potential (3.35) in the form (Milošević et al., 2006)

$$\mathbf{A}(t) = \sum_{j=1}^2 \varepsilon_j \mathbf{e}_j \sum_{i=0}^2 \mathcal{A}_i \cos \varphi_{ij}, \quad (\text{B.1})$$

where we introduced $\varphi_{ij} = \omega_i t + \phi_j$ and the short notation

$$\varepsilon_1 = \frac{\varepsilon_2}{\varepsilon} = \frac{1}{\sqrt{1 + \varepsilon^2}}, \quad \mathcal{A}_0 = 2\mathcal{A}_1 = 2\mathcal{A}_2 = \frac{A_0}{2}, \quad (\text{B.2a})$$

$$\omega_0 = \omega, \quad \omega_{1,2} = \frac{n_p \pm 1}{n_p} \omega, \quad \phi_1 = \phi_{\text{CEP}} + \frac{\pi}{2}, \quad \phi_2 = \phi_{\text{CEP}}. \quad (\text{B.2b})$$

With these definitions, the dipole Volkov phase can be expressed in a compact form and the integrals can be carried out.

Explicitly, we find:

$$\begin{aligned}
S_V(t) &= \frac{1}{2} \int^t dt' \left(p^2 + 2p_x A_x(t') + 2p_y A_y(t') + \mathbf{A}^2(t') \right) \\
&= \frac{p^2}{2} t + \sum_{j=1}^2 \varepsilon_j p_j \sum_{i=0}^2 \mathcal{A}_i \int^t dt' \cos \varphi_{ij} + \frac{1}{2} \sum_{j=1}^2 \varepsilon_j^2 \sum_{i,k=0}^2 \mathcal{A}_i \mathcal{A}_k \int^t dt' \cos \varphi_{ij} \cos \varphi_{kj} \\
&= \underbrace{\frac{1}{2} \sum_{j=1}^2 \varepsilon_j^2 \sum_{i=0}^2 \frac{\mathcal{A}_i^2 \phi_j}{2\omega_i}}_{C=\text{const.}} + \left[\frac{p^2}{2} + \frac{1}{4} \sum_{j=1}^2 \varepsilon_j^2 \sum_{i=0}^2 \mathcal{A}_i^2 \right] t + \sum_{j=1}^2 \varepsilon_j p_j \sum_{i=0}^2 \frac{\mathcal{A}_i}{\omega_i} \sin(\omega_i t + \phi_j) \\
&\quad + \frac{1}{2} \sum_{j=1}^2 \varepsilon_j^2 \sum_{i=0}^2 \sum_{k=0, k \neq i}^2 \mathcal{A}_i \mathcal{A}_k \left(\frac{\sin((\omega_i - \omega_k)t)}{2(\omega_i - \omega_k)} \right. \\
&\quad \quad \left. + \frac{\sin(2\phi_j + (\omega_i + \omega_k)t)}{2(\omega_i + \omega_k)} + \frac{\sin(2\phi_j + 2\omega_i t)}{4\omega_i} \delta_{ik} \right). \quad (\text{B.3})
\end{aligned}$$

More compactly, we may write

$$S_V(t) = \beta t + \sum_{r=1}^3 \gamma_r \cos(\omega_r^{(c)} t + \phi_{\text{CEP}}) + \sum_{s=1}^{10} \sigma_s \sin(\omega_s^{(s)} t + \phi_s^{(s)}), \quad (\text{B.4})$$

where we dropped the constant phase factor C since it does not modify ionization probabilities. The remaining coefficients and frequencies in Eq. (B.4) can be read off:

$$\beta = \frac{p^2}{2} + \frac{1}{4} \sum_{j=1}^2 \varepsilon_j^2 \sum_{i=0}^2 \mathcal{A}_i^2 = \frac{p^2}{2} + \mathcal{U}_p, \quad (\text{B.5a})$$

$$\boldsymbol{\omega}^{(c)} = (\omega_0, \omega_1, \omega_2) = \left(\omega, \omega \frac{n_p + 1}{n_p}, \omega \frac{n_p - 1}{n_p} \right), \quad (\text{B.5b})$$

$$\gamma_r = \frac{p_x}{\sqrt{1 + \varepsilon^2}} \frac{\mathcal{A}_{r-1}}{\omega_{r-1}} \quad (r = 1, 2, 3), \quad (\text{B.5c})$$

$$\boldsymbol{\omega}^{(s)} = \left(\omega_0, \omega_1, \omega_2, \frac{\omega}{n_p}, \frac{2\omega}{n_p}, \omega_1 + \omega, \omega_2 + \omega, 2\omega_0, 2\omega_1, 2\omega_2 \right), \quad (\text{B.5d})$$

$$\begin{aligned}
\boldsymbol{\sigma} &= \left(\frac{p_y \varepsilon}{\sqrt{1 + \varepsilon^2}} \frac{\mathcal{A}_0}{\omega_0}, \frac{p_y \varepsilon}{\sqrt{1 + \varepsilon^2}} \frac{\mathcal{A}_1}{\omega_1}, \frac{p_y \varepsilon}{\sqrt{1 + \varepsilon^2}} \frac{\mathcal{A}_2}{\omega_2}, (\mathcal{A}_1 + \mathcal{A}_2) \mathcal{A}_0 \frac{n_p}{2\omega}, \right. \\
&\quad \mathcal{A}_2 \mathcal{A}_1 \frac{n_p}{4\omega}, \frac{\varepsilon_2^2 - \varepsilon_1^2}{2(\omega_1 + \omega)} \mathcal{A}_1 \mathcal{A}_0, \frac{\varepsilon_2^2 - \varepsilon_1^2}{2(\omega_2 + \omega)} \mathcal{A}_2 \mathcal{A}_0, \\
&\quad \left. \frac{(\varepsilon_2^2 - \varepsilon_1^2) \mathcal{A}_0^2}{8\omega} + \frac{\varepsilon_2^2 - \varepsilon_1^2}{2(\omega_0 + \omega)} \mathcal{A}_2 \mathcal{A}_1, \frac{(\varepsilon_2^2 - \varepsilon_1^2) \mathcal{A}_1^2}{8\omega_1}, \frac{(\varepsilon_2^2 - \varepsilon_1^2) \mathcal{A}_2^2}{8\omega_2} \right), \quad (\text{B.5e})
\end{aligned}$$

$$\boldsymbol{\phi}_s = (\phi_{\text{CEP}}, \phi_{\text{CEP}}, \phi_{\text{CEP}}, 0, 0, 2\phi_{\text{CEP}}, 2\phi_{\text{CEP}}, 2\phi_{\text{CEP}}, 2\phi_{\text{CEP}}, 2\phi_{\text{CEP}}). \quad (\text{B.5f})$$

Although the Volkov phase in the above form is quite general, it is useful for specific calculations to obtain special cases. In particular, in Sec. 3.4 we consider circularly polarized ($\varepsilon = 1$) pulses, for which Eq. (B.4) reduces to

$$\begin{aligned}
 S_V(t) &= (E_p + U_p)t \\
 &+ \frac{A_0 p_x}{2\sqrt{2}\omega} \left[\cos(\omega t + \phi_{\text{CEP}}) + \frac{1}{2} \frac{n_p}{n_p + 1} \cos\left(\frac{n_p + 1}{n_p} \omega t + \phi_{\text{CEP}}\right) \right. \\
 &\quad \left. + \frac{1}{2} \frac{n_p}{n_p - 1} \cos\left(\frac{n_p - 1}{n_p} \omega t + \phi_{\text{CEP}}\right) \right] \\
 &+ \frac{A_0 p_y}{2\sqrt{2}\omega} \left[\sin(\omega t + \phi_{\text{CEP}}) + \frac{1}{2} \frac{n_p}{n_p + 1} \sin\left(\frac{n_p + 1}{n_p} \omega t + \phi_{\text{CEP}}\right) \right. \\
 &\quad \left. + \frac{1}{2} \frac{n_p}{n_p - 1} \sin\left(\frac{n_p - 1}{n_p} \omega t + \phi_{\text{CEP}}\right) \right] \\
 &+ U_p \frac{n_p}{2\omega} \sin\left(\frac{\omega}{n_p} t\right) + \frac{U_p}{4} \frac{n_p}{4\omega} \sin\left(\frac{2\omega}{n_p} t\right). \tag{B.6}
 \end{aligned}$$

In Sec. 5.3.1, we compare nondipole Volkov states for a continuous laser beam with the corresponding dipole Volkov states. Since it is not possible to take the limit $n_p \rightarrow \infty$ in the above expressions ($\mathbf{A}(t) \rightarrow 0$), we start from the vector potential

$$\mathbf{A}(\mathbf{r}, t) = \frac{A_0}{\sqrt{1 + \varepsilon^2}} (\cos(\omega t) \mathbf{e}_x + \varepsilon \Lambda \sin(\omega t) \mathbf{e}_y), \tag{B.7}$$

and derive the Volkov phase beginning with its definition:

$$\begin{aligned}
 S_V(t) &= \frac{1}{2} \int^t dt' \left(p^2 + \frac{2p_x A_0}{\sqrt{1 + \varepsilon^2}} \cos(\omega t') + \varepsilon \Lambda \frac{2p_y A_0}{\sqrt{1 + \varepsilon^2}} \sin(\omega t') \right. \\
 &\quad \left. + \frac{A_0^2}{1 + \varepsilon^2} \cos^2(\omega t') + \varepsilon^2 \frac{A_0^2}{1 + \varepsilon^2} \sin^2(\omega t') \right) \\
 &= \frac{p^2}{2} t + \frac{p_x A_0}{\omega \sqrt{1 + \varepsilon^2}} \sin(\omega t) - \varepsilon \Lambda \frac{p_y A_0}{\omega \sqrt{1 + \varepsilon^2}} \cos(\omega t) \\
 &\quad + \frac{A_0^2}{2(1 + \varepsilon^2)} \left(\frac{t}{2} + \frac{\sin(2\omega t)}{4\omega} \right) + \varepsilon^2 \frac{A_0^2}{2(1 + \varepsilon^2)} \left(\frac{t}{2} - \frac{\sin(2\omega t)}{4\omega} \right) \\
 &= \frac{p^2}{2} t + \frac{p_x A_0}{\omega \sqrt{1 + \varepsilon^2}} \sin(\omega t) - \varepsilon \Lambda \frac{p_y A_0}{\omega \sqrt{1 + \varepsilon^2}} \cos(\omega t) + \frac{A_0^2}{4} t \\
 &\quad + \frac{A_0^2}{8\omega} \frac{1 - \varepsilon^2}{1 + \varepsilon^2} \sin(2\omega t). \tag{B.8}
 \end{aligned}$$

In order to cast this result in a slightly different form, let us define the vector

$$\tilde{\mathbf{p}} = (p_x, \varepsilon p_y, p_z) = \tilde{p} (\sin \tilde{\vartheta}_p \cos \tilde{\varphi}_p, \sin \tilde{\vartheta}_p \sin \tilde{\varphi}_p, \cos \tilde{\vartheta}_p). \tag{B.9}$$

It then follows that

$$\begin{aligned} p_x \sin(\omega t) - \varepsilon \Lambda p_y \cos(\omega t) &= \tilde{p} \sin \tilde{\vartheta}_p (\cos \tilde{\varphi}_p \sin(\omega t) - \Lambda \sin \tilde{\varphi}_p \cos(\omega t)) \\ &= \tilde{p} \sin \tilde{\vartheta}_p \sin(\omega t - \Lambda \tilde{\varphi}_p), \end{aligned} \quad (\text{B.10})$$

where we used the fact that $\Lambda = \pm 1$. If we rewrite the azimuthal angle,

$$\tilde{\varphi}_p = \arctan\left(\frac{\tilde{p}_y}{\tilde{p}_x}\right) = \arctan(\varepsilon \tan \varphi_p), \quad (\text{B.11})$$

with $\tan \varphi_p = p_y/p_x$, and define $\varphi_p^{(\varepsilon)} = \tilde{\varphi}_p$, we arrive at

$$S_V(t) = E_p t + U_p t + \frac{A_0}{\omega} \frac{\sqrt{p_x^2 + \varepsilon^2 p_y^2}}{\sqrt{1 + \varepsilon^2}} \sin(\omega t - \varphi_p^{(\varepsilon)}) + \frac{A_0^2}{8\omega} \frac{1 - \varepsilon^2}{1 + \varepsilon^2} \sin(2\omega t). \quad (\text{B.12})$$

Here, we have also inserted $E_p = p^2/2$, $U_p = A_0^2/4$ and $\tilde{p} = |\tilde{\mathbf{p}}| = \sqrt{p_x^2 + \varepsilon^2 p_y^2}$.

B.2 BESSEL PULSE

For the Bessel pulse vector potential $\mathbf{A}_p(\mathbf{r}, t)$, given by Eq. (7.1) with the continuous Bessel beam (2.32), and for $\mathbf{r} = \mathbf{b} = \text{const.}$, the dipole Volkov phase $S_{V,b}(t)$ in Eq. (7.4) can be evaluated by performing a Fourier decomposition of the integrand and then integrating the resulting sum of harmonic terms. This yields

$$S_{V,b}(t) = \beta t + \sum_{j=1}^9 \gamma_j \cos(\varphi_j^{(c)} - \omega_j^{(c)} t) + \sum_{l=1}^{13} \sigma_l \sin(\varphi_l^{(s)} - \omega_l^{(s)} t), \quad (\text{B.13})$$

as stated in Eq. (7.5). The frequencies and phases are explicitly given by

$$\boldsymbol{\omega}^{(c)} = \omega \times \left(1, 1, 1, \frac{n_p - 1}{n_p}, \frac{n_p - 1}{n_p}, \frac{n_p - 1}{n_p}, \frac{n_p + 1}{n_p}, \frac{n_p + 1}{n_p}, \frac{n_p + 1}{n_p}\right), \quad (\text{B.14a})$$

$$\begin{aligned} \boldsymbol{\omega}^{(s)} = \omega \times \left(-\frac{1}{n_p}, -\frac{2}{n_p}, 1, 2, 1, \frac{2n_p - 1}{n_p}, \frac{n_p - 1}{n_p}, 2\frac{n_p - 1}{n_p}, \frac{n_p - 1}{n_p}, 2\frac{n_p + 1}{n_p}, \right. \\ \left. \frac{n_p + 1}{n_p}, \frac{n_p + 1}{n_p}, \frac{2n_p + 1}{n_p} \right), \end{aligned} \quad (\text{B.14b})$$

$$\boldsymbol{\varphi}^{(c)} = \varphi_b \times (m_\gamma - 1, m_\gamma, m_\gamma + 1, m_\gamma - 1, m_\gamma, m_\gamma + 1, m_\gamma - 1, m_\gamma, m_\gamma + 1), \quad (\text{B.14c})$$

$$\begin{aligned} \boldsymbol{\varphi}^{(s)} = \varphi_b \times (0, 0, m_\gamma - 1, 2m_\gamma, m_\gamma + 1, 2m_\gamma, m_\gamma - 1, 2m_\gamma, m_\gamma + 1, \\ 2m_\gamma, m_\gamma - 1, m_\gamma + 1, 2m_\gamma), \end{aligned} \quad (\text{B.14d})$$

and the Fourier coefficients in $S_{V,\mathbf{b}}(t)$ are

$$\beta = \frac{p^2}{2} + \frac{3}{32}A_0^2 \left(2\alpha_{-1}^2 + 2\alpha_1^2 + \alpha_0^2 \right), \quad (\text{B.15})$$

$$\boldsymbol{\gamma} = \frac{A_0}{2\omega} \left(-p_y\alpha_1, p_z\alpha_0, p_y\alpha_{-1}, \frac{n_p p_y \alpha_1}{2(n_p - 1)'}, -\frac{n_p p_z \alpha_0}{2(n_p - 1)'}, -\frac{n_p p_y \alpha_{-1}}{2(n_p - 1)'}, \right. \\ \left. \frac{n_p p_y \alpha_1}{2(n_p + 1)'}, -\frac{n_p p_z \alpha_0}{2(n_p + 1)'}, -\frac{n_p p_y \alpha_{-1}}{2(n_p + 1)'} \right), \quad (\text{B.16})$$

$$\boldsymbol{\sigma} = \frac{A_0}{2\omega} \left(-\frac{A_0 n_p}{4} \left(2\alpha_1^2 + 2\alpha_{-1}^2 + \alpha_0^2 \right), \frac{A_0 n_p}{32} \left(2\alpha_1^2 + 2\alpha_{-1}^2 + \alpha_0^2 \right), -p_x \alpha_1, \right. \\ \frac{3A_0}{32} \left(\alpha_0^2 - 4\alpha_{-1}\alpha_1 \right), -p_x \alpha_{-1}, \frac{A_0 n_p}{8(2n_p - 1)} \left(4\alpha_{-1}\alpha_1 - \alpha_0^2 \right), \frac{n_p p_x \alpha_1}{2(n_p - 1)'}, \\ \frac{A_0 n_p}{64(n_p - 1)} \left(\alpha_0^2 - 4\alpha_{-1}\alpha_1 \right), \frac{n_p p_x \alpha_{-1}}{2(n_p - 1)'}, \frac{A_0 n_p}{64(n_p + 1)} \left(\alpha_0^2 - 4\alpha_{-1}\alpha_1 \right), \\ \left. \frac{n_p p_x \alpha_1}{2(n_p + 1)'}, \frac{n_p p_x \alpha_{-1}}{2(n_p + 1)'}, \frac{A_0 n_p}{8(2n_p + 1)} \left(4\alpha_{-1}\alpha_1 - \alpha_0^2 \right) \right). \quad (\text{B.17})$$

The factors α_j ($j = 0, \pm 1$) encode the dependence of the Bessel pulse on the impact parameter \mathbf{b} and are defined as

$$\alpha_{-1} = \frac{1}{\sqrt{2}} \sqrt{\frac{\varkappa}{2\pi}} c_{-1} J_{m_\gamma+1}(\varkappa \mathbf{b}), \quad (\text{B.18a})$$

$$\alpha_0 = \sqrt{\frac{\varkappa}{2\pi}} c_0 J_{m_\gamma}(\varkappa \mathbf{b}), \quad (\text{B.18b})$$

$$\alpha_1 = \frac{1}{\sqrt{2}} \sqrt{\frac{\varkappa}{2\pi}} c_1 J_{m_\gamma-1}(\varkappa \mathbf{b}), \quad (\text{B.18c})$$

with $c_{0,\pm 1}$ given below Eq. (2.20).

ZEROth-ORDER APPROXIMATION IN THE NONDIPOLE SFA

Here, we prove by insertion that the functional $f^{(0)}$, given by Eqs. (4.13) with the definitions (4.11) is a solution to the functional integro-differential equation (4.12), which is equivalent to the Schrödinger equation with the second derivatives and the term proportional to $\mathbf{A}(\mathbf{r}, t) \cdot \nabla f^{(0)}$ neglected.

We start with the left hand side of Eq. (4.11):

$$\begin{aligned}
& i \int d^3 \mathbf{k}' \eta_{\mathbf{k}'} \frac{\delta f^{(0)}[\mathbf{u}_{\mathbf{k}}]}{\delta \mathbf{u}_{\mathbf{k}'}} \\
&= f^{(0)}[\mathbf{u}_{\mathbf{k}}] \int d^3 \mathbf{k}' \eta_{\mathbf{k}'} \frac{\delta \Gamma^{(0)}[\mathbf{u}_{\mathbf{k}}]}{\delta \mathbf{u}_{\mathbf{k}'}} \\
&= f^{(0)}[\mathbf{u}_{\mathbf{k}}] \int d^3 \mathbf{k}' \int d^3 \tilde{\mathbf{k}} \eta_{\mathbf{k}} \rho_{\mathbf{k}'} \cos(u_{\tilde{\mathbf{k}}} + \theta_{\mathbf{k}'}) \delta(\mathbf{k}' - \tilde{\mathbf{k}}) \\
&\quad + f^{(0)}[\mathbf{u}_{\mathbf{k}}] \int d^3 \mathbf{k}' \int d^3 \tilde{\mathbf{k}} \int d^3 \mathbf{k}'' \eta_{\mathbf{k}} \left(\alpha_{\tilde{\mathbf{k}}\mathbf{k}''}^+ \cos(u_{\tilde{\mathbf{k}}} + u_{\mathbf{k}''} + \theta_{\tilde{\mathbf{k}}\mathbf{k}''}^+) \delta(\tilde{\mathbf{k}} - \mathbf{k}') \right. \\
&\quad \quad \quad \left. + \alpha_{\tilde{\mathbf{k}}\mathbf{k}''}^+ \cos(u_{\tilde{\mathbf{k}}} + u_{\mathbf{k}''} + \theta_{\tilde{\mathbf{k}}\mathbf{k}''}^+) \delta(\mathbf{k}'' - \mathbf{k}') \right. \\
&\quad \quad \quad \left. + \alpha_{\tilde{\mathbf{k}}\mathbf{k}''}^- \cos(u_{\tilde{\mathbf{k}}} - u_{\mathbf{k}''} + \theta_{\tilde{\mathbf{k}}\mathbf{k}''}^-) \delta(\tilde{\mathbf{k}} - \mathbf{k}') \right. \\
&\quad \quad \quad \left. - \alpha_{\tilde{\mathbf{k}}\mathbf{k}''}^- \cos(u_{\tilde{\mathbf{k}}} - u_{\mathbf{k}''} + \theta_{\tilde{\mathbf{k}}\mathbf{k}''}^-) \delta(\mathbf{k}'' - \mathbf{k}') \right) \\
&= f^{(0)}[\mathbf{u}_{\mathbf{k}}] \int d^3 \tilde{\mathbf{k}} \lambda_{\tilde{\mathbf{k}}} \cos(u_{\tilde{\mathbf{k}}} + \theta_{\tilde{\mathbf{k}}}) \\
&\quad + f^{(0)}[\mathbf{u}_{\mathbf{k}}] \int d^3 \tilde{\mathbf{k}} \int d^3 \mathbf{k}'' \left(\Delta_{\tilde{\mathbf{k}}\mathbf{k}''}^+ \cos(u_{\tilde{\mathbf{k}}} + u_{\mathbf{k}''} + \theta_{\tilde{\mathbf{k}}\mathbf{k}''}^+) \right. \\
&\quad \quad \quad \left. + \Delta_{\tilde{\mathbf{k}}\mathbf{k}''}^- \cos(u_{\tilde{\mathbf{k}}} - u_{\mathbf{k}''} + \theta_{\tilde{\mathbf{k}}\mathbf{k}''}^-) \right). \tag{C.1}
\end{aligned}$$

In the last step, we have carried out the \mathbf{k}' integrals using the delta functions and the definition of the $\alpha_{\tilde{\mathbf{k}}\mathbf{k}'}^\pm$ [Eq. (4.11f)]. The last line above is identical to the right hand side of Eq. (4.13b) after renaming the integration variables, which proves that Eq. (4.13) is indeed a solution.

In the same manner, it can be shown that the functional g as given by Eq. (4.15) solves the functional integro-differential equation (4.14).

D

NONDIPOLE VOLKOV STATES: DERIVATIONS

In this appendix, we explicitly go through the evaluation of the functions defined in Eqs. (4.11) that determine the modified Volkov phase (4.20b) and are used in the main text in Chaps. 5 and 6.

D.1 PLANE-WAVE LASER BEAM

We begin with the plane-wave driving beam with the vector potential (5.4) and show that Eqs. (4.11) lead to Eqs. (5.5) in this case.

1. $\lambda_{\mathbf{k}}$, $\theta_{\mathbf{k}}$ and $\rho_{\mathbf{k}}$:

We insert the vector potential into Eq. (4.11a) and obtain

$$\begin{aligned} \lambda_{\mathbf{k}} \cos(u_{\mathbf{k}} + \theta_{\mathbf{k}}) &= \mathbf{p} \cdot \mathbf{A}(\mathbf{k}, t) \\ &= \frac{A_0}{\sqrt{1 + \varepsilon^2}} \delta(\mathbf{k} - \mathbf{k}_0) \operatorname{Re} \left\{ \mathbf{p} \cdot (\mathbf{e}_x + i\varepsilon \mathbf{e}_y) e^{iu_{\mathbf{k}}} \right\}. \end{aligned} \quad (\text{D.1})$$

With the definition (B.9) of the vector $\tilde{\mathbf{p}}$, we can write

$$\mathbf{p} \cdot (\mathbf{e}_x + i\varepsilon \mathbf{e}_y) = \tilde{p} \sin \tilde{\vartheta}_p (\cos \tilde{\varphi}_p + i \sin \tilde{\varphi}_p) \quad (\text{D.2})$$

and therefore

$$\begin{aligned} \operatorname{Re} \left\{ \mathbf{p} \cdot (\mathbf{e}_x + i\varepsilon \mathbf{e}_y) e^{iu_{\mathbf{k}}} \right\} &= \tilde{p} \sin \tilde{\vartheta}_p (\cos \tilde{\varphi}_p \cos u_{\mathbf{k}} - \sin \tilde{\varphi}_p \sin u_{\mathbf{k}}) \\ &= \tilde{p} \sin \tilde{\vartheta}_p \cos(u_{\mathbf{k}} + \tilde{\varphi}_p). \end{aligned} \quad (\text{D.3})$$

Upon insertion into Eq. (D.1), we can readily read off that

$$\lambda_{\mathbf{k}} = \frac{A_0}{\sqrt{1 + \varepsilon^2}} \tilde{p} \sin \tilde{\vartheta}_p \delta(\mathbf{k} - \mathbf{k}_0) = \frac{A_0}{\sqrt{1 + \varepsilon^2}} \sqrt{p_x^2 + \varepsilon^2 p_y^2} \delta(\mathbf{k} - \mathbf{k}_0), \quad (\text{D.4})$$

$$\theta_{\mathbf{k}} = \tilde{\varphi}_p = \arctan(\varepsilon \tan \varphi_p), \quad (\text{D.5})$$

and with the definition $\eta_{\mathbf{k}} = \mathbf{p} \cdot \mathbf{k} - \omega_{\mathbf{k}}$, we find from Eq. (4.11e) that

$$\rho_{\mathbf{k}} = \frac{\lambda_{\mathbf{k}}}{\eta_{\mathbf{k}}} = \frac{A_0}{\sqrt{1 + \varepsilon^2}} \frac{\sqrt{p_x^2 + \varepsilon^2 p_y^2}}{\mathbf{p} \cdot \mathbf{k} - \omega_{\mathbf{k}}} \delta(\mathbf{k} - \mathbf{k}_0). \quad (\text{D.6})$$

2. $\Delta_{\mathbf{k}\mathbf{k}'}^+$ and $\theta_{\mathbf{k}\mathbf{k}'}^+$:

We insert the Fourier coefficients $\mathbf{a}(\mathbf{k})$ into Eq. (4.11b) and obtain

$$\begin{aligned} \Delta_{\mathbf{k}\mathbf{k}'}^+ \exp(i\theta_{\mathbf{k}\mathbf{k}'}^+) &= \frac{1}{4} \mathbf{a}(\mathbf{k}) \cdot \mathbf{a}(\mathbf{k}') \\ &= \frac{1}{4} \frac{A_0^2}{1 + \varepsilon^2} (\mathbf{e}_x + i\Lambda\varepsilon\mathbf{e}_y)^2 \delta(\mathbf{k} - \mathbf{k}_0) \delta(\mathbf{k}' - \mathbf{k}_0) \\ &= \frac{A_0^2}{4} \frac{1 - \varepsilon^2}{1 + \varepsilon^2} \delta(\mathbf{k} - \mathbf{k}_0) \delta(\mathbf{k}' - \mathbf{k}_0). \end{aligned} \quad (\text{D.7})$$

We can read off that

$$\Delta_{\mathbf{k}\mathbf{k}'}^+ = \frac{A_0^2}{4} \frac{1 - \varepsilon^2}{1 + \varepsilon^2} \delta(\mathbf{k} - \mathbf{k}_0) \delta(\mathbf{k}' - \mathbf{k}_0), \quad (\text{D.8})$$

$$\theta_{\mathbf{k}\mathbf{k}'}^+ = 0. \quad (\text{D.9})$$

3. $\Delta_{\mathbf{k}\mathbf{k}'}^-$ and $\theta_{\mathbf{k}\mathbf{k}'}^-$:

We insert the Fourier coefficients $\mathbf{a}(\mathbf{k})$ into Eq. (4.11c) and obtain

$$\begin{aligned} \Delta_{\mathbf{k}\mathbf{k}'}^- \exp(i\theta_{\mathbf{k}\mathbf{k}'}^-) &= \frac{1}{4} \mathbf{a}(\mathbf{k}) \cdot \mathbf{a}^*(\mathbf{k}') \\ &= \frac{1}{4} \frac{A_0^2}{1 + \varepsilon^2} (\mathbf{e}_x + i\Lambda\varepsilon\mathbf{e}_y) \cdot (\mathbf{e}_x - i\Lambda\varepsilon\mathbf{e}_y) \delta(\mathbf{k} - \mathbf{k}_0) \delta(\mathbf{k}' - \mathbf{k}_0) \\ &= \frac{A_0^2}{4} \delta(\mathbf{k} - \mathbf{k}_0) \delta(\mathbf{k}' - \mathbf{k}_0). \end{aligned} \quad (\text{D.10})$$

We can read off that

$$\Delta_{\mathbf{k}\mathbf{k}'}^- = \frac{A_0^2}{4} \delta(\mathbf{k} - \mathbf{k}_0) \delta(\mathbf{k}' - \mathbf{k}_0), \quad (\text{D.11})$$

$$\theta_{\mathbf{k}\mathbf{k}'}^- = 0. \quad (\text{D.12})$$

4. $\sigma_{\mathbf{k}\mathbf{k}'}$ and $\xi_{\mathbf{k}\mathbf{k}'}$:

We insert the vector potential into Eq. (4.11d) and obtain

$$\sigma_{\mathbf{k}\mathbf{k}'} \cos(u_{\mathbf{k}'} + \xi_{\mathbf{k}\mathbf{k}'}) = -\mathbf{k} \cdot \mathbf{A}(\mathbf{k}', t). \quad (\text{D.13})$$

By comparing this definition with Eq. (D.1), we see that we can obtain $\sigma_{\mathbf{k}\mathbf{k}'}$ and $\xi_{\mathbf{k}\mathbf{k}'}$ from $\lambda_{\mathbf{k}}$ and $\theta_{\mathbf{k}}$, respectively, by replacing $\mathbf{k} \rightarrow \mathbf{k}'$ and $\mathbf{p} \rightarrow -\mathbf{k}$ in Eqs. (D.4) and (D.5):

$$\sigma_{\mathbf{k}\mathbf{k}'} = -\frac{A_0}{\sqrt{1+\varepsilon^2}} \sqrt{k_x^2 + \varepsilon^2 k_y^2} \delta(\mathbf{k}' - \mathbf{k}_0), \quad (\text{D.14})$$

$$\xi_{\mathbf{k}\mathbf{k}'} = 0. \quad (\text{D.15})$$

5. $\alpha_{\mathbf{k}\mathbf{k}'}^{\pm}$:

From the definition $\eta_{\mathbf{k}} = \mathbf{p} \cdot \mathbf{k} - \omega_{\mathbf{k}}$ and the above results (D.9) and (D.12) for $\Delta_{\mathbf{k}\mathbf{k}'}^{\pm}$, we find that

$$\alpha_{\mathbf{k}\mathbf{k}'}^{\pm} = \frac{A_0^2}{4} \frac{1 \mp \varepsilon^2}{1 + \varepsilon^2} \frac{1}{\mathbf{p} \cdot (\mathbf{k} \pm \mathbf{k}') - (\omega_{\mathbf{k}} \pm \omega_{\mathbf{k}'})} \delta(\mathbf{k} - \mathbf{k}_0) \delta(\mathbf{k}' - \mathbf{k}_0). \quad (\text{D.16})$$

The above results are identical to Eqs. (5.5) and upon insertion into the modified Volkov phase (4.20b) directly lead to Eq. (5.6).

D.2 STANDING LIGHT WAVE

Here we turn to the more complex case of a standing light wave with the vector potential (6.5) and show that Eqs. (4.11) and (4.20b) lead to the modified Volkov phase (6.6b) with the coefficients (6.7). Note that the following derivation can be generalized to two modes with arbitrary wave vectors \mathbf{k}_1 and \mathbf{k}_2 and also to more than two modes.

We begin by evaluating Eqs. (4.11). We will use the short hand notation

$$\Sigma_{\delta} = \sum_{j=1}^2 \delta(\mathbf{k} - \mathbf{k}_j), \quad (\text{D.17a})$$

$$\Sigma'_{\delta} = \sum_{j=1}^2 \delta(\mathbf{k}' - \mathbf{k}_j) \quad (\text{D.17b})$$

for convenience and indicate all other dependencies on the variable \mathbf{k} via a subscript.

1. $\lambda_{\mathbf{k}}$, $\theta_{\mathbf{k}}$ and $\rho_{\mathbf{k}}$:

Let us split the Fourier coefficients (6.5b) into real and imaginary parts,

$$\mathbf{a}_{\mathbf{k}} = \mathbf{a}(\mathbf{k}) = (\mathbf{a}_{\mathbf{R},\mathbf{k}} + i\mathbf{a}_{\mathbf{I},\mathbf{k}}) \Sigma_{\delta}, \quad (\text{D.18a})$$

$$\mathbf{a}_{\mathbf{R},\mathbf{k}} = \mathbf{a}_{\mathbf{R}}(\mathbf{k}) = \frac{A_{0,\mathbf{k}}}{\sqrt{1 + \varepsilon_{\mathbf{k}}^2}} \mathbf{e}_{1,\mathbf{k}}, \quad (\text{D.18b})$$

$$\mathbf{a}_{\mathbf{I},\mathbf{k}} = \mathbf{a}_{\mathbf{I}}(\mathbf{k}) = \frac{A_{0,\mathbf{k}}}{\sqrt{1 + \varepsilon_{\mathbf{k}}^2}} \varepsilon_{\mathbf{k}} \mathbf{e}_{2,\mathbf{k}}. \quad (\text{D.18c})$$

With this form, we insert the momentum space vector potential $\mathbf{A}(\mathbf{k}, t)$ from Eq. (6.5) into Eq. (4.11a) and obtain

$$\begin{aligned} \lambda_{\mathbf{k}} \cos(u_{\mathbf{k}} + \theta_{\mathbf{k}}) &= \mathbf{p} \cdot \mathbf{A}(\mathbf{k}, t) \\ &= \text{Re} \left\{ \mathbf{p} \cdot (\mathbf{a}_{\mathbf{R},\mathbf{k}} + i\mathbf{a}_{\mathbf{I},\mathbf{k}}) e^{iu_{\mathbf{k}}} \right\} \Sigma_{\delta} \\ &= \text{Re} \left\{ \sqrt{(\mathbf{p} \cdot \mathbf{a}_{\mathbf{R},\mathbf{k}})^2 + (\mathbf{p} \cdot \mathbf{a}_{\mathbf{I},\mathbf{k}})^2} e^{i \arctan\left(\frac{\mathbf{p} \cdot \mathbf{a}_{\mathbf{I},\mathbf{k}}}{\mathbf{p} \cdot \mathbf{a}_{\mathbf{R},\mathbf{k}}}\right)} e^{iu_{\mathbf{k}}} \right\} \Sigma_{\delta} \\ &= \sqrt{(\mathbf{p} \cdot \mathbf{a}_{\mathbf{R},\mathbf{k}})^2 + (\mathbf{p} \cdot \mathbf{a}_{\mathbf{I},\mathbf{k}})^2} \cos\left(u_{\mathbf{k}} + \arctan\left(\frac{\mathbf{p} \cdot \mathbf{a}_{\mathbf{I},\mathbf{k}}}{\mathbf{p} \cdot \mathbf{a}_{\mathbf{R},\mathbf{k}}}\right)\right) \Sigma_{\delta}. \end{aligned} \quad (\text{D.19})$$

Here, we can read off

$$\lambda_{\mathbf{k}} = \sqrt{(\mathbf{p} \cdot \mathbf{a}_{\mathbf{R},\mathbf{k}})^2 + (\mathbf{p} \cdot \mathbf{a}_{\mathbf{I},\mathbf{k}})^2} \Sigma_{\delta} = \frac{A_{0,\mathbf{k}}}{\sqrt{1 + \varepsilon_{\mathbf{k}}^2}} \sqrt{(\mathbf{p} \cdot \mathbf{e}_{1,\mathbf{k}})^2 + \varepsilon_{\mathbf{k}}^2 (\mathbf{p} \cdot \mathbf{e}_{2,\mathbf{k}})^2} \Sigma_{\delta} \quad (\text{D.20})$$

and

$$\theta_{\mathbf{k}} = \arctan\left(\frac{\mathbf{p} \cdot \mathbf{a}_{\mathbf{I},\mathbf{k}}}{\mathbf{p} \cdot \mathbf{a}_{\mathbf{R},\mathbf{k}}}\right) = \arctan\left(\varepsilon_{\mathbf{k}} \frac{\mathbf{p} \cdot \mathbf{e}_{2,\mathbf{k}}}{\mathbf{p} \cdot \mathbf{e}_{1,\mathbf{k}}}\right). \quad (\text{D.21})$$

Furthermore, with the definition $\eta_{\mathbf{k}} = \mathbf{p} \cdot \mathbf{k} - \omega_{\mathbf{k}}$ and Eq. (4.11e), we find that

$$\rho_{\mathbf{k}} = \frac{\lambda_{\mathbf{k}}}{\eta_{\mathbf{k}}} = \frac{A_{0,\mathbf{k}}}{\sqrt{1 + \varepsilon_{\mathbf{k}}^2}} \frac{\sqrt{(\mathbf{p} \cdot \mathbf{e}_{1,\mathbf{k}})^2 + \varepsilon_{\mathbf{k}}^2 (\mathbf{p} \cdot \mathbf{e}_{2,\mathbf{k}})^2}}{\mathbf{p} \cdot \mathbf{k} - \omega_{\mathbf{k}}} \Sigma_{\delta}. \quad (\text{D.22})$$

2. $\Delta_{\mathbf{k}\mathbf{k}'}^+$ and $\theta_{\mathbf{k}\mathbf{k}'}^+$:

We insert the Fourier coefficients $\mathbf{a}(\mathbf{k})$ into Eq. (4.11b) and obtain

$$\begin{aligned}
\Delta_{\mathbf{k}\mathbf{k}'}^+, \exp(i\theta_{\mathbf{k}\mathbf{k}'}^+) &= \frac{1}{4} \mathbf{a}(\mathbf{k}) \cdot \mathbf{a}(\mathbf{k}') \\
&= \frac{1}{4} (\mathbf{a}_{\mathbf{R},\mathbf{k}} + i\mathbf{a}_{\mathbf{I},\mathbf{k}}) (\mathbf{a}_{\mathbf{R},\mathbf{k}'} + i\mathbf{a}_{\mathbf{I},\mathbf{k}'}) \Sigma_\delta \Sigma'_\delta \\
&= \frac{1}{4} \sqrt{(\mathbf{a}_{\mathbf{R},\mathbf{k}}\mathbf{a}_{\mathbf{R},\mathbf{k}'} - \mathbf{a}_{\mathbf{I},\mathbf{k}}\mathbf{a}_{\mathbf{I},\mathbf{k}'})^2 + (\mathbf{a}_{\mathbf{R},\mathbf{k}}\mathbf{a}_{\mathbf{I},\mathbf{k}'} + \mathbf{a}_{\mathbf{I},\mathbf{k}}\mathbf{a}_{\mathbf{R},\mathbf{k}'})^2} \\
&\quad \times e^{i \arctan\left(\frac{\mathbf{a}_{\mathbf{R},\mathbf{k}}\mathbf{a}_{\mathbf{I},\mathbf{k}'} + \mathbf{a}_{\mathbf{I},\mathbf{k}}\mathbf{a}_{\mathbf{R},\mathbf{k}'}}{\mathbf{a}_{\mathbf{R},\mathbf{k}}\mathbf{a}_{\mathbf{R},\mathbf{k}'} - \mathbf{a}_{\mathbf{I},\mathbf{k}}\mathbf{a}_{\mathbf{I},\mathbf{k}'}}\right)} \Sigma_\delta \Sigma'_\delta
\end{aligned} \tag{D.23}$$

and therefore

$$\begin{aligned}
\Delta_{\mathbf{k}\mathbf{k}'}^+ &= \frac{1}{4} \sqrt{(\mathbf{a}_{\mathbf{R},\mathbf{k}}\mathbf{a}_{\mathbf{R},\mathbf{k}'} - \mathbf{a}_{\mathbf{I},\mathbf{k}}\mathbf{a}_{\mathbf{I},\mathbf{k}'})^2 + (\mathbf{a}_{\mathbf{R},\mathbf{k}}\mathbf{a}_{\mathbf{I},\mathbf{k}'} + \mathbf{a}_{\mathbf{I},\mathbf{k}}\mathbf{a}_{\mathbf{R},\mathbf{k}'})^2} \Sigma_\delta \Sigma'_\delta \\
&= \frac{A_{0,\mathbf{k}} A_{0,\mathbf{k}'}}{4 \sqrt{(1 + \varepsilon_{\mathbf{k}}^2) (1 + \varepsilon_{\mathbf{k}'}^2)}} \Sigma_\delta \Sigma'_\delta \\
&\quad \times \sqrt{(\mathbf{e}_{1,\mathbf{k}} \cdot \mathbf{e}_{1,\mathbf{k}'} - \varepsilon_{\mathbf{k}} \varepsilon_{\mathbf{k}'} \mathbf{e}_{2,\mathbf{k}} \cdot \mathbf{e}_{2,\mathbf{k}'})^2 + (\varepsilon_{\mathbf{k}'} \mathbf{e}_{1,\mathbf{k}} \cdot \mathbf{e}_{2,\mathbf{k}'} + \varepsilon_{\mathbf{k}} \mathbf{e}_{1,\mathbf{k}'} \cdot \mathbf{e}_{2,\mathbf{k}})^2}
\end{aligned} \tag{D.24}$$

and

$$\theta_{\mathbf{k}\mathbf{k}'}^+ = \arctan\left(\frac{\mathbf{a}_{\mathbf{R},\mathbf{k}}\mathbf{a}_{\mathbf{I},\mathbf{k}'} + \mathbf{a}_{\mathbf{I},\mathbf{k}}\mathbf{a}_{\mathbf{R},\mathbf{k}'}}{\mathbf{a}_{\mathbf{R},\mathbf{k}}\mathbf{a}_{\mathbf{R},\mathbf{k}'} - \mathbf{a}_{\mathbf{I},\mathbf{k}}\mathbf{a}_{\mathbf{I},\mathbf{k}'}}\right) = \arctan\left(\frac{\varepsilon_{\mathbf{k}'} \mathbf{e}_{1,\mathbf{k}} \cdot \mathbf{e}_{2,\mathbf{k}'} + \varepsilon_{\mathbf{k}} \mathbf{e}_{1,\mathbf{k}'} \cdot \mathbf{e}_{2,\mathbf{k}}}{\mathbf{e}_{1,\mathbf{k}} \cdot \mathbf{e}_{1,\mathbf{k}'} - \varepsilon_{\mathbf{k}} \varepsilon_{\mathbf{k}'} \mathbf{e}_{2,\mathbf{k}} \cdot \mathbf{e}_{2,\mathbf{k}'}}\right). \tag{D.25}$$

3. $\Delta_{\mathbf{k}\mathbf{k}'}^-$ and $\theta_{\mathbf{k}\mathbf{k}'}^-$:

Very similarly to the previous steps, we insert the Fourier coefficients $\mathbf{a}(\mathbf{k})$ into Eq. (4.11c) and obtain

$$\begin{aligned}
\Delta_{\mathbf{k}\mathbf{k}'}^-, \exp(i\theta_{\mathbf{k}\mathbf{k}'}^-) &= \frac{1}{4} \mathbf{a}(\mathbf{k}) \cdot \mathbf{a}^*(\mathbf{k}') \\
&= \frac{1}{4} (\mathbf{a}_{\mathbf{R},\mathbf{k}} + i\mathbf{a}_{\mathbf{I},\mathbf{k}}) (\mathbf{a}_{\mathbf{R},\mathbf{k}'} - i\mathbf{a}_{\mathbf{I},\mathbf{k}'}) \Sigma_\delta \Sigma'_\delta \\
&= \frac{1}{4} \sqrt{(\mathbf{a}_{\mathbf{R},\mathbf{k}}\mathbf{a}_{\mathbf{R},\mathbf{k}'} + \mathbf{a}_{\mathbf{I},\mathbf{k}}\mathbf{a}_{\mathbf{I},\mathbf{k}'})^2 + (\mathbf{a}_{\mathbf{R},\mathbf{k}}\mathbf{a}_{\mathbf{I},\mathbf{k}'} - \mathbf{a}_{\mathbf{I},\mathbf{k}}\mathbf{a}_{\mathbf{R},\mathbf{k}'})^2} \\
&\quad \times e^{i \arctan\left(\frac{\mathbf{a}_{\mathbf{R},\mathbf{k}}\mathbf{a}_{\mathbf{I},\mathbf{k}'} - \mathbf{a}_{\mathbf{I},\mathbf{k}}\mathbf{a}_{\mathbf{R},\mathbf{k}'}}{\mathbf{a}_{\mathbf{R},\mathbf{k}}\mathbf{a}_{\mathbf{R},\mathbf{k}'} + \mathbf{a}_{\mathbf{I},\mathbf{k}}\mathbf{a}_{\mathbf{I},\mathbf{k}'}}\right)} \Sigma_\delta \Sigma'_\delta.
\end{aligned} \tag{D.26}$$

Accordingly,

$$\begin{aligned}\Delta_{\mathbf{k}\mathbf{k}'}^- &= \frac{1}{4} \sqrt{(\mathbf{a}_{\mathbf{R},\mathbf{k}}\mathbf{a}_{\mathbf{R},\mathbf{k}'} + \mathbf{a}_{\mathbf{I},\mathbf{k}}\mathbf{a}_{\mathbf{I},\mathbf{k}'})^2 + (\mathbf{a}_{\mathbf{R},\mathbf{k}}\mathbf{a}_{\mathbf{I},\mathbf{k}'} - \mathbf{a}_{\mathbf{I},\mathbf{k}}\mathbf{a}_{\mathbf{R},\mathbf{k}'})^2} \Sigma_\delta \Sigma'_\delta \\ &= \frac{A_{0,\mathbf{k}}A_{0,\mathbf{k}'}}{4\sqrt{(1+\varepsilon_{\mathbf{k}}^2)(1+\varepsilon_{\mathbf{k}'}^2)}} \Sigma_\delta \Sigma'_\delta \\ &\quad \times \sqrt{(\mathbf{e}_{1,\mathbf{k}} \cdot \mathbf{e}_{1,\mathbf{k}'} + \varepsilon_{\mathbf{k}}\varepsilon_{\mathbf{k}'}\mathbf{e}_{2,\mathbf{k}} \cdot \mathbf{e}_{2,\mathbf{k}'})^2 + (\varepsilon_{\mathbf{k}'}\mathbf{e}_{1,\mathbf{k}} \cdot \mathbf{e}_{2,\mathbf{k}'} - \varepsilon_{\mathbf{k}}\mathbf{e}_{1,\mathbf{k}'} \cdot \mathbf{e}_{2,\mathbf{k}})^2}\end{aligned}\quad (\text{D.27})$$

and

$$\theta_{\mathbf{k}\mathbf{k}'}^- = \arctan\left(\frac{\mathbf{a}_{\mathbf{R},\mathbf{k}}\mathbf{a}_{\mathbf{I},\mathbf{k}'} - \mathbf{a}_{\mathbf{I},\mathbf{k}}\mathbf{a}_{\mathbf{R},\mathbf{k}'}}{\mathbf{a}_{\mathbf{R},\mathbf{k}}\mathbf{a}_{\mathbf{R},\mathbf{k}'} + \mathbf{a}_{\mathbf{I},\mathbf{k}}\mathbf{a}_{\mathbf{I},\mathbf{k}'}}\right) = \arctan\left(\frac{\varepsilon_{\mathbf{k}'}\mathbf{e}_{1,\mathbf{k}} \cdot \mathbf{e}_{2,\mathbf{k}'} - \varepsilon_{\mathbf{k}}\mathbf{e}_{1,\mathbf{k}'} \cdot \mathbf{e}_{2,\mathbf{k}}}{\mathbf{e}_{1,\mathbf{k}} \cdot \mathbf{e}_{1,\mathbf{k}'} + \varepsilon_{\mathbf{k}}\varepsilon_{\mathbf{k}'}\mathbf{e}_{2,\mathbf{k}} \cdot \mathbf{e}_{2,\mathbf{k}'}}\right). \quad (\text{D.28})$$

4. $\sigma_{\mathbf{k}\mathbf{k}'}$ and $\xi_{\mathbf{k}\mathbf{k}'}$:

As in App. D.1, we can obtain $\sigma_{\mathbf{k}\mathbf{k}'}$ and $\xi_{\mathbf{k}\mathbf{k}'}$ from $\lambda_{\mathbf{k}}$ and $\theta_{\mathbf{k}}$ in Eqs. (D.20) and (D.21), respectively, by replacing $\mathbf{k} \rightarrow \mathbf{k}'$ and $\mathbf{p} \rightarrow -\mathbf{k}$:

$$\sigma_{\mathbf{k}\mathbf{k}'} = \frac{A_{0,\mathbf{k}'}}{\sqrt{1+\varepsilon_{\mathbf{k}'}^2}} \sqrt{(\mathbf{k} \cdot \mathbf{e}_{1,\mathbf{k}'})^2 + \varepsilon_{\mathbf{k}'}^2 (\mathbf{k} \cdot \mathbf{e}_{2,\mathbf{k}'})^2} \Sigma'_\delta, \quad (\text{D.29})$$

$$\xi_{\mathbf{k}\mathbf{k}'} = \arctan\left(\varepsilon_{\mathbf{k}'} \frac{\mathbf{k} \cdot \mathbf{e}_{2,\mathbf{k}'}}{\mathbf{k} \cdot \mathbf{e}_{1,\mathbf{k}'}}\right). \quad (\text{D.30})$$

5. $\alpha_{\mathbf{k}\mathbf{k}'}^\pm$:

With the definition $\eta_{\mathbf{k}} = \mathbf{p} \cdot \mathbf{k} - \omega_{\mathbf{k}}$ and the above results (D.24) and (D.27) for Δ^\pm , we find that

$$\begin{aligned}\alpha_{\mathbf{k}\mathbf{k}'}^\pm &= \frac{A_{0,\mathbf{k}}A_{0,\mathbf{k}'}}{4\sqrt{(1+\varepsilon_{\mathbf{k}}^2)(1+\varepsilon_{\mathbf{k}'}^2)}} \Sigma_\delta \Sigma'_\delta \\ &\quad \times \frac{\sqrt{(\mathbf{e}_{1,\mathbf{k}} \cdot \mathbf{e}'_{1,\mathbf{k}} \mp \varepsilon_{\mathbf{k}}\varepsilon_{\mathbf{k}'}\mathbf{e}_{2,\mathbf{k}} \cdot \mathbf{e}_{2,\mathbf{k}'})^2 + (\varepsilon_{\mathbf{k}'}\mathbf{e}_{1,\mathbf{k}} \cdot \mathbf{e}_{2,\mathbf{k}'} \pm \varepsilon_{\mathbf{k}}\mathbf{e}_{1,\mathbf{k}'} \cdot \mathbf{e}_{2,\mathbf{k}})^2}}{\mathbf{p} \cdot (\mathbf{k} \pm \mathbf{k}') - (\omega_{\mathbf{k}} \pm \omega_{\mathbf{k}'})}.\end{aligned}\quad (\text{D.31})$$

Modified Volkov phase:

With the above results for the functions $\rho_{\mathbf{k}}$, $\theta_{\mathbf{k}}$, $\alpha_{\mathbf{k}\mathbf{k}'}^\pm$, $\theta_{\mathbf{k}\mathbf{k}'}^\pm$, $\sigma_{\mathbf{k}\mathbf{k}'}$ and $\xi_{\mathbf{k}\mathbf{k}'}$, we are now in a position to evaluate the integrals in the modified Volkov phase $\Gamma(\mathbf{r}, t)$ defined in Eq. (4.20b). We first note that the $\mathcal{O}(\alpha\delta_2)$ term that consists of the triple integrals over \mathbf{k} , \mathbf{k}' and \mathbf{k}'' in Eq. (4.15) vanishes for a standing light wave. This can be seen

by evaluating the \mathbf{k} and \mathbf{k}' integrals using the delta functions in Eqs. (D.31) and (D.29). One then finds that the resulting terms are proportional to $\sigma_{\mathbf{k}_i \mathbf{k}_j}$ with $i = 1, 2$ and $j = 1, 2$, respectively, and the wave vectors $\mathbf{k}_1 = \mathbf{e}_z$ and $\mathbf{k}_2 = -\mathbf{e}_z$ of the two counter-propagating laser modes. Since $\mathbf{k}_i \cdot \mathbf{e}_{1, \mathbf{k}_j} = 0$ for all combinations of i and j , one finds from Eq. (D.29) that $\sigma_{\mathbf{k}_i \mathbf{k}_j} = 0$ and, therefore, that all these terms vanish. By the same argument, the integrals with a prefactor $\frac{1}{2}$ in the modified Volkov phase (4.20b) vanish.

The remaining integrals can easily be solved by making use of the delta functions: with Eqs. (D.21) and (D.22), the single integral over \mathbf{k} is

$$\begin{aligned}
 & \int d^3 \mathbf{k} \rho_{\mathbf{k}} \sin(u_{\mathbf{k}} + \theta_{\mathbf{k}}) \\
 &= \sum_{j=1}^2 \int d^3 \mathbf{k} \frac{A_{0, \mathbf{k}}}{\sqrt{1 + \varepsilon_{\mathbf{k}}^2}} \frac{\sqrt{(\mathbf{p} \cdot \mathbf{e}_{1, \mathbf{k}})^2 + \varepsilon_{\mathbf{k}}^2 (\mathbf{p} \cdot \mathbf{e}_{2, \mathbf{k}})^2}}{\mathbf{p} \cdot \mathbf{k} - \omega_{\mathbf{k}}} \\
 & \quad \times \sin\left(u_{\mathbf{k}} + \arctan\left(\varepsilon_{\mathbf{k}} \frac{\mathbf{p} \cdot \mathbf{e}_{2, \mathbf{k}}}{\mathbf{p} \cdot \mathbf{e}_{1, \mathbf{k}}}\right)\right) \delta(\mathbf{k} - \mathbf{k}_j) \\
 &= \sum_{j=1}^2 \rho_j \sin(u_j + \theta_j), \tag{D.32}
 \end{aligned}$$

where we defined $u_j = u_{\mathbf{k}_j}$ and

$$\rho_1 = \frac{A_0^{(1)}}{\omega_1 \sqrt{1 + \varepsilon^2}} \frac{\sqrt{p_x^2 + \varepsilon^2 p_y^2}}{p_z/c - 1}, \tag{D.33a}$$

$$\rho_2 = -\frac{A_0^{(2)}}{\omega_2 \sqrt{1 + \varepsilon^2}} \frac{\sqrt{p_x^2 + \varepsilon^2 p_y^2}}{p_z/c + 1}, \tag{D.33b}$$

$$\theta_1 = -\Lambda \theta_2 = \arctan\left(\varepsilon \frac{p_y}{p_x}\right), \tag{D.33c}$$

since $\mathbf{p} \cdot \mathbf{e}_{1, \mathbf{k}_1} = p_x$, $\mathbf{p} \cdot \mathbf{e}_{2, \mathbf{k}_1} = p_y$, $\mathbf{p} \cdot \mathbf{e}_{1, \mathbf{k}_2} = -p_x$ and $\mathbf{p} \cdot \mathbf{e}_{2, \mathbf{k}_2} = p_y$, as well as $\mathbf{p} \cdot \mathbf{k}_1 = \omega_1/c p_z$ and $\mathbf{p} \cdot \mathbf{k}_2 = -\omega_2/c p_z$ for the standing light wave. Also, we have used that $\varepsilon_{\mathbf{k}_2} = \Lambda \varepsilon_{\mathbf{k}_1} = \Lambda \varepsilon$.

In the same way, we find with Eqs. (D.25) and (D.31) that

$$\int d^3 \mathbf{k} \int d^3 \mathbf{k}' \alpha_{\mathbf{k} \mathbf{k}'}^+ \sin(u_{\mathbf{k}} + u_{\mathbf{k}'} + \theta_{\mathbf{k} \mathbf{k}'}^+) = 2\alpha_{12}^+ \sin(u_1 + u_2) + \sum_{j=1}^2 \alpha_j^+ \sin(2u_j), \tag{D.34}$$

with

$$\alpha_{12}^+ = \frac{A_0^{(1)} A_0^{(2)}}{4} \frac{1 + \Lambda \varepsilon^2}{1 + \varepsilon^2} \frac{1}{p_z/c(\omega_1 - \omega_2) - (\omega_1 + \omega_2)}, \quad (\text{D.35a})$$

$$\alpha_1^+ = \frac{(A_0^{(1)})^2}{8\omega_1} \frac{1 - \varepsilon^2}{1 + \varepsilon^2} \frac{1}{p_z/c - 1}, \quad (\text{D.35b})$$

$$\alpha_2^+ = -\frac{(A_0^{(2)})^2}{4\omega_2} \frac{1 - \varepsilon^2}{1 + \varepsilon^2} \frac{1}{p_z/c + 1}. \quad (\text{D.35c})$$

Finally, the remaining integral has the same form as the previous one,

$$\int d^3\mathbf{k} \int d^3\mathbf{k}' \alpha_{\mathbf{k}\mathbf{k}'}^- \sin(u_{\mathbf{k}} - u_{\mathbf{k}'} + \theta_{\mathbf{k}\mathbf{k}'}^-) = 2\alpha_{12}^- \sin(u_1 - u_2) + \sum_{j=1}^2 \alpha_j^- \sin(2u_j), \quad (\text{D.36})$$

where, analogous to the definitions above,

$$\alpha_{12}^- = \frac{A_0^{(1)} A_0^{(2)}}{4} \frac{1 - \Lambda \varepsilon^2}{1 + \varepsilon^2} \frac{1}{p_z/c(\omega_1 + \omega_2) - (\omega_1 - \omega_2)}, \quad (\text{D.37a})$$

$$\alpha_1^- = \frac{(A_0^{(1)})^2}{4\omega_1} \frac{1}{p_z/c - 1}, \quad (\text{D.37b})$$

$$\alpha_2^- = -\frac{(A_0^{(2)})^2}{4\omega_2} \frac{1}{p_z/c + 1}. \quad (\text{D.37c})$$

Note that, in the integral (D.36), one has to be careful when integrating the two terms proportional to $\delta(\mathbf{k} - \mathbf{k}_j)\delta(\mathbf{k}' - \mathbf{k}_j)$, since an apparent singularity arises in the integrand for $\mathbf{k} = \mathbf{k}' = \mathbf{k}_j$. However, since the sine in the numerator also goes to zero in this case, the integral behaves well and can be solved in the same way as the integral in Eq. (5.8) for the single-mode plane-wave laser beam.

If the results (D.32), (D.34) and (D.36) are combined in the general expression for modified Volkov phase (4.20b) and the terms are slightly rearranged, we arrive at the modified Volkov phase (6.6b) with the coefficients (6.7) given in Sec. 6.3.1 for the standing wave.

BIBLIOGRAPHY

- Abramowitz, M. and I. Stegun, eds. (1972). *Handbook of Mathematical Functions with Formulas, Graphs, and Mathematical Tables*. 10th ed. Washington D.C.: United States Department of Commerce, National Bureau of Standards.
- Agostini, P., F. Fabre, G. Mainfray, G. Petite, and N. K. Rahman (1979). "Free-Free Transitions Following Six-Photon Ionization of Xenon Atoms." In: *Phys. Rev. Lett.* 42 (17), pp. 1127–1130. DOI: 10.1103/PhysRevLett.42.1127.
- Allen, L., M. W. Beijersbergen, R. J. C. Spreeuw, and J. P. Woerdman (1992). "Orbital angular momentum of light and the transformation of Laguerre-Gaussian laser modes." In: *Phys. Rev. A* 45 (11), pp. 8185–8189. DOI: 10.1103/PhysRevA.45.8185.
- Amini, K. et al. (2019). "Symphony on strong field approximation." In: *Reports on Progress in Physics* 82.11, p. 116001. DOI: 10.1088/1361-6633/ab2bb1.
- Ammosov, M. V., N. B. Delone, and V. P. Krainov (1986). "Tunnel ionization of complex atoms and of atomic ions in an alternating electromagnetic field." In: *Sov. Phys.-JETP* 64 (6), p. 1191.
- Andrews, D. L. and M. Babiker, eds. (2013). *The Angular Momentum of Light*. Cambridge: Cambridge University Press. DOI: 10.1017/CB09780511795213.
- Arbó, D. G., J. E. Miraglia, M. S. Gravielle, K. Schiessl, E. Persson, and J. Burgdörfer (2008). "Coulomb-Volkov approximation for near-threshold ionization by short laser pulses." In: *Phys. Rev. A* 77 (1), p. 013401. DOI: 10.1103/PhysRevA.77.013401.
- Arlt, J. and K. Dholakia (2000). "Generation of high-order Bessel beams by use of an axicon." In: *Optics Communications* 177.1–6, pp. 297–301. DOI: 10.1016/S0030-4018(00)00572-1.
- Baghdasaryan, B., B. Böning, W. Paufler, and S. Fritzsche (2019). "Dichroism in two-color above-threshold ionization with twisted XUV beams and intense infrared laser fields." In: *Phys. Rev. A* 99 (2), p. 023403. DOI: 10.1103/PhysRevA.99.023403.
- Batelaan, H. (2007). "Colloquium: Illuminating the Kapitza-Dirac effect with electron matter optics." In: *Rev. Mod. Phys.* 79 (3), pp. 929–941. DOI: 10.1103/RevModPhys.79.929.
- Bauer, D., D. B. Milošević, and W. Becker (2005). "Strong-field approximation for intense-laser-atom processes: The choice of gauge." In: *Phys. Rev. A* 72 (2), p. 023415. DOI: 10.1103/PhysRevA.72.023415.
- Becker, W., F. Grasbon, R. Kopold, D. Milošević, G. Paulus, and H. Walther (2002). "Above-Threshold Ionization: From Classical Features to Quantum Effects." In:

- Advances In Atomic, Molecular, and Optical Physics*. Elsevier, pp. 35–98. DOI: 10.1016/S1049-250X(02)80006-4.
- Becker, W, S. P. Goreslavski, D. B. Milošević, and G. G. Paulus (2018). “The plateau in above-threshold ionization: the keystone of rescattering physics.” In: *Journal of Physics B: Atomic, Molecular and Optical Physics* 51.16, p. 162002. DOI: 10.1088/1361-6455/aad150.
- Beijersbergen, M., R. Coerwinkel, M. Kristensen, and J. Woerdman (1994). “Helical-wavefront laser beams produced with a spiral phaseplate.” In: *Optics Communications* 112.5, pp. 321–327. DOI: 10.1016/0030-4018(94)90638-6.
- Blaga, C. I., F. Catoire, P. Colosimo, G. G. Paulus, H. G. Muller, P. Agostini, and L. F. DiMauro (2009). “Strong-field photoionization revisited.” In: *Nature Physics* 5, pp. 335–338. DOI: 10.1038/nphys1228.
- Böning, B., W. Paufler, and S. Fritzsche (2017). “Attosecond streaking with twisted X waves and intense infrared pulses.” In: *Phys. Rev. A* 96 (4), p. 043423. DOI: 10.1103/PhysRevA.96.043423.
- Böning, B., W. Paufler, and S. Fritzsche (2018). “Above-threshold ionization by few-cycle Bessel pulses carrying orbital angular momentum.” In: *Phys. Rev. A* 98 (2), p. 023407. DOI: 10.1103/PhysRevA.98.023407.
- Boucher, P., J. D. Hoyo, C. Billet, O. Pinel, G. Labroille, and F. Courvoisier (2018). “Generation of high conical angle Bessel–Gauss beams with reflective axicons.” In: *Applied Optics* 57.23, p. 6725. DOI: 10.1364/ao.57.006725.
- Brennecke, S. and M. Lein (2018). “High-order above-threshold ionization beyond the electric dipole approximation.” In: *Journal of Physics B: Atomic, Molecular and Optical Physics* 51.9, p. 094005. DOI: 10.1088/1361-6455/aab91f.
- Bucksbaum, P. H., D. W. Schumacher, and M. Bashkansky (1988). “High-Intensity Kapitza-Dirac Effect.” In: *Phys. Rev. Lett.* 61 (10), pp. 1182–1185. DOI: 10.1103/PhysRevLett.61.1182.
- Calegari, F., G. Sansone, S. Stagira, C. Vozzi, and M. Nisoli (2016). “Advances in attosecond science.” In: *Journal of Physics B: Atomic, Molecular and Optical Physics* 49.6, p. 062001. DOI: 10.1088/0953-4075/49/6/062001.
- Chelkowski, S., A. D. Bandrauk, and P. B. Corkum (2015). “Photon-momentum transfer in multiphoton ionization and in time-resolved holography with photoelectrons.” In: *Phys. Rev. A* 92 (5), p. 051401. DOI: 10.1103/PhysRevA.92.051401.
- Colosimo, P. et al. (2008). “Scaling strong-field interactions towards the classical limit.” In: *Nature Physics* 4, pp. 386–389. DOI: 10.1038/nphys914.
- Corkum, P. B. (1993). “Plasma perspective on strong field multiphoton ionization.” In: *Phys. Rev. Lett.* 71 (13), pp. 1994–1997. DOI: 10.1103/PhysRevLett.71.1994.

- Daněk, J., M. Klaiber, K. Z. Hatsagortsyan, C. H. Keitel, B. Willenberg, J. Maurer, B. W. Mayer, C. R. Phillips, L. Gallmann, and U. Keller (2018a). “Interplay between Coulomb-focusing and non-dipole effects in strong-field ionization with elliptical polarization.” In: *Journal of Physics B: Atomic, Molecular and Optical Physics* 51.11, p. 114001. DOI: 10.1088/1361-6455/aaba42.
- Daněk, J., K. Z. Hatsagortsyan, and C. H. Keitel (2018b). “Analytical approach to Coulomb focusing in strong-field ionization. I. Nondipole effects.” In: *Physical Review A* 97.6. DOI: 10.1103/physreva.97.063409.
- Dellweg, M. M. and C. Müller (2017). “Controlling electron spin dynamics in bichromatic Kapitza-Dirac scattering by the laser field polarization.” In: *Phys. Rev. A* 95 (4), p. 042124. DOI: 10.1103/PhysRevA.95.042124.
- Dirac, P. M. (1928). “The quantum theory of the electron.” In: *Proceedings of the Royal Society of London. Series A, Containing Papers of a Mathematical and Physical Character* 117.778, pp. 610–624. DOI: 10.1098/rspa.1928.0023.
- Dorney, K. M. et al. (2018). “Controlling the polarization and vortex charge of attosecond high-harmonic beams via simultaneous spin-orbit momentum conservation.” In: *Nature Photonics* 13, pp. 123–130. DOI: 10.1038/s41566-018-0304-3.
- Dura, J., N. Camus, A. Thai, A. Britz, M. Hemmer, M. Baudisch, A. Senftleben, C. D. Schröter, J. Ullrich, R. Moshhammer, and J. Biegert (2013). “Ionization with low-frequency fields in the tunneling regime.” In: *Scientific Reports* 3, p. 2675. DOI: 10.1038/srep02675.
- Eichmann, U., T. Nubbemeyer, H. Rottke, and W. Sandner (2009). “Acceleration of neutral atoms in strong short-pulse laser fields.” In: *Nature* 461, pp. 1261–1264. DOI: 10.1038/nature08481.
- Einstein, A. (1905). “Über einen die Erzeugung und Verwandlung des Lichtes betreffenden heuristischen Gesichtspunkt.” In: *Annalen der Physik* 322.6, pp. 132–148. DOI: 10.1002/andp.19053220607.
- Erhard, R. and H. Bauke (2015). “Spin effects in Kapitza-Dirac scattering at light with elliptical polarization.” In: *Phys. Rev. A* 92 (4), p. 042123. DOI: 10.1103/PhysRevA.92.042123.
- Faisal, F. H. M. (1973). “Multiple absorption of laser photons by atoms.” In: *Journal of Physics B: Atomic and Molecular Physics* 6.4, pp. L89–L92. DOI: 10.1088/0022-3700/6/4/011.
- Fang, X., K. F. MacDonald, E. Plum, and N. I. Zheludev (2016). “Coherent control of light-matter interactions in polarization standing waves.” In: *Scientific Reports* 6, p. 31141. DOI: 10.1038/srep31141.

- Faure, J., C. Rechatin, A. Norlin, A. Lifschitz, Y. Glinec, and V. Malka (2006). "Controlled injection and acceleration of electrons in plasma wakefields by colliding laser pulses." In: *Nature* 444, pp. 737–739. DOI: 10.1038/nature05393.
- Freimund, D. L. and H. Batelaan (2002). "Bragg Scattering of Free Electrons Using the Kapitza-Dirac Effect." In: *Phys. Rev. Lett.* 89 (28), p. 283602. DOI: 10.1103/PhysRevLett.89.283602.
- Freimund, D. L., K. Aflatooni, and H. Batelaan (2001). "Observation of the Kapitza-Dirac effect." In: *Nature* 413, pp. 142–143. DOI: 10.1038/35093065.
- Gariepy, G., J. Leach, K. T. Kim, T. J. Hammond, E. Frumker, R. W. Boyd, and P. B. Corkum (2014). "Creating High-Harmonic Beams with Controlled Orbital Angular Momentum." In: *Phys. Rev. Lett.* 113 (15), p. 153901. DOI: 10.1103/PhysRevLett.113.153901.
- Gelfand, I. and S. V. Fomin (2000). *Calculus of Variations*. 1st ed. Mineola, New York: Dover Publications.
- Guo, D.-S. and G. W. F. Drake (1992). "Multiphoton ionization in circularly polarized standing waves." In: *Phys. Rev. A* 45 (9), pp. 6622–6635. DOI: 10.1103/PhysRevA.45.6622.
- Harrington, B. (2018). *Inkscape, Version 0.92.3*. inkscape.org.
- Hartung, A. et al. (2019). "Magnetic fields alter strong-field ionization." In: *Nature Physics* 15, pp. 1222–1226. DOI: 10.1038/s41567-019-0653-y.
- He, P.-L., D. Lao, and F. He (2017). "Strong Field Theories beyond Dipole Approximations in Nonrelativistic Regimes." In: *Phys. Rev. Lett.* 118 (16), p. 163203. DOI: 10.1103/PhysRevLett.118.163203.
- Heckenberg, N. R., R. McDuff, C. P. Smith, and A. G. White (1992). "Generation of optical phase singularities by computer-generated holograms." In: *Opt. Lett.* 17.3, pp. 221–223. DOI: 10.1364/OL.17.000221.
- Hernández-García, C., J. A. Pérez-Hernández, T. Popmintchev, M. M. Murnane, H. C. Kapteyn, A. Jaron-Becker, A. Becker, and L. Plaja (2013). "Zeptosecond High Harmonic keV X-Ray Waveforms Driven by Midinfrared Laser Pulses." In: *Phys. Rev. Lett.* 111 (3), p. 033002. DOI: 10.1103/PhysRevLett.111.033002.
- Hernández-García, C., J. Vieira, J. Mendonça, L. Rego, J. S. Román, L. Plaja, P. Ribic, D. Gauthier, and A. Picón (2017). "Generation and Applications of Extreme-Ultraviolet Vortices." In: *Photonics* 4.4, p. 28. DOI: 10.3390/photonics4020028.
- Jackson, J. D. (1999). *Classical Electrodynamics*. 3rd ed. Hoboken, New Jersey: John Wiley & Sons.
- Jameson, P. and A. Khvedelidze (2008). "Classical dynamics of a charged particle in a laser field beyond the dipole approximation." In: *Phys. Rev. A* 77 (5), p. 053403. DOI: 10.1103/PhysRevA.77.053403.

- Kapitza, P. L. and P. A. M. Dirac (1933). "The reflection of electrons from standing light waves." In: *Mathematical Proceedings of the Cambridge Philosophical Society* 29.2, pp. 297–300. DOI: 10.1017/s0305004100011105.
- Keil, T. and D. Bauer (2017). "Coulomb-corrected strong-field quantum trajectories beyond dipole approximation." In: *Journal of Physics B: Atomic, Molecular and Optical Physics* 50.19, p. 194002. DOI: 10.1088/1361-6455/aa8ab1.
- Keldysh, L. V. (1964). "Ionization in the Field of a Strong Electromagnetic Wave." In: *Sov. Phys.-JETP* 20 (5), p. 1307.
- Klaiber, M., K. Z. Hatsagortsyan, and C. H. Keitel (2005). "Above-threshold ionization beyond the dipole approximation." In: *Phys. Rev. A* 71 (3), p. 033408. DOI: 10.1103/PhysRevA.71.033408.
- Klaiber, M., E. Yakaboylu, and K. Z. Hatsagortsyan (2013a). "Above-threshold ionization with highly charged ions in superstrong laser fields. II. Relativistic Coulomb-corrected strong-field approximation." In: *Phys. Rev. A* 87 (2), p. 023418. DOI: 10.1103/PhysRevA.87.023418.
- Klaiber, M., E. Yakaboylu, H. Bauke, K. Z. Hatsagortsyan, and C. H. Keitel (2013b). "Under-the-Barrier Dynamics in Laser-Induced Relativistic Tunneling." In: *Phys. Rev. Lett.* 110 (15), p. 153004. DOI: 10.1103/PhysRevLett.110.153004.
- Kopold, R., W. Becker, and D. B. Milošević (2002). "Quantum orbits: a space-time picture of intense-laser-induced processes in atoms." In: *Journal of Modern Optics* 49.12, pp. 1987–1999. DOI: 10.1080/09500340210140731.
- Kotlyar, V. V. and A. A. Kovalev (2008). "Family of hypergeometric laser beams." In: *J. Opt. Soc. Am. A* 25.1, pp. 262–270. DOI: 10.1364/JOSAA.25.000262.
- Krajewska, K. and J. Z. Kaminski (2015). "Radiation pressure in strong-field-approximation theory: Retardation and recoil corrections." In: *Phys. Rev. A* 92 (4), p. 043419. DOI: 10.1103/PhysRevA.92.043419.
- Krause, J. L., K. J. Schafer, and K. C. Kulander (1992). "High-order harmonic generation from atoms and ions in the high intensity regime." In: *Phys. Rev. Lett.* 68 (24), pp. 3535–3538. DOI: 10.1103/PhysRevLett.68.3535.
- Kulander, K. C. (1987). "Multiphoton ionization of hydrogen: A time-dependent theory." In: *Phys. Rev. A* 35 (1), pp. 445–447. DOI: 10.1103/PhysRevA.35.445.
- Li, M., J.-W. Geng, H. Liu, Y. Deng, C. Wu, L.-Y. Peng, Q. Gong, and Y. Liu (2014). "Classical-Quantum Correspondence for Above-Threshold Ionization." In: *Phys. Rev. Lett.* 112 (11), p. 113002. DOI: 10.1103/PhysRevLett.112.113002.
- Li, X., J. Zhang, Z. Xu, P. Fu, D.-S. Guo, and R. R. Freeman (2004). "Theory of the Kapitza-Dirac Diffraction Effect." In: *Phys. Rev. Lett.* 92 (23), p. 233603. DOI: 10.1103/PhysRevLett.92.233603.

- Ludwig, A., J. Maurer, B. W. Mayer, C. R. Phillips, L. Gallmann, and U. Keller (2014). "Breakdown of the Dipole Approximation in Strong-Field Ionization." In: *Phys. Rev. Lett.* 113 (24), p. 243001. DOI: 10.1103/PhysRevLett.113.243001.
- Maiman, T. H. (1960). "Stimulated Optical Radiation in Ruby." In: *Nature* 187, pp. 493–494. DOI: 10.1038/187493a0.
- Martin, P. J., B. G. Oldaker, A. H. Miklich, and D. E. Pritchard (1988). "Bragg scattering of atoms from a standing light wave." In: *Phys. Rev. Lett.* 60 (6), pp. 515–518. DOI: 10.1103/PhysRevLett.60.515.
- Matula, O., A. G. Hayrapetyan, V. G. Serbo, A. Surzhykov, and S. Fritzsche (2013). "Atomic ionization of hydrogen-like ions by twisted photons: angular distribution of emitted electrons." In: *Journal of Physics B: Atomic, Molecular and Optical Physics* 46.20, p. 205002. DOI: 10.1088/0953-4075/46/20/205002.
- Maurer, J., B. Willenberg, J. Daněk, B. W. Mayer, C. R. Phillips, L. Gallmann, M. Klaiber, K. Z. Hatsagortsyan, C. H. Keitel, and U. Keller (2018). "Probing the ionization wave packet and recollision dynamics with an elliptically polarized strong laser field in the nondipole regime." In: *Phys. Rev. A* 97 (1), p. 013404. DOI: 10.1103/PhysRevA.97.013404.
- Maxwell, J. C. (1865). "A dynamical theory of the electromagnetic field." In: *Philosophical Transactions of the Royal Society of London* 155, pp. 459–512. DOI: 10.1098/rstl.1865.0008.
- McGloin, D. and K. Dholakia (2005). "Bessel beams: Diffraction in a new light." In: *Contemporary Physics* 46.1, pp. 15–28. DOI: 10.1080/0010751042000275259.
- McPherson, A., G. Gibson, H. Jara, U. Johann, T. S. Luk, I. A. McIntyre, K. Boyer, and C. K. Rhodes (1987). "Studies of multiphoton production of vacuum-ultraviolet radiation in the rare gases." In: *J. Opt. Soc. Am. B* 4.4, pp. 595–601. DOI: 10.1364/JOSAB.4.000595.
- Milošević, D. B., G. G. Paulus, D. Bauer, and W. Becker (2006). "Above-threshold ionization by few-cycle pulses." In: *Journal of Physics B: Atomic, Molecular and Optical Physics* 39.14, R203–R262. DOI: 10.1088/0953-4075/39/14/r01.
- Moulton, P. F. (1986). "Spectroscopic and laser characteristics of Ti:Al₂O₃." In: *J. Opt. Soc. Am. B* 3.1, pp. 125–133. DOI: 10.1364/JOSAB.3.000125.
- Müller, R. A., D. Seipt, R. Beerwerth, M. Ornigotti, A. Szameit, S. Fritzsche, and A. Surzhykov (2016). "Photoionization of neutral atoms by X waves carrying orbital angular momentum." In: *Phys. Rev. A* 94 (4), p. 041402. DOI: 10.1103/PhysRevA.94.041402.
- Nairz, O., B. Brezger, M. Arndt, and A. Zeilinger (2001). "Diffraction of Complex Molecules by Structures Made of Light." In: *Phys. Rev. Lett.* 87 (16), p. 160401. DOI: 10.1103/PhysRevLett.87.160401.

- Ornigotti, M., C. Conti, and A. Szameit (2015). "Effect of Orbital Angular Momentum on Nondiffracting Ultrashort Optical Pulses." In: *Phys. Rev. Lett.* 115 (10), p. 100401. DOI: 10.1103/PhysRevLett.115.100401.
- Ornigotti, M., C. Conti, and A. Szameit (2016). "Cylindrically polarized nondiffracting optical pulses." In: *Journal of Optics* 18.7, p. 075605. DOI: 10.1088/2040-8978/18/7/075605.
- Paufler, W., B. Böning, and S. Fritzsche (2018a). "Strong-field ionization with twisted laser pulses." In: *Phys. Rev. A* 97 (4), p. 043418. DOI: 10.1103/PhysRevA.97.043418.
- Paufler, W., B. Böning, and S. Fritzsche (2018b). "Tailored orbital angular momentum in high-order harmonic generation with bicircular Laguerre-Gaussian beams." In: *Phys. Rev. A* 98 (1), p. 011401. DOI: 10.1103/PhysRevA.98.011401.
- Paufler, W., B. Böning, and S. Fritzsche (2019). "Strong-Field Ionization with Few-Cycle Bessel Pulses: Interplay Between Orbital Angular Momentum and Carrier Envelope Phase." In: *Quantum Collisions and Confinement of Atomic and Molecular Species, and Photons*. Ed. by P. C. Deshmukh, E. Krishnakumar, S. Fritzsche, M. Krishnamurthy, and S. Majumder. Singapore: Springer Singapore, pp. 274–284.
- Paulus, G. G., W. Nicklich, H. Xu, P. Lambropoulos, and H. Walther (1994). "Plateau in above threshold ionization spectra." In: *Phys. Rev. Lett.* 72 (18), pp. 2851–2854. DOI: 10.1103/PhysRevLett.72.2851.
- Paulus, G. G., F. Grasbon, H. Walther, P. Villoresi, M. Nisoli, S. Stagira, E. Priori, and S. D. Silvestri (2001). "Absolute-phase phenomena in photoionization with few-cycle laser pulses." In: *Nature* 414, pp. 182–184. DOI: 10.1038/35102520.
- Peshkov, A. A., D. Seipt, A. Surzhykov, and S. Fritzsche (2017). "Photoexcitation of atoms by Laguerre-Gaussian beams." In: *Phys. Rev. A* 96 (2), p. 023407. DOI: 10.1103/PhysRevA.96.023407.
- Pisanty, E., D. D. Hickstein, B. R. Galloway, C. G. Durfee, H. C. Kapteyn, M. M. Murnane, and M. Ivanov (2018). "High harmonic interferometry of the Lorentz force in strong mid-infrared laser fields." In: *New Journal of Physics* 20.5, p. 053036. DOI: 10.1088/1367-2630/aabb4d.
- Planck, M. (1901). "Ueber das Gesetz der Energieverteilung im Normalspectrum." In: *Annalen der Physik* 309.3, pp. 553–563. DOI: 10.1002/andp.19013090310.
- Popmintchev, T. et al. (2012). "Bright Coherent Ultrahigh Harmonics in the keV X-ray Regime from Mid-Infrared Femtosecond Lasers." In: *Science* 336.6086, pp. 1287–1291. DOI: 10.1126/science.1218497.
- Quinteiro, G. F., D. E. Reiter, and T. Kuhn (2017a). "Formulation of the twisted-light-matter interaction at the phase singularity: Beams with strong magnetic fields." In: *Phys. Rev. A* 95 (1), p. 012106. DOI: 10.1103/PhysRevA.95.012106.

- Quinteiro, G. F., F. Schmidt-Kaler, and C. T. Schmiegelow (2017b). "Twisted-Light-Ion Interaction: The Role of Longitudinal Fields." In: *Phys. Rev. Lett.* 119 (25), p. 253203. DOI: 10.1103/PhysRevLett.119.253203.
- Reiss, H. R. (2008). "Limits on Tunneling Theories of Strong-Field Ionization." In: *Phys. Rev. Lett.* 101 (4), p. 043002. DOI: 10.1103/PhysRevLett.101.043002.
- Reiss, H. R. (2014). "The tunnelling model of laser-induced ionization and its failure at low frequencies." In: *Journal of Physics B: Atomic, Molecular and Optical Physics* 47.20, p. 204006. DOI: 10.1088/0953-4075/47/20/204006.
- Reiss, H. R. (1980). "Effect of an intense electromagnetic field on a weakly bound system." In: *Phys. Rev. A* 22 (5), pp. 1786–1813. DOI: 10.1103/PhysRevA.22.1786.
- Rosenberg, L. (1994). "Effect of virtual Compton scattering on electron propagation in a laser field." In: *Phys. Rev. A* 49 (2), pp. 1122–1130. DOI: 10.1103/PhysRevA.49.1122.
- Rosenberg, L. and F. Zhou (1993). "Generalized Volkov wave functions: Application to laser-assisted scattering." In: *Phys. Rev. A* 47 (3), pp. 2146–2155. DOI: 10.1103/PhysRevA.47.2146.
- Salamin, Y. I., G. R. Mocken, and C. H. Keitel (2003). "Relativistic electron dynamics in intense crossed laser beams: Acceleration and Compton harmonics." In: *Phys. Rev. E* 67 (1), p. 016501. DOI: 10.1103/PhysRevE.67.016501.
- Saleh, B. E. A. and M. C. Teich (1991). *Fundamentals of Photonics*. 1st ed. New York: John Wiley & Sons.
- Sarachik, E. S. and G. T. Schappert (1970). "Classical Theory of the Scattering of Intense Laser Radiation by Free Electrons." In: *Phys. Rev. D* 1 (10), pp. 2738–2753. DOI: 10.1103/PhysRevD.1.2738.
- Schafer, K. J., B. Yang, L. F. DiMauro, and K. C. Kulander (1993). "Above threshold ionization beyond the high harmonic cutoff." In: *Phys. Rev. Lett.* 70 (11), pp. 1599–1602. DOI: 10.1103/PhysRevLett.70.1599.
- Schmiegelow, C. T., J. Schulz, H. Kaufmann, T. Ruster, U. G. Poschinger, and F. Schmidt-Kaler (2016). "Transfer of optical orbital angular momentum to a bound electron." In: *Nature Communications* 7, p. 12998. DOI: 10.1038/ncomms12998.
- Scholz-Marggraf, H. M., S. Fritzsche, V. G. Serbo, A. Afanasev, and A. Surzhykov (2014). "Absorption of twisted light by hydrogenlike atoms." In: *Phys. Rev. A* 90 (1), p. 013425. DOI: 10.1103/PhysRevA.90.013425.
- Schrödinger, E. (1926). "An Undulatory Theory of the Mechanics of Atoms and Molecules." In: *Phys. Rev.* 28 (6), pp. 1049–1070. DOI: 10.1103/PhysRev.28.1049.
- Schultze, M. et al. (2010). "Delay in Photoemission." In: *Science* 328.5986, pp. 1658–1662. DOI: 10.1126/science.1189401.

- Seipt, D., R. A. Müller, A. Surzhykov, and S. Fritzsche (2016). “Two-color above-threshold ionization of atoms and ions in XUV Bessel beams and intense laser light.” In: *Phys. Rev. A* 94 (5), p. 053420. DOI: 10.1103/PhysRevA.94.053420.
- Smeenck, C. T. L., L. Arissian, B. Zhou, A. Mysyrowicz, D. M. Villeneuve, A. Staudte, and P. B. Corkum (2011). “Partitioning of the Linear Photon Momentum in Multiphoton Ionization.” In: *Phys. Rev. Lett.* 106 (19), p. 193002. DOI: 10.1103/PhysRevLett.106.193002.
- Smirnova, O., D. L. Freimund, H. Batelaan, and M. Ivanov (2004). “Kapitza-Dirac Diffraction without Standing Waves: Diffraction without a Grating?” In: *Phys. Rev. Lett.* 92 (22), p. 223601. DOI: 10.1103/PhysRevLett.92.223601.
- Smorenburg, P. W., J. H. M. Kanters, A. Lassise, G. J. H. Brussaard, L. P. J. Kamp, and O. J. Luiten (2011). “Polarization-dependent ponderomotive gradient force in a standing wave.” In: *Phys. Rev. A* 83 (6), p. 063810. DOI: 10.1103/PhysRevA.83.063810.
- Surzhykov, A., D. Seipt, and S. Fritzsche (2016). “Probing the energy flow in Bessel light beams using atomic photoionization.” In: *Phys. Rev. A* 94 (3), p. 033420. DOI: 10.1103/PhysRevA.94.033420.
- Titi, A. S. and G. W. F. Drake (2012). “Quantum theory of longitudinal momentum transfer in above-threshold ionization.” In: *Phys. Rev. A* 85 (4), p. 041404. DOI: 10.1103/PhysRevA.85.041404.
- Walker, B., B. Sheehy, L. F. DiMauro, P. Agostini, K. J. Schafer, and K. C. Kulander (1994). “Precision Measurement of Strong Field Double Ionization of Helium.” In: *Phys. Rev. Lett.* 73 (9), pp. 1227–1230. DOI: 10.1103/PhysRevLett.73.1227.
- Whittaker, E. T. (1910). *A history of the theories of aether and electricity from the age of Descartes to the close of the nineteenth century*. London, New York: Longmans, Green and Co. DOI: 10.5962/bhl.title.19630.
- Willenberg, B., J. Maurer, U. Keller, J. Daněk, M. Klaiber, N. Teeny, K. Z. Hatsagortsyan, and C. H. Keitel (2019). “Holographic interferences in strong-field ionization beyond the dipole approximation: The influence of the peak and focal-volume-averaged laser intensities.” In: *Phys. Rev. A* 100 (3), p. 033417. DOI: 10.1103/PhysRevA.100.033417.
- Wolfram Research, Inc. (2016). *Mathematica, Version 11.0*. wolfram.com/mathematica, Champaign, IL.
- Wolkow, D. M. (1935). “Über eine Klasse von Lösungen der Diracschen Gleichung.” In: *Zeitschrift für Physik* 94.3-4, pp. 250–260. DOI: 10.1007/bf01331022.
- Wollenhaupt, M., T. Bayer, and T. Baumert (2016). “Control of Ultrafast Electron Dynamics with Shaped Femtosecond Laser Pulses: From Atoms to Solids.” In: *Ultrafast Dynamics Driven by Intense Light Pulses: From Atoms to Solids, from Lasers*

- to Intense X-rays*. Ed. by M. Kitzler and S. Gräfe. Cham: Springer International Publishing, pp. 63–122. DOI: 10.1007/978-3-319-20173-3_4.
- Wolter, B., M. G. Pullen, M. Baudisch, M. Scalfani, M. Hemmer, A. Senftleben, C. D. Schröter, J. Ullrich, R. Moshhammer, and J. Biegert (2015). “Strong-Field Physics with Mid-IR Fields.” In: *Phys. Rev. X* 5 (2), p. 021034. DOI: 10.1103/PhysRevX.5.021034.
- Yakaboylu, E., M. Klaiber, H. Bauke, K. Z. Hatsagortsyan, and C. H. Keitel (2013). “Relativistic features and time delay of laser-induced tunnel ionization.” In: *Phys. Rev. A* 88 (6), p. 063421. DOI: 10.1103/PhysRevA.88.063421.
- Yu, C., J. Zhang, Z. Sun, J. Gao, and D.-S. Guo (2015). “Conditions for ponderomotive resonances in the Kapitza–Dirac effect.” In: *Frontiers of Physics* 10.5, p. 104208. DOI: 10.1007/s11467-015-0499-4.

EHRENWÖRTLICHE ERKLÄRUNG

Ich erkläre hiermit ehrenwörtlich, dass ich die vorliegende Arbeit selbstständig, ohne unzuässige Hilfe dritter und ohne Benutzung anderer als der angegebenen Hilfsmittel und Literatur angefertigt habe. Die aus anderen Quellen direkt oder indirekt übernommenen Daten und Konzepte sind unter Angabe der Quelle gekennzeichnet. Bei der Anfertigung dieser Arbeit haben mir meine Betreuer und die Koautoren oben genannter Publikationen geholfen.

Weitere Personen waren an der inhaltlich-materiellen Erstellung der vorliegenden Arbeit nicht beteiligt. Insbesondere habe ich hierfür nicht die entgeltliche Hilfe von Vermittlungs- bzw. Beratungsdiensten (Promotionsberater oder andere Personen) in Anspruch genommen.

Niemand hat von mir unmittelbar oder mittelbar geldwerte Leistungen für Arbeiten erhalten, die im Zusammenhang mit dem Inhalt der vorgelegten Dissertation stehen. Die Arbeit wurde bisher weder im In- noch im Ausland in gleicher oder ähnlicher Form einer anderen Prüfungsbehörde vorgelegt. Die geltende Promotionsordnung der Physikalisch-Astronomischen Fakultät ist mir bekannt.

Ich versichere ehrenwörtlich, dass ich nach bestem Wissen die reine Wahrheit gesagt und nichts verschwiegen habe.

Jena,

Birger Nils Böning